DIPLOMARBEIT

Simulation of the dynamic range of retinal ganglion cells during microelectrode stimulation

zur Erlangung des akademischen Grades

Diplom-Ingenieurin

im Rahmen des Studiums

Biomedical Engineering

Eingerichtet von

Fatima Dizdar

Matrikelnummer: 01428838

ausgeführt am Institut für Analysis und Scientific Computing
der Fakultät für Mathematik und Geoinformatik der Technischen Universität Wien

Betreuung:

Ao.Univ.Prof.Dipl.-Ing. Dr.sc.med. Dr.techn. Dr.rer.nat. Frank Rattay

Dipl.-Ing. Dr.techn. Paul Werginz

Wien, Dezember 2022

Abstract

Electrical stimulation of retinal ganglion cells (RGC) plays an important role in the creation of retinal prostheses which aim to restore vision in people suffering from degenerative retinal diseases by stimulating the remaining healthy retinal neurons. In order to better investigate the influence of electrical stimulation on RGCs, in addition to experimental studies, many computational RGC models have been developed. Given that most of these models are based on the deterministic well-known Hodgkin and Huxley model, they also lack a stochastic component that would mimic the natural channel noise present in cells. When we calculate the stimulus threshold with a deterministic model, we lose information about the spiking probability, which increases from 0 to 1 as a function of stimulus intensity following thereby the shape of a sigmoidal curve. In this thesis we study the stochastic behavior of RGCs by calculating dynamic range (DR), defined as the stimulus intensity range in which spiking probability increases from 0.1 to 0.9. The main aim of the thesis is to analyze DR in dependency on the stimulated part of the RGC, since different cell sections show different geometrical and biophysical properties. For that, a multi-compartment RGC model based on Fohlmeister and Miller model from 1997 was implemented in NEURON and Python. A stochastic component was added to the model by injecting the maximum sodium conductance dependent noise current into each cell compartment. We observed that, regardless of the type of stimulation (intracellular or extracellular), DR values given as percentage seem to show a somewhat inverse relationship to threshold values. With intracellular stimulation, a steeper sigmoidal curve of spiking probability was observed for axonal than for somatic compartments, as reported by previous experimental studies. With extracellular stimulation this behavior was observed only after increasing channel noise at soma. While estimating DR with an upper threshold, similar DR values given in μA (not normalized to threshold) as with a lower threshold were observed, which could indicate from previous studies reported characteristic U-shape of spiking probability as a function of stimulus intensity.

Kurzfassung

Die elektrische Stimulation der Ganglienzellen (RGC) spielt eine wichtige Rolle bei der Herstellung von Netzhautprothesen. Um den Einfluss der elektrischen Stimulation der RGC besser zu verstehen, wurden neben experimentellen Studien viele rechnergestützte RGC-Modelle entwickelt. Da die meisten dieser Modelle auf dem bekannten deterministischen Modell von Hodgkin und Huxley basiert sind, fehlt ihnen auch eine stochastische Komponente, die das in Zellen vorhandene natürliche Kanalrauschen imitieren würde. Wenn wir den Schwellenwert mit einem deterministischen Modell berechnen, verlieren wir Information über die Feuerungswahrscheinlichkeit, die als Funktion der Stimulsintensität von 0 auf 1 ansteigt und dabei der Form einer sigmoidalen Kurve folgt. In dieser Diplomarbeit untersuchen wir das stochastische Verhalten von RGC durch Berechnung des sogenannten *dynamic range* (DR), der als der Stimulusintensitätsbereich definiert ist, in dem die Feuerungswahrscheinlichkeit von 0.1 auf 0.9 ansteigt. Das Hauptziel ist es, DR in der Abhängigkeit vom stimulierten Teil der Zelle zu analysieren, da verschiedene Zellteilen unterschiedliche geometrische und biophysikalische Eigenschaften aufweisen. Dazu wurde ein Multi-Compartment-RGC-Modell basierend auf dem Fohlmeister und Miller Modell von 1997 in NEURON und Python implementiert. Dem Modell wurde eine stochastische Komponente hinzugefügt, indem der von der maximalen Natriumleitfähigkeit abhängige Rauschstrom in jedes Zellsegment injiziert wurde. Zusammenfassend sieht es so aus, dass unabhängig von der Art der Stimulation (intrazellulär oder extrazellulär), die in Prozent angegebene DR-Werte eine etwas inverse Beziehung zu den Schwellenwerten aufweisen. Bei intrazellulärer Stimulation wurde eine steilere sigmoidale Kurve der Feuerungswahrscheinlichkeit für axonale als für somatische Stimulationen beobachtet, wie es auch von früheren experimentellen Studien berichtet wurde. Bei extrazellulärer Stimulation wurde dieses Verhalten nur nach der Erhöhung des Kanalrauschens bei Soma beobachtet. Bei der Schätzung der DR-Werte an der oberen Schwelle wurden ähnliche in μA angegebenen DR-Werte wie an der unteren Schwelle beobachtet, was auf die charakteristische U-Form der Feuerungswahrscheinlichkeit als Funktion der Stimulsintensität hinweisen könnte, die schon in früheren Studien berichtet wurde.

Acknowledgements

First and foremost, I want to sincerely thank Prof. Frank Rattay, who supervised this thesis. His balance between giving me enough space to follow my intuition during the research and at the same time providing support and guidance in every part of the process is marvelous. Thank you for creating such a pleasant working atmosphere.

Secondly, I want to thank Dr. Paul Werginz for his selfless support and discussions during this research. His suggestions were especially valuable for the optimization of the performed simulations as well as for a deeper understanding of the processes behind them. Big thanks go also to Dr. Andreas Fellner, who was advising me at the beginning of my introduction to nerve cell modeling in NEURON.

Special thanks to Ms. Angela Pecinovsky and Ms. Sonja Weiss from the Dean's Office of Faculty for Mathematics and Geoinformation for all their generous support during submission of the thesis.

Words cannot express my gratefulness to my Mom, Dad and Brother who, despite our distance, made sure that I feel their support and love every day. I am also deeply grateful to my closest friends in and outside of Vienna for all their inspiration and belief in me.

In the end, I want to express my deepest gratitude to my boyfriend Dusan. Having him as a companion since the beginning of our studies and especially during this research is simply invaluable. Thank you for all the interesting discussions on topics related to this thesis, and most importantly, thank you for your immense love and constant encouragement through all ups and downs over the past years.

Content

1 Introduction

In this section, the basics of the structure and functioning of nerve cells will be presented, which are necessary for a correct understanding of further work. Different characteristics of nerve cells that enable intercellular communication are shown and the basics of signal transmission through one nerve cell and from one to another nerve cell are described.

1.1 Nerve cells compared to other cells

Nerve cells (neurons) are cells that are specialized for intercellular communication and as such form the basic units of nervous tissues. If we look at the basic organization of a nerve cell, apart from some minor deviations, there is no essential difference compared to other cells. For example, nerve cells contain the same types of organelles as other cells, but there is usually a difference in their distribution compared to other cells. Contrary to that, if we observe the morphology of nerve cells, we come to the first major differences between nerve cells and other cells. Their morphology, characterized by the branching of their specific parts, is something that significantly contributes to intercellular communication. Apart from morphology, the cell membrane (specialized for conducting signals through a neuron) and synapses (specialized for transmitting signals between two neurons) are the key mechanisms of this type of communication. (Purves, et al., 2004)

Figure 1 shows a typical vertebrate neuron. Almost every neuron consists of three main parts. The first part is the soma, the so-called cell body, in which the nucleus is located. Numerous extensions emerge from the soma and form the other two main parts of the neuron: the axon and the dendrite. The axon is usually the longest branch that emerges from the soma and carries the signal away from the cell body to the synaptic connections with other neurons. As we can see in Figure 1, the axon branches at its very end so that it can transmit the signal to as many cells as possible in parallel.

Dendrites, unlike axons, have many short branches that spring from different sides of the soma and are thus able to receive signals from other neurons via synaptic connections. (Alberts, et al., 2002)

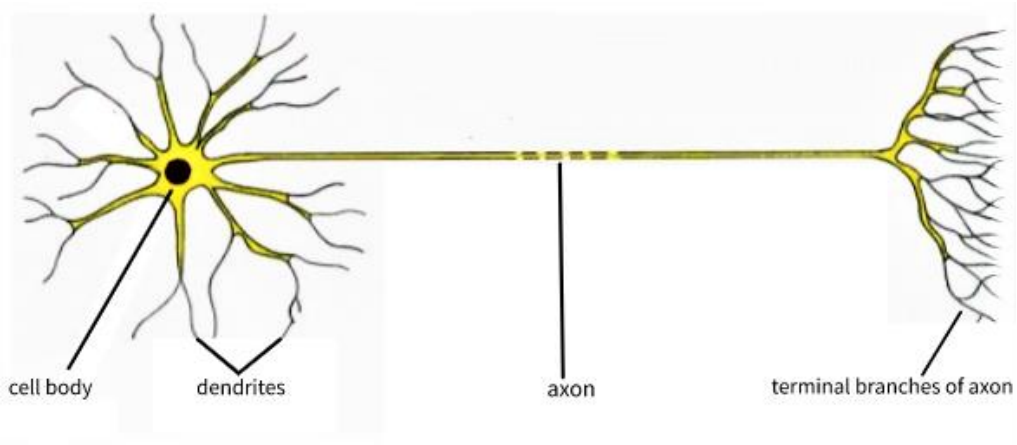

Figure 1: Vertebrate neuron. In the figure we can observe all three main part of typical nerve cell: soma as a cell body, dendrites as branches that receive signals from other cells and axon with its terminal end as branches that conduct signal away from the body cell and transmit it to synaptic connections with other nerve cells. Figure and parts of caption adapted from Alberts, et al. (2002).

There are numerous variations in the morphology of nerve cells depending on the function of individual neurons (Figure 2). We can see these differences, for example, in the length of the axon. Thus, the neurons that transmit the signal to the peripheral parts of the body will have significantly longer axons than the neurons that connect two parts of the brain, the so-called local circuit neurons. A similar thing is observed with dendrites, the more input a certain neuron should receive, the more complex its dendritic tree will be. (Purves, et al., 2004)

In addition to morphology, we mentioned synapses as one very important aspect of intercellular communication. Synapses are connections between two nerve cells that enable signal transmission between them. We distinguish two types of synapses: electrical and chemical. Electrical synapses are characterized with channels, so-called gap junctions, that connect cytoplasm of presynaptic (neuron from which electrical signal is coming) and postsynaptic neuron (neuron which receives electrical signal). Those gap junctions allow current to passively pass from presynaptic to postsynaptic neurons and thus transmit signals. Chemical synapses don´t need physical connection of cells in order to transmit a signal from one cell into the other. They work in a

following way: in the moment of signal transmission presynaptic cell releases neurotransmitter (chemical signals that carry information about electrical signal that needs to be transmitted) from its synaptic vesicles and those neurotransmitters then transfer "the signal" to the receptors at the postsynaptic cell. According to the information received from neurotransmitters, those receptors produce secondary current flow, and the signal is transmitted. (Purves, et al., 2004)

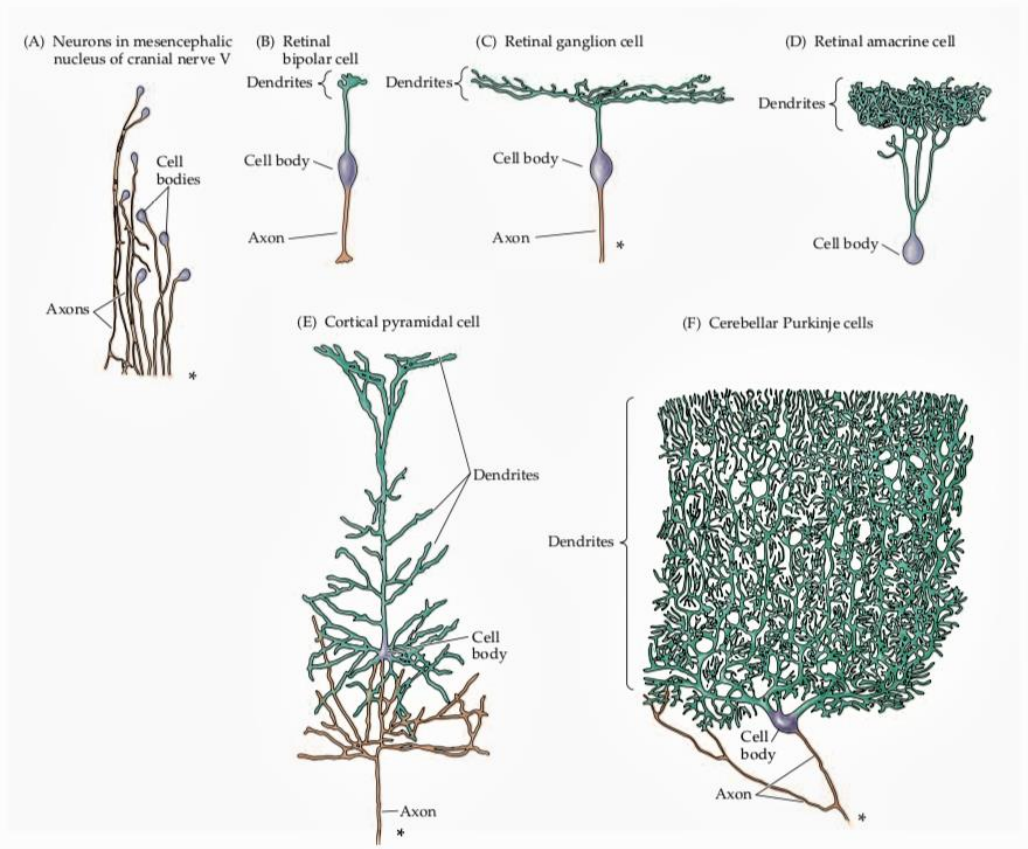

Figure 2: Variations in morphology of nerve cells as a consequence of their different function. Note that not all cells or parts of cells are drawn at the same scale. Figure and parts of caption from Purves, et al. (2004).

1.2 Ion channels and action potential

As we have already mentioned, nerve cells are specialized for intercellular communication i.e., for transmitting signals through a neuron and with the help of synaptic connections from one neuron to another. Signals are transmitted in the form of electrical signals and the main role here is played by the cell membrane and its ion channels.

Cell membranes are made of a phospholipid bilayer that creates a barrier between the inner and outer parts of the cell, which prevents the free transport of molecules into and out of the cell. While small uncharged molecules can diffuse through the phospholipid bilayer, large polar molecules and ions cannot (Figure 3). (Cooper, 2000)

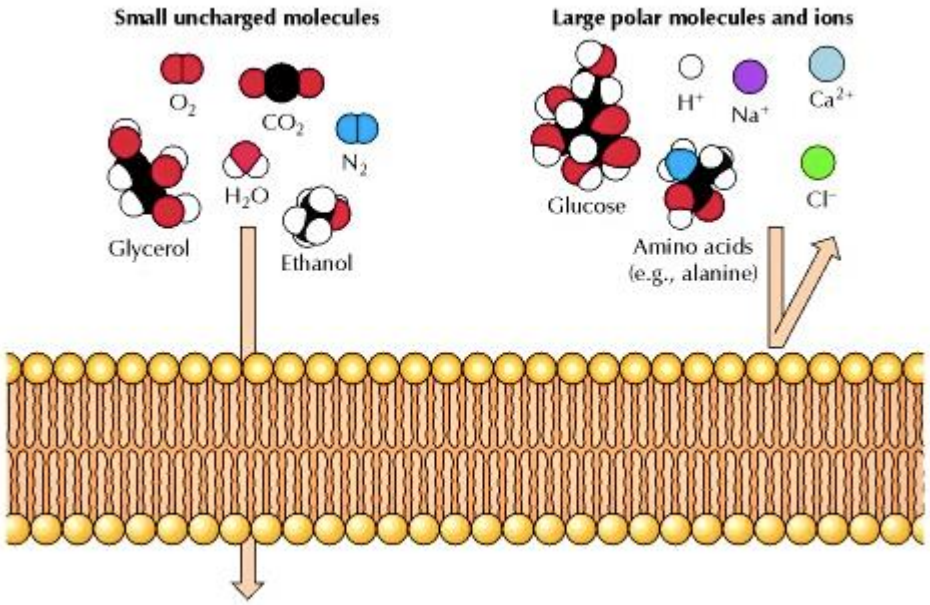

Figure 3: Permeability of the cell membrane due to its phospholipid bilayer. The figure shows that some small uncharged molecules can diffuse through the cell membrane without any other support mechanism. In contrast to that, large polar molecules will need different kinds of supporting mechanisms (channel or carrier proteins for example) in order to pass the cell membrane. Figure and parts of caption from Cooper (2000).

In order to allow transport of different ions into and out of the cell, the cell membrane contains different types of ion channels. The first important characteristic of ion channels is ion selectivity, which means that a certain ion channel lets only one or more specific ions through. Another characteristic of ion channels is that they are not constantly open for ion transport, but open exclusively under specific conditions that depend on the type of ion channel. (Alberts, et al., 2002)

For us, the voltage-gated type of ion channels is particularly interesting because they actively participate in signal transmission through neurons by creating action potentials, which will be discussed soon.

The cell membrane always has a certain membrane potential, which represents the difference between the electrical potentials inside and outside the cell. This difference

in electric potentials, also called transmembrane voltage, is caused by the different concentration of ions on both sides of the cell membrane (for example sodium Na^+ that is dominant in extracellular space and potassium K^+ that is dominant inside the cell). When the neuron is unexcited (does not transmit a signal), it is in a state of rest and has a so-called resting membrane potential that is negative and has a value about $-70\ mV$ (depending on the type of neuron it can be lower or higher). But when the neuron is excited (using, for example, electrical current), there is also a change in the membrane potential. This change is called the action potential (AP) and is characterized by a rapid increase in the membrane potential that reaches positive values and then drops and returns to the resting state. This kind of signal is capable of propagating along neurons. (Purves, et al., 2004)

If we want to better understand what is happening during action potential, we need to consider the above mentioned voltage-gated ion channels. As already said, voltage-gated ion channels are responsible for generating action potential and thereby sodium Na^+ and potassium K^+ voltage-gated ion channels play a major role. Both channels have selective filters which make them permeable only for Na^+/ K^+ ions and activation gates that will open under specific circumstances and allow flow of the ions through the membrane. Besides that, Na^+ channels have an additional inactivation gate. For further text please refer to Figure 4. When exposed to an electrical stimulus Na^+ activation gates open and the positive Na^+ ions start moving from the extracellular space towards the cell making the membrane potential more and more positive. If the electric stimulus is strong enough (a certain threshold is passed) we will have action potential and the cell membrane will reach a positive peak. This phase is called depolarization. When the peak is reached Na^+ inactivation gate will start stopping Na^+ influx while K^+ activation gates open and K^+ ions start moving toward the extracellular space making membrane potential more and more negative so it can reach a resting state again. This phase is called repolarization. Before reaching a resting state, a membrane voltage goes below a resting voltage for a short period of time, so-called hyperpolarization (not shown in Figure 4). During hyperpolarization it is not possible to excite a cell. (Rattay, 1990; Alberts, et al., 2002)

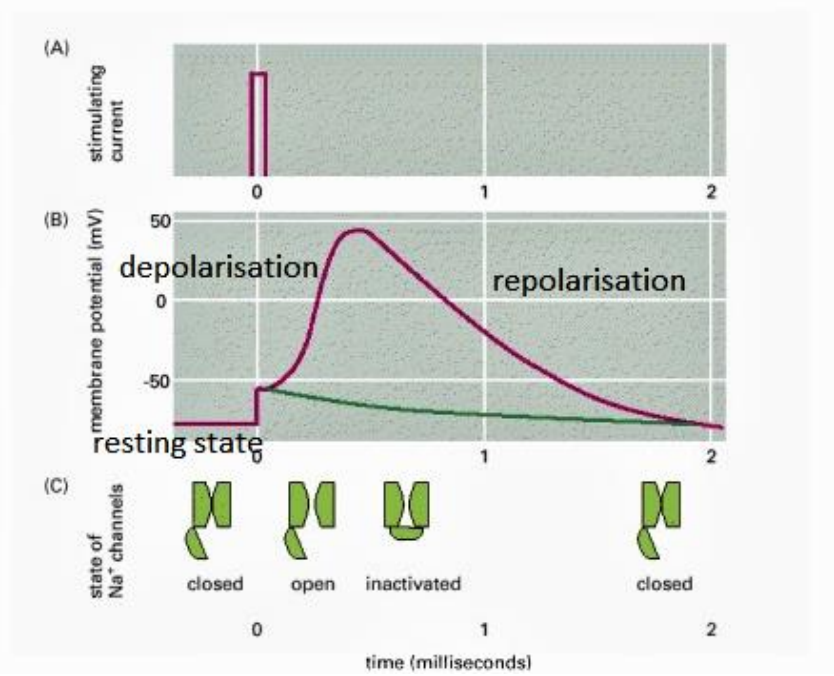

Figure 4: An action potential. On the first graph (A) we can see a short electric pulse that is used to excite a cell and generate an action potential. On the second graph (B) we can observe an action potential in red color i.e., changes in voltage membrane over time when the cell is excited. On the last graph (C) different states of Na^+ ion channels over time are shown. While the cell is still in resting state Na^+ channels are closed. At the moment when stimulus current is sent, Na^+ channels begin to open and Na^+ ions flow into the cell. After a threshold is exceeded, action potential is fired and the cell membrane is in a depolarized phase. When the peak of action potential is reached, inactivation gates of Na^+ channel are activated, and we observe the repolarization phase. At the end Na^+ channels are closed again and the membrane voltage is in a resting state. The green line in (B) shows how the membrane voltage would look like for the same stimulus current if there were no ion channels in the membrane. Figure and parts of caption adapted from Alberts, et al. (2002).

The important thing regarding action potential is that in order to get one, the electrical stimulus needs to pass a certain threshold value (it can depend on many different things). So, if the threshold is not passed, we will not have an action potential and if the threshold is passed, we will have an action potential of the same amplitude, regardless of the stimulus strength. This is called all or nothing law. (Rattay, 1990)

1.3 Retina

Retina is the nerve tissue of the eye that is placed at the back of the eyeball (Figure 5). Normally, the images (light) we observe pass through the eye´s lens and are then focused on the retina. Thanks to its light-sensitive properties, which we will discuss later, the main role of the retina is to sense the light that enters our eyes, to convert it

to electrical signals and at the end to send those signals further into the brain with the help of the optic nerve. (Cleveland Clinic, n.d.)

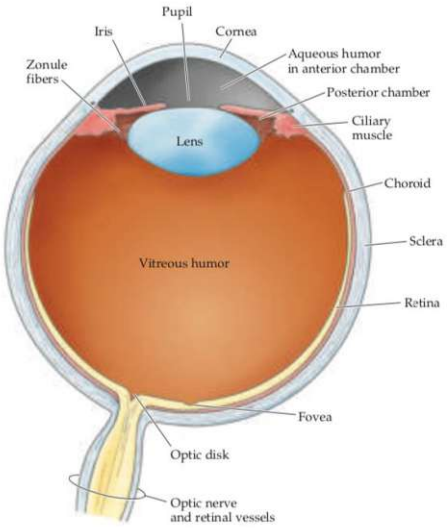

Figure 5: Anatomy of the eye. When light comes to the eye, it goes through the lens and is focused on the retina. After the signal is processed, it leaves the retina via optic nerve fiber and travels further into the brain. Figure from Purves, et al. (2004).

Interesting thing about retina is that it is a part of the central nervous system, although it is located at the back of the eyeball and thus is the only extension of the central nervous system that can be reached (visible) from the "outside world" (Mahabadi & Al Khalili, 2022). Retina consists of five (or six[1]) different nerve cell types: photoreceptors, bipolar cells, ganglion cells, horizontal cells and amacrine cells (Purves, et al., 2004). All retina´s cells and layers are shown in Figure 6.

1.3.1 Nerve cells in retina

In this part we are going to briefly go through retinal nerve cells. For their description following sources were used: Purves, et al (2004), Lamb (2016), Mahabadi & Al Khalili (2022) and Byrne & Dafny (n.d.). For a better understanding and insight into the neural structure of the retina, please refer to Figure 6.

[1] Some sources like Mahabadi & Al Khalili (2022) don´t group rods and cones into photoreceptors but consider them as two different nerve cell types.

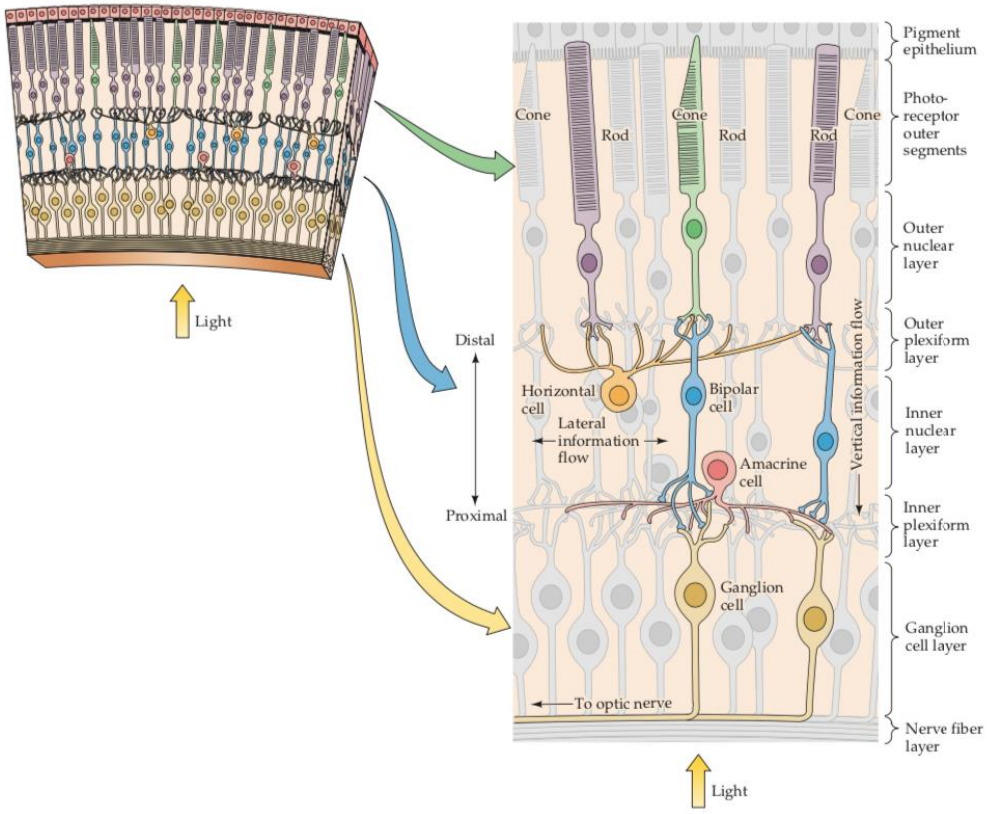

Figure 6: Structure of the retina. In this figure we can see the structure of the retina with its overall arrangement (left) and detailed arrangement of nerve cells and layers (right). At the distal end of the retina there is a pigment epithelium that supports the photoreceptors in their proper functioning. The cell bodies of retinal nerve cells are located at three different layers: outer nuclear layer (photoreceptors), inner nuclear layer (bipolar and amacrine cells) and ganglion cell layer (ganglion cells). Outer plexiform layer is a place where processes of bipolar cells, horizontal cells and photoreceptors are connected, while the inner plexiform layer is a place where processes of bipolar, amacrine and ganglion cells are connected. The nerve fiber layer is at the proximal end of the retina and contains axons of ganglion cells. Figure and caption from Purves, et al. (2004).

There are two types of **photoreceptors** in the retina: rods and cones. In total, about 95% of photoreceptors in humans are rods. Rods are concentrated in the outer, and especially in the peripheral retina. They have higher sensitivity to light compared to cones, but slow reaction speed. They also have low spatial acuity and low contrast sensitivity. Due to the mentioned characteristics, the rods enable us to see in poor lighting conditions i.e., in the dark. Cones, however, make up only 5% of the total number of photoreceptors in humans. They are located mainly in the central part of the retina and fovea (a place of the highest vision sharpness). What significantly distinguishes them from rods is their better sensitivity to different wavelengths (red, green and blue color). They are less sensitive to light (compared to rods and thus need

more light to be stimulated) but have a higher reaction speed and higher contrast sensitivity. Cones are also characterized by high spatial acuity. Cones thus enable our color and daytime vision. Both photoreceptor types are using a neurotransmitter called glutamate in order to communicate with the other retina neurons they are connected to (bipolar and horizontal cells).

Horizontal cells are regulating or modifying signals that are coming from photoreceptors before they go to the bipolar cells. They actually receive information from a small number of photoreceptors and then, based on that, give the information back to the larger number of surrounding photoreceptors. Due to the influence of horizontal cells, the image we see at the end is sharper and the contrast is adjusted according to the environment.

Bipolar cells are cells that connect photoreceptors with retinal ganglion cells, but also have synaptic connections with amacrine cells. Bipolar cells can be divided into two different ways: based on how they react to glutamate (neurotransmitter released by photoreceptors) or based on which type of photoreceptors they receive information from. Based on how they respond to glutamate, bipolar cells are divided into ON and OFF bipolar cells. Neither type of these cells makes an action potential but reacts to glutamate exclusively by being depolarized or hyperpolarized. ON type of bipolar cells are those cells that are hyperpolarized by glutamate and they enable recognition of bright objects in a darker environment. OFF type of bipolar cells is depolarized by glutamate and thus enable recognition of dark objects in a brighter environment. The second division is the division into cone and rod bipolar cells. As the name suggests, cone bipolar cells are connected to cone photoreceptors and can be either ON or OFF type of bipolar cells. However, the type of bipolar cells that are connected to the rod photoreceptors are exclusively ON type of bipolar cells. Most bipolar cells release neurotransmitter glutamate (like photoreceptors) in their synaptic clefts.

Amacrine cells are placed between bipolar cells (presynaptic connection) and retinal ganglion cells (postsynaptic connection). Amacrine cells are characterized by their diversity and based on their type they perform different functions in the retina and thus contribute to better visual function.

Retinal ganglion cells (RGCs) are the last line of nerve cells in the retina that transmit the signal in the form of action potential further to the brain via the nerve fiber layer and optic nerve (formed by RGC axons). In order to achieve that, RGC axons need to be long enough and need to have voltage-gated sodium channels so that action potential can propagate along them. RGCs are connected to and receive signals from the bipolar cells and amacrine cells. The release of glutamate from the bipolar cells excites and depolarizes RGCs which at the and results in the action potential. We distinguish two large groups of RGCs in the primate retina: M RGCs and P RGCs. P type of RGCs is better for detecting color and duration of visual stimulus, while M type of RGCs is better at detection of visual stimulus movement.

1.3.2 Retinal prostheses

Retinal prostheses are implants that help people who suffer from degenerative retinal diseases where photoreceptors or parts of the retina in the outer nuclear layer are damaged, while the optic nerves (together with RGCs) are not exposed to the damage and can perform their tasks properly. An example of this kind of disease is AMD (age-related macular degeneration), which occurs in elderly people and affects, as the name suggests, the macula – a place where the fovea is located. From that we can conclude that it affects a group of cone photoreceptors and thus makes our vision less sharp (problem with reading, seeing details etc.). Another example of a disease in which retinal prostheses could help is retinitis pigmentosa. Here, too, the photoreceptors are the ones exposed to damage, but unlike AMD, retinitis pigmentosa affects a larger area of the photoreceptors and can lead to complete blindness. Given that the disease is genetically caused, there is currently no cure for it. (Fitzpatrick, 2015)

The general idea of retinal prostheses is to use electrical stimulation to excite the remaining healthy cells (bipolar or ganglion cells for example), which in a healthy retina would be done via neurotransmitters sent by photoreceptors. Since the light-sensitive photoreceptors are damaged in this case, it is necessary to somehow convert the incoming light into an electrical signal. There are ideas to do this in two ways. The first is that we use a video camera to record the environment and from that data we get the information necessary for electrical stimulation. Another way is to use

microphotodiodes, which use the fact that the eye lenses work properly and convert the incoming light into an electrical signal. (Fitzpatrick, 2015)

Many retinal prostheses are using electrical stimulation to excite the remaining healthy retinal nerve cells. There are a few places where those prostheses could be placed and thus, we have different types of prostheses like epiretinal, subretinal, suprachoroidal (Figure 7). Epiretinal prostheses are located on the surface of the retina and thereby stimulate retinal bipolar or ganglion cells. They are minimally invasive because of their position. Subretinal prostheses are placed inside the retina (between retinal pigment epithelium and the photoreceptors) with the goal to stimulate remaining healthy bipolar or amacrine cells. The bipolar and amacrine cells are then supposed to excite retinal ganglion cells, as it would happen normally in healthy retina. Suprachoroidal prostheses are placed between choroid and sclera and have advantage of easy implantation. (Werginz & Rattay, 2014; Cohen, 2018)

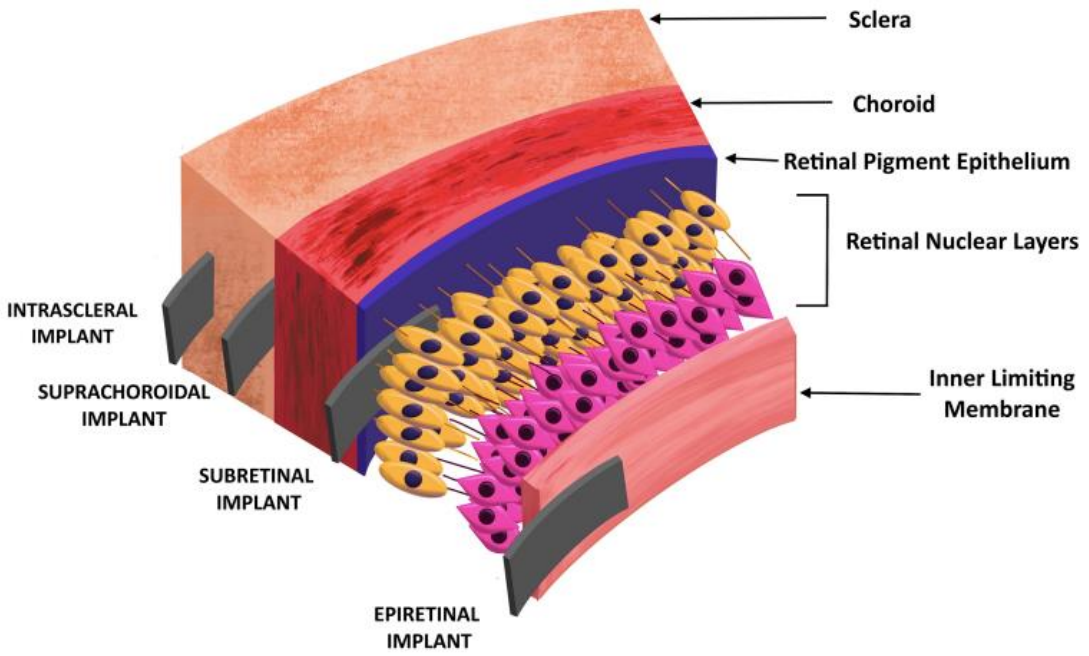

Figure 7: Different locations of retinal prostheses. Epiretinal implants are placed on the surface of the retina and thus have the ability to stimulate retinal ganglion cells or even bipolar cells. Subretinal implants are placed between subretinal implant and photoreceptors in order to stimulate bipolar or amacrine cells. Suprachoroidal implants are placed between sclera and choroid, while intrascleral implants are placed in the sclera. Figure from Ezeokafor, et al. (2021).

It is important to keep in mind that current retinal prostheses, due to a wide range of different problems, are unfortunately still unable to reproduce high-quality vision (Werginz & Rattay, 2014).

2 Modeling the Electrical Stimulation of Nerve Cells

In this section the main principles of nerve cells modeling will be described, with the focus on the electrical stimulation of the retinal ganglion cells. In addition, several specific models that are particularly relevant for this work will be presented.

Modeling of nerve cells is a very demanding task due to their great complexity. Therefore, nerve cell models vary from very simplified to very detailed, depending on which phenomenon we are investigating and how many resources we have. It is important to find a compromise between those two points, so that an overly simplified model does not lead to wrong results, and that we are, at the same time, still able to deal with the complex equations of the detailed model. In order to be able to model nerve cells, it is necessary to pay attention to two aspects. One of them is the modeling of conductances that are the result of the operation of voltage-gated ion channels and thus describe the dynamics of nerve cells. Another aspect is the specific morphology of neurons, which, depending on their function, enables them to communicate with other neurons in the optimal way. (Dayan & Abbott, 2005)

2.1 Modeling of cell membrane

Neuron modeling in this thesis is reduced exclusively to single neuron modeling, so the focus will not be on the transmission of signals and information from one neuron to another, but on the flow of signals through a single neuron and its response to different electrical stimuli. Bearing in mind the modeling of the single neuron, the main thing in addition to its morphology is the modeling of the cell membrane, which together with its voltage-gated ion channels, plays the main role in generating action potential and the transmission of signal through a single neuron.

2.1.1 Passive cell membrane

The following description of the passive cell membrane modeling (section 2.1.1) is based on its description in Gerstner, et al., (2014). To begin modeling the cell membrane, we can consider a passive membrane that as such does not contain voltage-gated ion channels. The way in which we can generally model cell membranes are electric circuits made on the basis of the elementary laws of electrical theory. The cell membrane, which consists primarily of phospholipids, prevents the completely free flow of molecules into and out of the cell (see section 1.2) and thus has the properties of an insulator and acts as capacitor with capacity C. If the cell membrane is excited by certain electric current pulse $I(t)$ that current cannot disappear or leave without any action, but it will charge the cell membrane. Bearing in mind that the cell membrane is not a perfect insulator, this charge will eventually "leak" through it and this behavior can be represented with a “leak” resistor with resistance R. In Figure 8 we can see an example of an electrical circuit which shows the above-described behavior. Resistor is here in parallel with capacitor, but in serial with a battery u_{rest} (represents resting potential of a cell membrane).

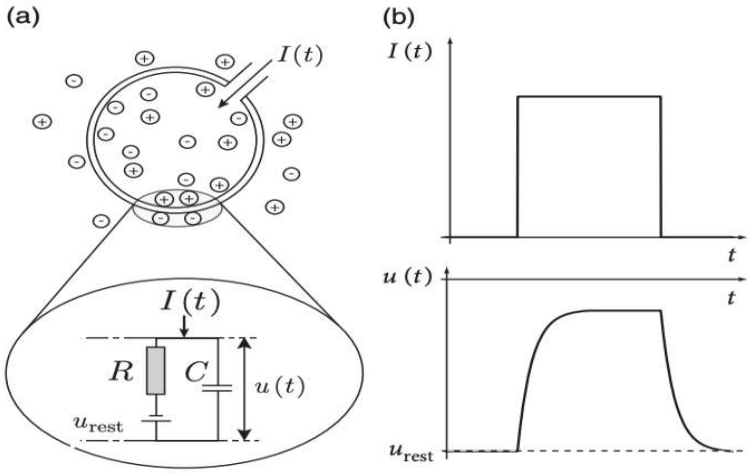

Figure 8: Electrical circuit model of passive membrane. In (a) we can see a model of passive cell membrane described as a capacitor that is in parallel with resistor and battery u_{rest}. In (b) we can observe change of membrane voltage $u(t)$ as a reaction on a current pulse $I(t)$. The voltage increases from resting potential u_{rest} and then comes back to it. Figure from Gerstner, et al. (2014).

As described in Gerstner, et al. (2014) using elementary laws of electric theory, we can analyze electrical circuit from Figure 8 with a set of formulas. First, we can split the incoming current into two parts: resistive current I_R and capacitor current I_C:

$$I(t) = I_R + I_C$$

We can further describe I_R as a voltage across the resistor $u_R = u(t) - u_{rest}$ divided through resistance R and I_C as $C\frac{du}{dt}$ and we get current across the membrane:

$$I(t) = \frac{u(t) - u_{rest}}{R} + C\frac{du}{dt}$$

From that we are getting a differential equation of a membrane voltage:

$$\frac{du}{dt} = -\frac{u(t) - u_{rest}}{RC} + \frac{I(t)}{C}$$

Due to absence of ion channels in this model, we have a linear resistor R. The model presented here is called the "leaky integrate-and-fire model" and is the simplest model of the group of integrate-and-fire models, that describes only a passive membrane behavior. It is important to mention that in general integrate-and-fire models are not able to analyze shape of action potential, but rather gain information from whether or not action potential occurs or predict spike times.

2.1.2 Active cell membrane

If we want to make a complicated model with ionic channels integrated in the membrane, we also need a way to determine effects of ionic channels on membrane voltage. Depending on whether we include only one type of ion or several of them at once, we will use the Nernst equation or the Goldman equation (Rattay, 1990; Pfützner, 2012):

Nernst equation describes effects of one type of ions/ion channels on membrane voltage and is described as following:

$$E_m = \frac{RT}{zF} ln \frac{[ion]_o}{[ion]_i}$$

thereby, R is defined as a gas constant, T is a temperature in Kelvin, F is a Faraday constant and z as an elementary charge. Concentrations of the specific ion outside and inside the cell are given with $[ion]_o$ and $[ion]_i$, respectively. Nernst equation can be used to determine static equilibrium of an ion (reversal potential[2]) which is defined as an equilibrium between chemical and electrical gradient.

Goldman equation is used to describe effects of different ions at once on the membrane voltage:

$$E_m = \frac{RT}{F} ln \frac{P_K[K]_o + P_{Na}[Na]_o + P_{Cl}[Cl]_i}{P_K[K]_i + P_{Na}[Na]_i + P_{Cl}[Cl]_o}$$

thereby, concentration of each involved ion is given as $[ion]_o$ for outside and $[ion]_i$ for inside concentration. With P_{ion}, permeabilities of each ion are given in $[cm/sec]$.

It is important to note that unlike the passive cell membrane model where we have a linear resistance R, in the case of an active cell membrane resistance R is highly nonlinear (Rattay, 1990).

2.1.3 Multi-compartment model

The model used in this thesis is developed as a multi-compartment model. The description of the multi-compartment model and the need for one in the first place, can be found in the book by Rattay (1990). Namely, when a signal travels through a cell, the action potential is not everywhere at once. The action potential propagates along the cell with the length of the excited region of only a few cm. Regardless of whether we are talking about a passive or active cell membrane, we need a way to describe the propagation of an action potential along the cell and that can be done using a so-called multi-compartment model. It consists of many single compartments (often cylindric) where each of them has its own circuit elements and thus properties and describes a reaction of a small part of the cell to the internal or external stimuli.

[2] This kind of equilibrium is also called reversal potential, see Gerstner, et al. (2014).

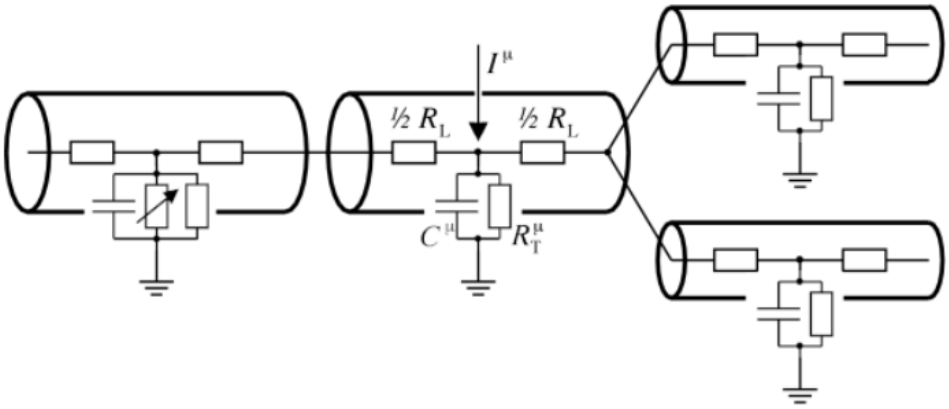

Figure 9: Multi-compartment neuron model. A model with several compartments and one bifurcation is shown in the figure. This type of modeling enables the individual description of each compartment, from determining the properties of individual electric circuits to the variation of geometric properties (e.g., diameters). Individual compartments can be described with the cable equation. Membrane capacitance is represented by C^{μ} and is together with R_T^{μ} (transversal resistance) coupled by a $r^{v\mu} = (R_L^v + R_L^{\mu})/2$ (longitudinal resistance), whereby R_L^v and R_L^{μ} represent longitudinal resistors. External stimulus reaching the compartment is represented by current I^{μ}. If resistors in an electrical circuit are defined as variable (see leftmost compartment) or not, it depends on the type of channels that are modeled (linear or nonlinear). Figure and caption from Gerstner, et al. (2014).

An example of such a multi-compartment neuron model with some more description details is presented in Figure 9 from Gerstner, et al. (2014). Thereby it is shown that besides electrical properties that can be defined individually for each compartment, we can also model different kinds of bifurcations or diameter variations. That is a very important characteristic of this type of modeling, especially if we keep in mind complex nerve cell morphology. It is also important to notice that both linear and nonlinear resistances are present in the model, which means it is suitable for both passive and active channels.

The mathematical formulation of the current flow in the multicompartment model is called cable equation which can be used both for intracellular and extracellular stimulation (Rattay, 1990; Rattay, 1999).

2.2 Hodgkin and Huxley model

In this section, the model that made a turning point in the modeling of nerve cells, the so-called Hodgkin and Huxley model, will be presented. This model, created after a series of experiments that led to description of dynamics of nerve cells by differential

mathematical equations, serves as the basis for more detailed and complex neuron models (Gerstner, et al., 2014).

In their paper from 1952 (Hodgkin & Huxley, 1952), Hodgkin and Huxley rounded off a series of their previous papers and based on them quantitatively described the dynamics of ion channels and the cell membrane. After the so-called voltage clamp experiments performed on a giant squid axon and the following results described in their above-mentioned previous papers, Hodgkin and Huxley quantified the dynamics of a single cell membrane compartment using the electric circuit presented in Figure 10. Combining the single compartments according to section 2.1 allows to study excitation and action potential conduction in the squid axon. C represents membrane capacity which produces capacity current, while ionic currents depend on constant (R_L) and variable resistances (R_{Na} and R_K). R_L describes small leakage current and thus needs constant resistance, while R_{Na} and R_K describe active voltage-gated sodium and potassium ion channels, respectively. Voltage-gated ion channels are changing with time and membrane potential and thus have non constant resistances (open and closed states, see section 1.2). Ionic currents I_{Na}, I_K and I_L which pass through given ion channels are proportional to their conductance g_{Na}, g_K and g_L. Battery voltages E_L, E_{Na} and E_K represent Nernst potentials for each ion type (see section 2.1.2). Besides g_{Na} and g_K, all other values (E_L, E_{Na}, E_K, g_L and C) can be assumed as constant.

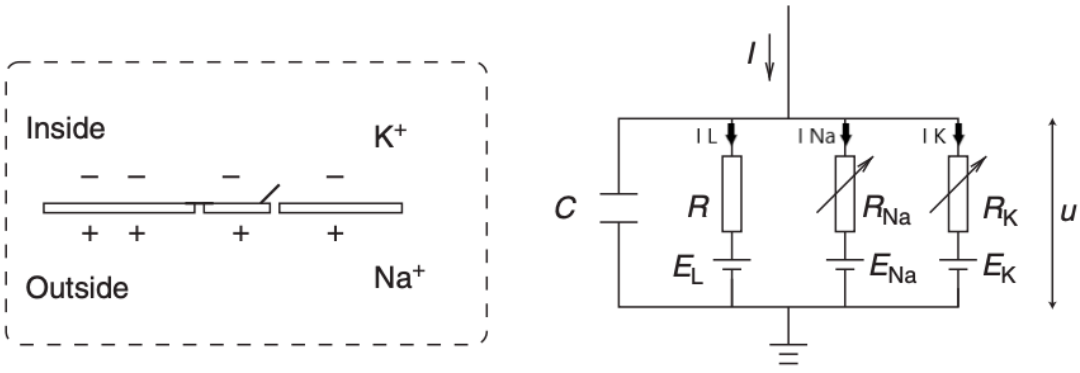

Figure 10: Electrical circuit of cell membrane by Hodgkin and Huxley. Membrane capacitance is represented by C, external current coming into the cell (compartment) by I. All ionic currents are represented by their constant (R_L for leakage current) or variable (R_{Na} for sodium and R_K for

potassium current) resistances. Battery voltages E_L, E_{Na} and E_K represent Nernst potentials for each ion type. Figure adapted from Gerstner, et al. (2014).

The whole Hodgkin and Huxley model is described with the four main nonlinear differential equations (Rattay, 1990):

$$\dot{V} = [-g_{Na}m^3h(V - E_{Na}) - g_K n^4(V - E_K) - g_L(V - E_L) + i_{st}]/c$$

$$\dot{m} = [-(\alpha_m + \beta_m)m + \alpha_m]k$$

$$\dot{n} = [-(\alpha_n + \beta_n)n + \alpha_n]k$$

$$\dot{h} = [-(\alpha_h + \beta_h)h + \alpha_h]k$$

Thereby, the first equation describes a membrane voltage V in relation to ionic currents. Capacity of membrane is described through its density c, while applied stimulus current is described through its density i_{st} and neuron ionic currents are described through their conductances. The variables m, h, n that are given with the remaining three differential equations are so-called gating variables which describe the open probabilities of the sodium and potassium ion channels. Thereby m and n are activating variables, while h is inactivating. Opening rates are represented by α and closing rates with β and they are functions of membrane voltage V. As we can see in the first equation, the variables m and h are related to Na^+ ion channels. Contrary to that, state of K^+ ion channels is given only through their activation gate and thus here described with only one gating variable n. Notice that no gating variables are needed for leakage channels for a very simple reason: they are always open and thus their opening probability is always one. When determining the gating variables, in addition to the membrane voltage, the temperature also plays a role through a temperature coefficient k. The experiments from Hodgkin and Huxley in 1952 were performed at the temperature of $T = 6.3$℃. With temperature coefficient $k = 3^{0.1T-0.63}$, we can adjust our model to lower/higher temperatures. (Hodgkin & Huxley, 1952; Rattay, 1990)

2.3 Fohlmeister and Miller model

Fohlmeister and Miller model (Fohlmeister & Miller, 1997a) is a model on which simulations in this thesis are based and performed and thus we need to look at it with more details. It is a part of the retinal ganglion cell model family created by a group of scientists from 1990 onwards. The first model created in 1990 by Fohlmeister, Coleman and Miller is based on the Hodgkin and Huxley model and represents the starting point for future retinal models, also known as Fohlmeister-Coleman-Miller (FCM) model family (Guo, et al., 2014).

According to Guo, et al. (2014), we can divide FCM model family to several groups based on the purpose and degree of complexity of each model. These groups are represented in Figure 11 by different colors. Thereby, black color represents the single-compartment models (Hodgkin & Huxley, 1952; Fohlmeister, et al., 1990; Fohlmeister & Miller, 1997a; Boinagrov, et al., 2010; Kameneva, et al., 2011; Boinagrov, et al., 2012). Purple color represents block compartment models (Schiefer & Grill, 2006; Werginz, et al., 2014). Morphologically-realistic models are shown in red color and besides models for retinal ganglion cells (Velte & Miller, 1995; Fohlmeister & Miller, 1997b; Sheasby & Fohlmeister, 1999; Greenberg, et al., 1999; Schachter, et al., 2010; Fohlmeister, et al., 2010; Jeng, et al., 2011; Tsai, et al., 2012; Guo, et al., 2013; Maturana, et al., 2014) there are also two amacrine cell models (Velte & Miller, 1997; Miller, et al., 2006). On the tissue level there are discrete-neuronal network models marked in green (Rattay, et al., 2003; Rattay & Resatz, 2004; Resatz & Rattay, 2004; Publio, et al., 2009; Publio, et al., 2012) and continuum models marked in blue (Dokos, et al., 2005; Yin, et al., 2010; Yin, et al., 2011; Abramian, et al., 2011; Joarder, et al., 2011; Al Abed, et al., 2012; Abramian, et al., 2014).

REMARK: Since the Figure 11 from Guo, et al. (2014) contains references for mentioned models, those references are grouped according to Figure 11 and listed above, so they can be accessed in the case of interest.

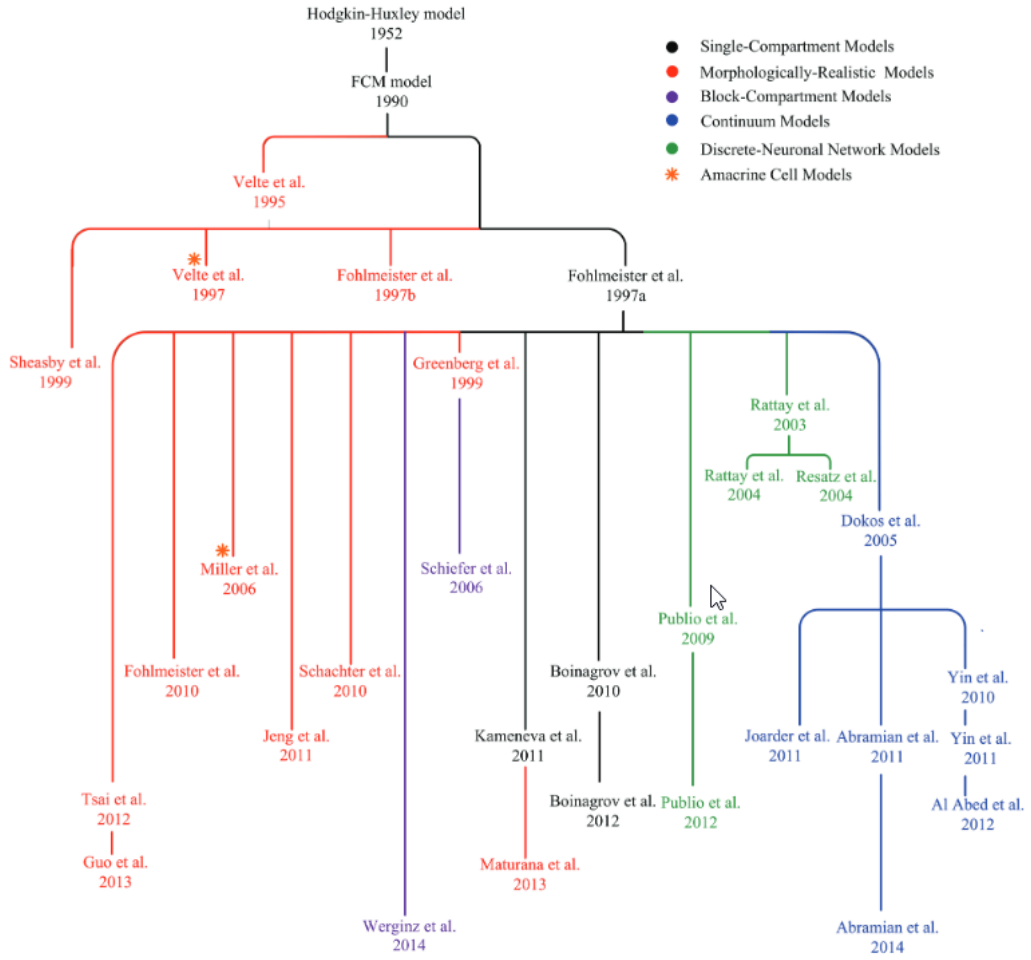

Figure 11: Fohlmeister-Coleman-Miller (FCM) model family. The first FCM model was based on the famous Hodgkin and Huxley model from 1952 and belongs to a group of so-called Single-Compartment Models. With that model as a starting point, many other more complex models were later created on both single-cell level (Morphologically-Realistic Models, Block-Compartment Models) and tissue level (Continuum Models, Discrete-Neuronal Network Models). Besides the retinal ganglion cell model, FCM model from 1990 and its derivatives were also the basis for some amacrine cell modes. Figure and parts of caption from Guo, et al. (2014).

In the RGC model from Fohlmeister, et al. (1990), the model of tiger salamander retina was presented. The retinal ganglion cell was described with five nonlinear channels (currents): Na^+, Ca^{2+}, non-inactivating K^+ (delayed rectifier), inactivating K^+ (A type) and Ca^{2+} activated K^+channels. As we can see, in contrast to the Hodgkin and Huxley model from 1952, this model is characterized by one sodium, one calcium and three different potassium channels. In order to preserve input resistance continuity between model and experiment, this model was updated in 1997 with one additional leakage channel and we got the so-called Fohlmeister and Miller model (Fohlmeister & Miller, 1997a).

If we exclude the Ca^{2+} activated K^{+}channels, which are gated by Ca^{2+}, all other channels are voltage-gated channels and are modeled accordingly. The equation for voltage V across the membrane is given by Fohlmeister & Miller (1997a):

$$\dot{V} = \left[-\bar{g}_{Na} m^3 h (V - E_{Na}) - \bar{g}_{Ca} c^3 (V - E_{Ca}) - (\bar{g}_K n^4 + \bar{g}_A a^3 h_A + \bar{g}_{K,Ca})(V - E_K) - \bar{g}_L (V - E_L) + i_{st}\right]/c$$

And gating variables of the voltage-gated ion channels (m, h, c, n, a, h_A) are modeled with the differential equations from Hodgkin & Huxley (1952):

$$\dot{x} = -(\alpha_x + \beta_x)x + \alpha_x$$

However, $g_{K,Ca}$ is ligand gated by Ca^{2+} ions and is modeled with following equation (Fohlmeister, et al., 1990):

$$g_{K,Ca} = \bar{g}_{K,Ca} \frac{([Ca^{2+}]_i/(Ca^{2+})_{diss})^2}{1 + ([Ca^{2+}]_i/(Ca^{2+})_{diss})^2}$$

where $Ca^{2+}{}_{diss}$ represents dissociation constant and $[Ca^{2+}]_i$ represents actual Ca^{2+} ion concentration.

Although the base for this model is the Hodgkin and Huxley model, there is a difference in conduciveness of those two models. The Fohlmeister and Miller model is significantly less conductive compared to the Hodgkin and Huxley model in the resting and subthreshold states (Fohlmeister & Miller, 1997a).

A local (soma) form of the model developed for this thesis, which is based on a model from Fohlmeister & Miller (1997a) was used to present above-mentioned ionic currents, gating variables and resulting action potential (Figure 12). Thereby, intracellular stimulation was used in order to send anodic stimulus (a) which is strong enough to initiate action potential (b). The difference in the behavior of activating (m, c, n, a) and inactivating variables (h_A and h) can be observed in (c). Resulting ionic currents densities are represented in (d) and their influence on action potential can be analyzed. During depolarization phase, we observe that the sudden rise in membrane voltage seems to come only from sodium current I_{Na}, while calcium current I_{Ca} is initially delayed. After that begins repolarization phase and the main role is now played

by two potassium currents: delayed rectifier I_K and A type current $I_{K,A}$. The third potassium current $I_{K,Ca}$ overlaps with leakage current I_L shows no significant contribution to action potential.

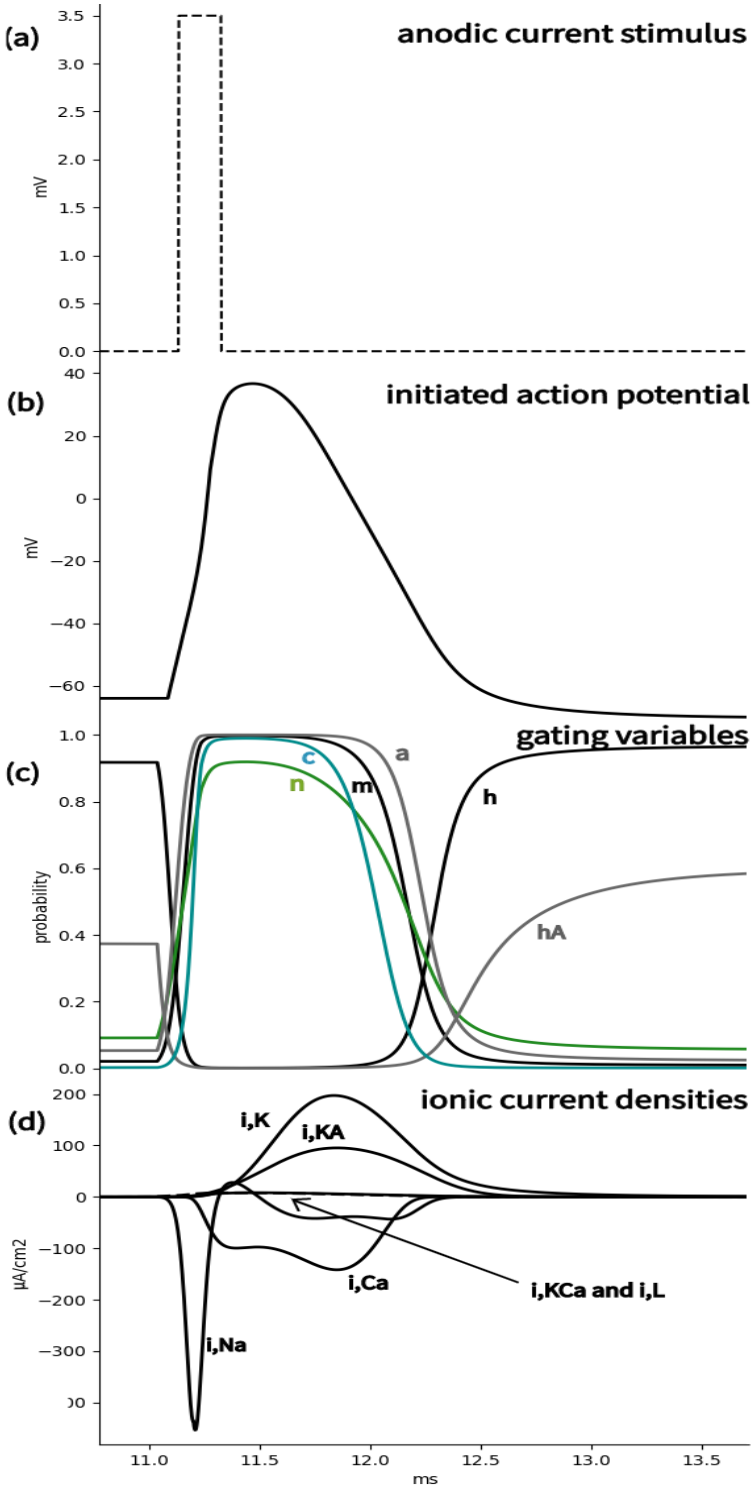

Figure 12: Action potential, gating variables and ionic currents of Fohlmeister and Miller model. For this representation a simple local model consisting only of soma divided into 21 segments was

developed. Intracellular square current stimulus (anodic) is applied (a). This stimulus was strong enough to initiate action potential (b). All gating variables are shown in (c). Thereby, black color represents sodium related activating and inactivating variables m and h, while gray color represents A type potassium related activating and inactivating variables a and hA. Green color represents delayed rectifier potassium gating variable n and cyan represents to calcium related gating variable c. Resulting ionic current densities are shown in (d), where we can observe strong inward sodium current at the beginning of action potential and with some delay relatively strong outward potassium current at the fall of action potential.

In addition to describing retinal ganglion cell dynamics with the above-mentioned differential equations, Fohlmeister and Miller also investigated influence of different ion channels on action potential spikes and interspike intervals using spike train analysis (Fohlmeister, et al., 1990; Fohlmeister & Miller, 1997a). In Figure 13 the influence of ionic currents on action potential is shown. We can see that the ionic currents presented in the original paper are comparable with the one resulting from our local (soma) model (Figure 12).

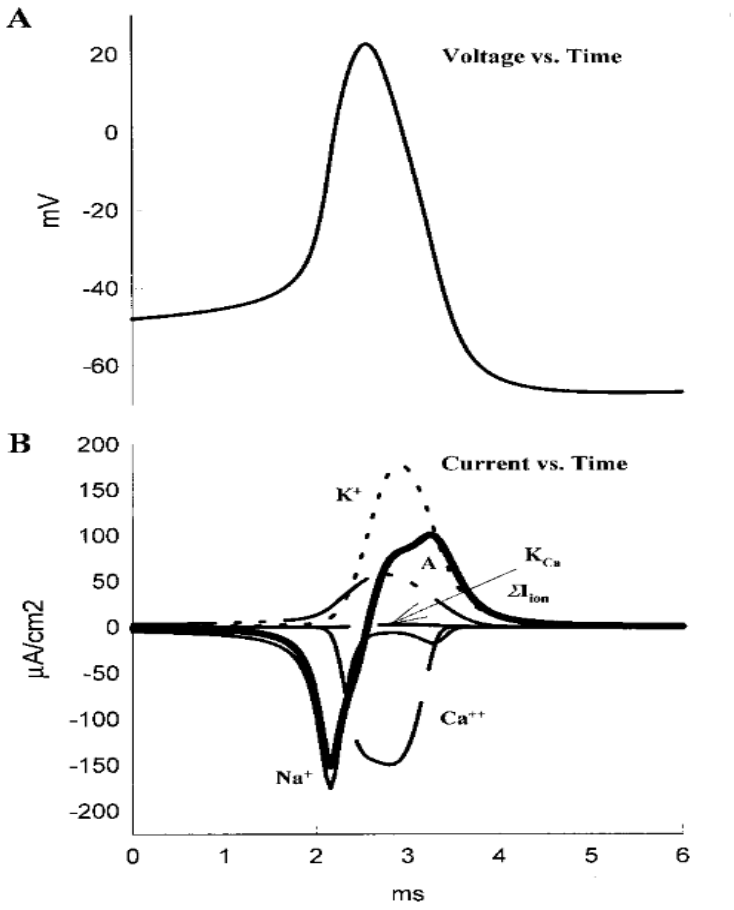

Figure 13: Influence of ionic currents (B) on action potential (A). The depolarization phase is characterized by the influence of sodium ionic currents, with a delayed reaction of calcium current, while the repolarization phase is characterized by the impact of delayed rectifier and A type of potassium currents. The role of calcium gated potassium current is minor. The

transmembrane current resulting from all five ionic currents is shown with a bold line. Figure and parts of caption from Fohlmeister & Miller (1997a).

After spike train analysis, Fohlmeister and Miller divided five ionic currents present in the model based on their impact throughout the impulse train into two groups: small and large currents. Small currents like $I_{K,Ca}$ or I_L may play significant role at controlling interspike intervals, while large currents like I_{Na}, I_K, $I_{K,A}$, I_{Ca} control impulse generation and contribute to action potential (Figure 13). In addition to influence on interspike interval, $I_{K,Ca}$ seems to have an important impact on stabilizing the cell and thus preventing spontaneous firing.

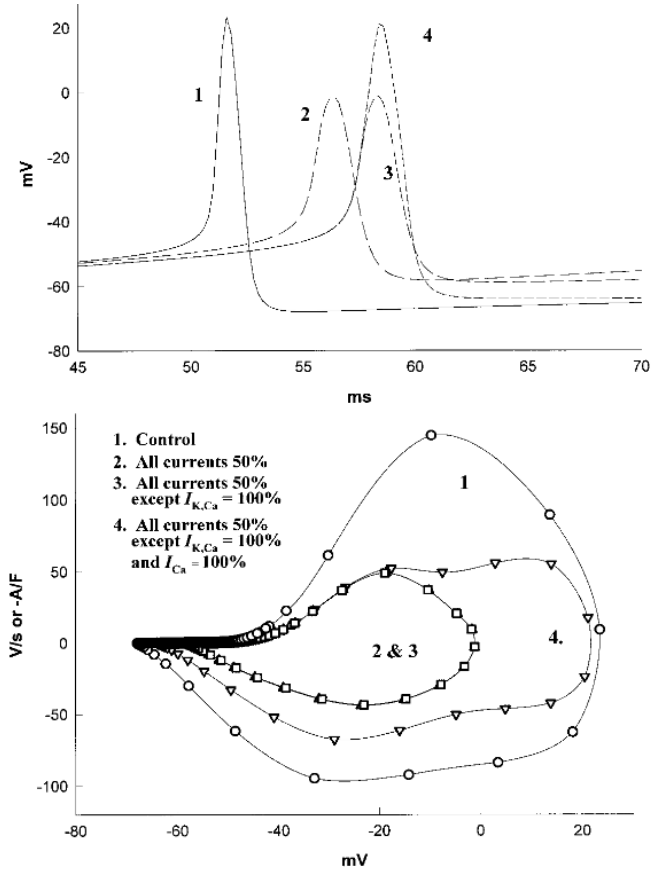

Figure 14: Influence of $I_{K,Ca}$ and I_{Ca} on action potential and interspike interval. With one control and three modified groups of ionic currents, their influence on the action potential and interspike interval is shown, with special emphasis on the role of $I_{K,Ca}$ and I_{Ca}. After measuring action potential one (AP1) of the control group, all ionic currents are reduced by 50% and AP2 is observed as a delayed version of AP1 with decreased amplitude. Then $I_{K,Ca}$ is increased back to its initial value and thereby, it seems that $I_{K,Ca}$ has no impact on shape of action potential or its amplitude, but rather on further hyperpolarization and delay (AP3). In contrast to it, no delay is observed with increasing I_{Ca} to its initial value, while increase in amplitude height is obvious. Figure and parts of caption from Fohlmeister & Miller (1997a).

Figure 14 caption from Fohlmeister & Miller (1997a) can deepen our understanding of the roles of $I_{K,Ca}$ and I_{Ca} in this model. In the Trace 1 control set of unchanged ionic currents is applied and action potential number one (AP1) is shown. In the Trace 2 all currents are reduced by 50% and we observe AP2 with decreased amplitude and delayed impulse (longer interspike interval). In the Trace 3 $I_{K,Ca}$ was increased back to initial state, while all other currents remained reduced by 50%. Now we observe AP3 that has identical shape (amplitude and waveform) as AP2 but is delayed even more and shows further hyperpolarization. In the Trace 4 both $I_{K,Ca}$ and I_{Ca} were increased back to initial state, while all other currents remained reduced by 50%. In contrast to AP3, the amplitude of AP4 increases significantly, while the beginnings of the AP3 and AP4 overlap. From this it can be suggested that, as already stated, $I_{K,Ca}$ plays no role in the shaping of the action potential or the height of its amplitude, but above all in the regulation of the interspike interval, while I_{Ca} significantly affects the amplitude of the action potential.

It is important to notice that although their train spike analysis also suggests that both $I_{K,Ca}$ and I_{Ca} are important factors in regulating impulse frequency, all channels contribution to it should not be neglected (Fohlmeister & Miller, 1997a).

The Fohlmeister and Miller model from 1997 has a temperature limitation i.e., the impossibility of temperature variation, thus all simulations were performed at a temperature of 22°C. This was changed with the new model from 2010 (Fohlmeister, et al., 2010), where models of cat and rat retinal ganglion cells were presented. Here, the temperature is used as an independent variable and varied in range of $7 - 37$°C. Although the model from 1997 has no temperature dependency, it was used in this thesis because of its stability regarding spontaneous firing.

3 Dynamic Range and Relative Spread

Dynamic range, together with the relative spread, is the main phenomenon being investigated in this thesis and as such requires more detailed description. In order to understand the concept of dynamic range and relative spread and the need to define them in the first place, it is necessary to first look briefly at the most common models of nerve cells and the principles on which nerve cell behavior is defined.

Since many other models are developed from the famous Hodgkin and Huxley model (Rattay & Aberham, 1993; Guo, et al., 2014), we can take that model as a reference. As already described in the section 2.2, the model describes the relation of membrane voltage and ionic currents (through sodium and potassium ion channels) and thus their reaction to internal or external stimuli that at the end leads to generation of action potentials. Open probabilities of sodium and potassium channels are thereby modeled in deterministic way with three gating variables (m, h, n) that depend only on membrane voltage and have no random fluctuations. These random fluctuations are normally the result of the channel noise present in the nerve cells that emerges from random opening and closing of voltage-gated ion channels. Channel noise is always present and measurable and as such should be part of nerve cells modeling (White, et al., 2000). Unfortunately, because of the lack of stochastic components, channel noise is neglected in standard Hodgkin and Huxley based models. Thus, when we stimulate nerve cell using a Hodgkin and Huxley based model with a train of 10 pulses (all of them having threshold amplitude) we expect them to generate exactly 10 APs (one for each pulse). In contrast to that, using experimental methods will lead us to different results. As a result of random fluctuations in ion channels, if we experimentally send a train of 10 pulses with threshold stimulus amplitude, we will not evoke and measure all 10 APs, but can expect about 50% of pulses to generate AP. The example of this behavior is observed in Figure 15 from Boinagrov, et al. (2012), where they performed experimental measurements on rat retinal ganglion cell. As we can see, there is a range of stimulus intensity in which the probability of evoking an action potential pro pulse

in a series of pulses increases from 0 to 1 with increased stimulus intensity. Two important terms that describe relation between stimulus intensity and spiking probability and thus give stochasticity information on the cell behavior are relative spread (Verveen, 1960) and dynamic range (Shepherd & Javel, 1997) (detailed description follows).

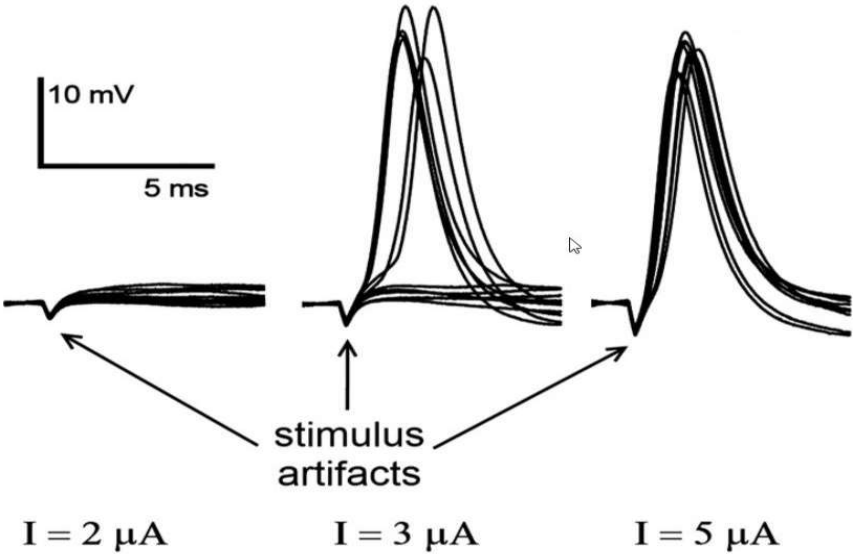

Figure 15: Stochasticity in AP generation (experimental measurements). A rat retinal ganglion cells were stimulated with a train of rectangular cathodic pulses of different amplitudes. Regardless of the strength of stimulus amplitude (subthreshold, threshold or suprathreshold) we observe stochastic behavior in all three responses. With subthreshold stimulus amplitude of 2 μA no action potential is evoked, but noise is observed in differences of responses (lines have no complete overlap). With threshold stimulus amplitude of 3 μA approximately 50% of actions potentials are evoked. When stimulus amplitude is enough above the threshold (in this case 5 μA), all action potentials are evoked, but noise is still observed (no complete overlap of evoked action potentials). Figure adapted from Boinagrov, et al. (2012).

3.1 Relative spread

Since the beginning of 1960, Verveen has investigated the phenomenon of spiking probability and threshold fluctuations of the nerve cells (Verveen, 1960; Verveen, 1962). From his experiments (Verveen, 1960), he showed that there is characteristic relationship between stimulus intensity and spiking probability that can be described with sigmoid function or approximated with integrated Gaussian curve (cumulative distribution function of normal distribution)[3]. In Figure 16 we observe this

[3] In the original paper from Verveen (1960) this function is referred to as integral of the function of De Moivre.

characteristic relationship based on Verveen´ s experimental results that led him to characterize the relationship by two parameters of the given curve: threshold and spread. Threshold is defined as a mean of the integral (value of the stimulus intensity where the spiking probability reaches 50%, expressed in current intensity), while spread is defined as standard deviation of the integral (width of the curve, also expressed in current intensity). The quotient of the two parameters (spread normalized to the threshold) is defined as relative spread (RS). RS is thus used as a measure of stochasticity and has no dimension. According to the same paper (Verveen, 1960) RS shows no dependency on strength and duration of the stimulus current.

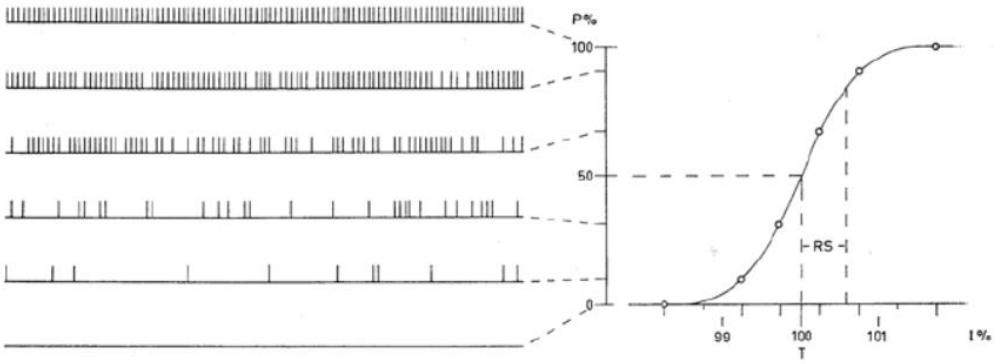

Figure 16: Relationship between stimulus intensity and spiking probability. On the left side we can see trains of evoked action potentials for six different stimulus intensities. Note that for the bottom line of trains no APs were generated, and for the top one all of them were generated. In between we observe different spiking probabilities that are following sigmoid curve or integrated Gaussian curve. Relative spread is also shown in the figure. Figure from Verveen (1960).

3.2 Dynamic range

Another important measure of stochasticity of nerve cells (besides relative spread) is dynamic range (DR). Dynamic range is defined in paper from Shepherd & Javel (1997) as the stimulus intensity range in which spiking probability increases from 0.1 to 0.9. In their paper Shepherd and Javel investigated electrical stimulation and dynamic range of the auditory nerves in animals with different levels of cochlear pathology. The variation in dynamic range among auditory units is shown in Figure 17, where DR is given in dB in the brackets. Note that the relationship between spiking probability and stimulus intensity shows the same sigmoid curve, as described in Figure 16 from Verveen.

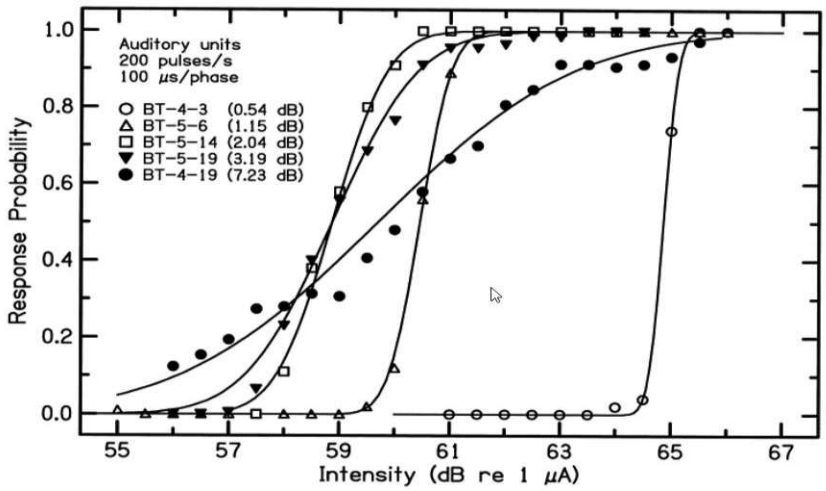

Figure 17: Variations in dynamic range among auditory units. DR is given in dB in the brackets. Despite the variation of DR that is obvious by looking at stimulus intensity range from 0.1 to 0.9 spiking probability, all of the curves indicate the same sigmoid shape and were fitted by integrated Gaussian curve, like described in (Verveen, 1960). Figure and parts of caption from Shepherd & Javel (1997).

Given that both relative spread and dynamic range are described through the parameters of the integrated Gaussian curve, it can be assumed that there is a relationship between the two terms. This relationship has been recently investigated and described by Rattay and Tanzer in their works (Tanzer, 2021; Rattay & Tanzer, 2022a; Rattay & Tanzer, 2022b). They showed that there is a linear relationship between relative spread (standard deviation of integrated Gaussian curve normalized to threshold) and dynamic range normalized to threshold. Dynamic range is larger than relative spread by the factor of 2.56:

$$RS = \frac{\sigma}{\mu} \approx \frac{DR}{2.56\mu}$$

3.3 Noise modeling

Like already mentioned, Hodgkin and Huxley based models are defined as deterministic models and thus miss a stochastic nature of nerve cells and their random fluctuations that are normally observed in experimental measurements like we have seen until now in Verveen (1960), Shepherd & Javel (1997) and Boinagrov, et al. (2012). Deterministic models are sufficient when investigating threshold values that are needed to generate action potential in different nerve cells or parts of specific nerve

cell, but if we want to analyze their stochastic behavior using dynamic range or relative spread, then we need to find a method for inserting stochastic component (noise) into the Hodgkin and Huxley based models (Rattay & Tanzer, 2022b).

Different papers investigated and compared methods of adding channel noise to the existing deterministic models (Mino, et al., 2002; Goldwyn, et al., 2011; Goldwyn & Shea-Brown, 2011). In the study from Goldwyn & Shea-Brown (2011) several approaches of noise insertion were reviewed and analyzed based on Hodgkin and Huxley model from 1952[4]. They classified reviewed noise insertion approaches into three groups: current noise, subunit noise and conductance noise. All following equations and explanations of these three groups are based on the mentioned study from Goldwyn & Shea-Brown (2011):

With **current noise** approach, noise term $\xi_v(t)$ is added to the first (main) Hodgkin and Huxley equation (see section 2.2) as following:

$$\dot{V} = [-g_{Na}m^3h(V - E_{Na}) - g_K n^4(V - E_K) - g_L(V - E_L) + i_{st} + \xi_v(t)]/c$$

where $\xi_v(t)$ represents Gaussian white noise and is assumed to depend only on the time t. The advantage of this approach lies in its simplicity, but its deficiency is reflected in two important aspects. Since channel noise is a consequence of random fluctuations reflected in the closing and opening of ion channels, it suggests that noise term $\xi_v(t)$ should also depend on membrane voltage V or gating variables (m, h, n). The other negative aspect can be seen in the fact that it is hard to determine noise intensity with this approach.

With **subunit noise** approach, noise term $\xi_x(t)$ is added to the remaining three Hodgkin and Huxley equations. Since the usual understanding is that different ion channels (for example sodium and potassium) are independent of each other, the three equations that describe gating variables (m, h, n) and thus opening/closing probability of specific ion channels may be a good place for positioning the noise:

$$\dot{m} = [-(\alpha_m + \beta_m)m + \alpha_m + \xi_m(t)]$$

[4] Their discussion applies actually to any conductance-based model, but the Hodgkin and Huxley model (Hodgkin & Huxley, 1952) was taken as an example.

$$\dot{n} = [-(\alpha_n + \beta_n)n + \alpha_n + \xi_n(t)]$$

$$\dot{h} = [-(\alpha_h + \beta_h)h + \alpha_h + \xi_h(t)]$$

where $\xi_x(t)$ represents Gaussian white noise and is assumed to depend on time t and may depend on specific gating variable (m, h, n) or V.

The last approach classified and reviewed by Goldwyn & Shea-Brown (2011) is the so-called **conductance noise** approach. In this approach noise term $\xi_x(t)$ is again applied to first Hodgkin and Huxley equation, but this time straight to the fraction of open channels (in Hodgkin and Huxley model represented by m^3h for sodium channels and n^4 for potassium channels):

$$\dot{V} = \begin{bmatrix} -g_{Na}(m^3h + \xi_{Na}(t))(V - E_{Na}) - g_K(n^4 + \xi_K(t))(V - E_K) \\ -g_L(V - E_L) + i_{st} \end{bmatrix} / c$$

where $\xi_x(t)$ represents Gaussian white noise and is assumed to depend on time t and may depend on fraction of open channels or V.

3.3.1 Rattay´ s current noise approach

The above-explained methods of noise injection into Hodgkin and Huxley based models are a brief overview of the possibilities that serve us to create an overview of possible solutions. But method of noise insertion used in this thesis is based on so-called Rattay´ s current noise approach[5], where the defined noise current is included in each active compartment of the model.

In 1995 Rubinstein (Rubinstein, 1995) presented a model of the amphibian node of Ranvier, where the stochastic component included only kinetics of single voltage-gated sodium channels. Thereby, he demonstrates that relative spread shows proportion to $1/\sqrt{N}$ (where N represents voltage-gated sodium channels) and suggest that this kind of modeling could be suitable for predicting stochastic behavior, since the model results coincide with the results measured in experiments.

[5] This method in some literature is referred to as Rattay´ s current noise approach (see Tanzer (2021)).

Following Rubinstein and his work from 1995 where noise term seems to be proportional to the square root of the number of voltage-gated sodium channels in the given compartment, Rattay discussed and proposed in his works (Rattay, 2000; Rattay, et al., 2001) a method for noise insertion. The noise is thereby represented through a noise current I_{noise} that describes random fluctuations of voltage-gated ion channels and is added to the standard ionic current (defined through product of membrane area A_n and ionic current density $i_{ion,n}$) as following:

$$I_{ion} = A_n i_{ion,n} + I_{noise,n}$$

The noise current $I_{noise,n}$ of a specific compartment is then defined as following:

$$I_{noise,n} = GAUSS\, k_{noise} \sqrt{A_n g_{Na}}$$

Where $GAUSS$ represents Gaussian noise current with the mean $\mu = 0$ and standard deviation $\sigma = 1$ that changes its value according to the defined time step dt; k_{noise} is a constant factor common to all compartments given in $\mu A/\sqrt{mS}$; A_n represents membrane area in cm^2 and g_{Na} represents maximum sodium conductance given in mS/cm^2.

As already described, Gaussian noise current $GAUSS$ is controlled by defined time step dt, since it changes its value according to it. In the first studies where Rattay´ s current noise approach was used (Rattay, 2000; Rattay, et al., 2001), as well as in the newest one (Rattay & Tanzer, 2022a; Rattay & Tanzer, 2022b) a standard time step of $dt = 0.0025\, ms$ was used. In their recent work (Rattay & Tanzer, 2022b), Rattay and Tanzer defined an equation for noise factor k_{noise} adjustment based on change of time step dt:

$$k_{noise}(dt) = \sqrt{\frac{0.0025}{dt}}\, k_{noise}(0.0025)$$

It is important to emphasize that this equation is suitable only for the cases when time step dt in not too large, or to be more precise for $dt \leq 0.005$.

3.4 RS and DR as function of diameter

After defining relative spread as a measure of nerve cell stochasticity in 1960 (Verveen, 1960), Verveen investigated the relationship between RS and diameter in his further studies (Verveen, 1962). Thereby he performed experiments on frog, cray-fish and cuttle-fish axons and saw that with increased diameter, RS decreases. At the end he demonstrated linear relationship between $\log RS$ and $\log d$, where d represents diameter of given part of nerve cell:

$$\log RS = -1.5 - 0.8 \log d$$

The relationship between RS and diameter, obtained from the Verveen´ s experimental measurements, is presented in Figure 18.

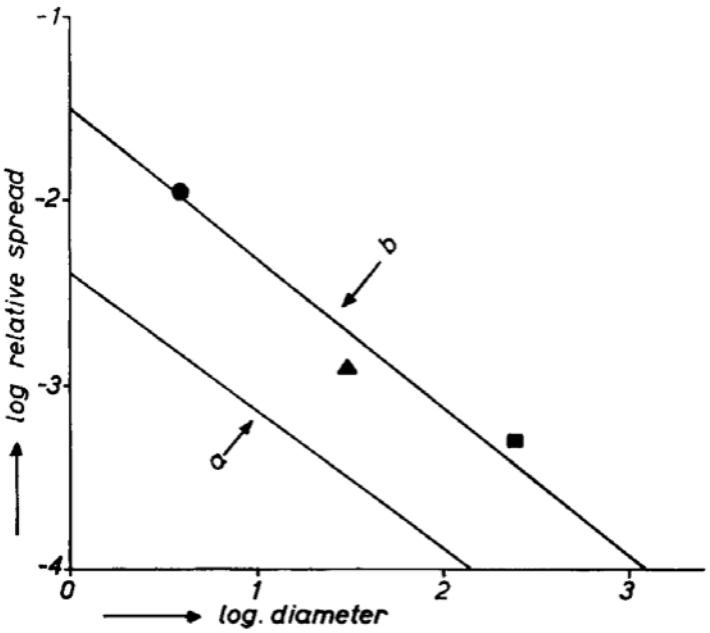

Figure 18: Relationship between RS and diameter. The results of Verveen´ s experiments show an inversely linear relation between log RS and log d. With increased diameter, RS decreases. Circle represents axon measurements on frog, triangle on cray-fish and square on cuttle-fish. Line a represents the theoretical relation, while line b represents the least square line. Figure and caption from Verveen (1962).

The similar relationship between RS and diameter was reported by Rattay & Tanzer (2022b). They investigated this relationship on the compartment model of a myelinated axon using three different Hodgkin and Huxley based models and Rattay´ s current noise approach. After adjusting k_{noise} parameters for each model, the logarithmic equations were comparable to the one reported from Verveen. In the same study,

Rattay and Tanzer also concluded that RS increases linearly with k_{noise} parameter (Figure 19).

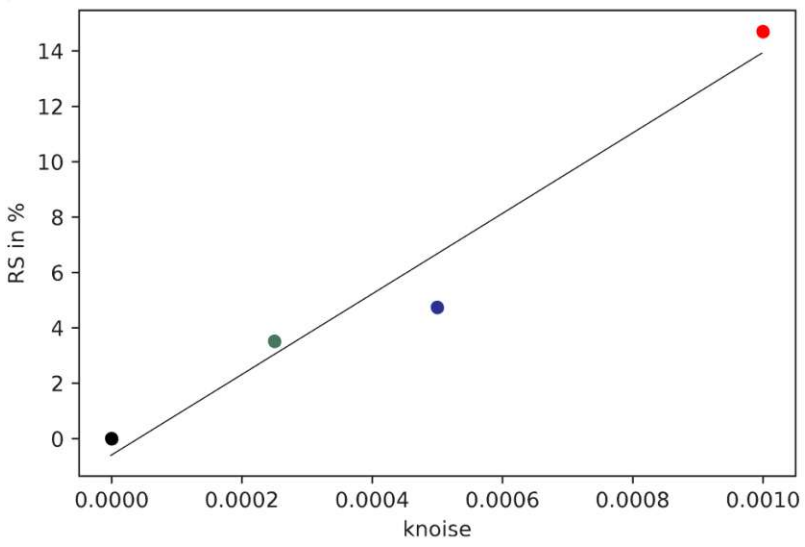

Figure 19: Relationship between RS and k_{noise}. RS was calculated for three different k_{noise} values: $k_{noise} = 0.00025$ (green), $k_{noise} = 0.0005$ (blue) and $k_{noise} = 0.001$ (red). The relationship seems to be linear, with increased k_{noise}, RS also increases. Figure and caption from Rattay & Tanzer (2022b).

Since it is suggested that DR and RS differ only in the constant factor (see section 3.2), it can be assumed that DR shows a similar relationship to diameter and that with increased diameter, DR decreases.

3.5 DR investigation in this thesis

Retinal prostheses developed until now are unfortunately still unable to reproduce high-quality vision due to different reasons (Werginz & Rattay, 2014). Thus, any new aspect of the influence of electrical stimulation on RGCs may be very important for needed improvements, which also includes DR. Several recent experimental and modeling RGCs studies included stochastic cell behavior (spiking probability, DR, RS) to some degree in their research, while searching for retinal prosthesis improvement methods (Vilkhu, et al., 2021; Tandon, et al., 2021; Madugula, et al., 2022).

Various studies recognized cell selectivity (avoidance of unwanted axon stimulations) during electrode stimulation as a possible way towards retinal prosthesis quality improvement and proposed different approaches for dealing with it (Grosberg, et al., 2017; Tong, et al., 2020; Vilkhu, et al., 2021; Tandon, et al., 2021). Thereby, in their research Tandon, et al. (2021) presented an algorithm for preventing inadvertent axon stimulation of far-away RGCs which, among two other indicators, exploits spiking probability and thus DR in order to stimulate only RGCs that lie on the electrode array.

Another recent study performed by Madugula, et al. (2022), suggests that measurement of stochastic cell behavior i.e. spontaneous cell activity could be used for obtaining cell responses to electrical stimulation and thus for partially or completely avoiding complicated electrical stimulus calibration, which at the end could improve quality of restored vision.

Through their research, mentioned studies mostly concentrated on exploitation of stochastic cell behavior in different ways, investigating thereby retinal prosthesis improvement methods. In this thesis, we want to focus directly on stochastic measures (mostly DR) and try to find and understand differences in those measures, which arise from stimulation of different cell sections.

3.5.1 Aims of this thesis

The main aim of this thesis is estimation of dynamic range in dependency on the stimulated part of the cell. Since the nerve cell consists of several sections which show differences in both geometrical and biophysical properties, we can expect that their reaction to the stimuli and thus estimated DR values also differ. To achieve this, DR values were measured for six electrode positions that are defined in a way to stimulate different cell sections. Thereby, three types of stimulation were used: extracellular monophasic (cathodic), extracellular biphasic (anodic-cathodic) and intracellular (anodic).

For the purpose of analyzing the main aim of this thesis, following points related to stochastic measures (DR and RS) were investigated and discussed:

- **RS vs. diameter.** Since linear relationship between $\log RS$ and $\log d$ was reported in both experimental (Verveen, 1962) and modeling (Rattay & Tanzer, 2022a; Rattay & Tanzer, 2022b) studies, the response of RS to diameter was checked with our model, too.
- **DR vs. maximal sodium conductances.** Bearing in mind that the noise component used in this thesis, on all of the maximal ion conductances, is only sodium dependent, relationship between DR and $\bar{g}_{Na}$ was analyzed.
- **DR vs. electrode position (standard parameters).** With standard parameters defined for this thesis, DR was estimated for six electrode positions, stimulating thereby different cell sections. At the same time, the three types of stimuli mentioned above and the electrode-cell distance were varied. Since it has been reported that RS and thus DR should be quite independent of pulse duration (Rubinstein, 1995; Rattay & Tanzer, 2022a), it remained constant through all simulations.
- **DR vs. electrode position (increased channel noise at soma segments).** A recent experimental study performed on retinal ganglion cells by Madugula, et al. (2022) suggest that higher DR values are observed at somatic than at axonal cell regions. Following that, for computational simulations Madugula, et al. set standard deviation of somatic segments to be four times larger than the one for axonal segments. Thereby, they used Gaussian distribution to add random voltage values to membrane voltage and thus imitate stochastic cell behavior. Contrary to that, stochastic cell behavior in this thesis is modeled by inserting noise current, which depends on corresponding membrane area and maximum sodium conductances, into each segment of the cell. In order to see how our model and thus DR values react to increased channel noise at soma segments, again three types of stimuli and the electrode-cell distance were varied for all six positions.
- **DR vs. electrode position (upper threshold).** The existence of the upper threshold has been investigated and demonstrated for retinal ganglion cells (Boinagrov, et al., 2012; Rattay, 2014; Meng, et al., 2018). Thereby, it was shown that there is a stimulus intensity value (below the cell damage threshold) above which no AP could be initiated. This value is called the upper threshold

and represents the first stimulus intensity value where the action potential is not observed anymore. They also showed that, when approaching the upper threshold, the spiking probability decreases with the shape of the negative sigmoid (together with the lower threshold it gives us characteristic U-shape). All DR investigations until this point were performed for the lower threshold (referred to as just threshold), but at the end DR values were analyzed a bit with the upper threshold using extracellular monophasic stimulation.

4 Methodology

In order to investigate the stochastic properties of retinal ganglion cells in this thesis, dynamic range simulations during microelectrode stimulation were performed. For this purpose, a computational RGC multi-compartment model (see section 2.1.3) was developed.

The description of model dynamics and mechanisms (active cell behavior) was done using Fohlmeister and Miller model (Fohlmeister & Miller, 1997a)[6]. Since Fohlmeister and Miller model is Hodgkin and Huxley based model and thus has deterministic nature, it was adapted in order to simulate stochastic cell behavior by inserting a channel noise component at each compartment. Thereby, Rattay´ s current noise approach was used (Rattay, 2000). The simplified cell morphology, as well as cell biophysical properties were created based on previous experimental (Fohlmeister & Miller, 1997a; Fohlmeister, et al., 2010) and modeling studies (Jeng, et al., 2011; Rattay, 2014; Fellner, 2017; Meng, et al., 2018). However, during simulations some of these morphology and biophysical properties were slightly adapted for the purpose of better understanding different phenomena in the stochastic behavior of retinal ganglion cells. All standard parameters set for this thesis and described through this section are listed one more time in Appendix for a better overview (Table 7). Unless otherwise noted, those standard parameters are used during simulations.

The cell model was primarily stimulated extracellularly by monopolar microelectrode (monophasic, as well as biphasic), but also intracellularly with the aim of comparing the results and obtaining new conclusions.

Implementation of active cell behavior was done in NEURON (version 8.1.0) (Hines, 1993), while Python (version 3.9.0) was used to manage the model and visualize part of the results.

[6] Model available at ModelDB: http://modeldb.science/showmodel?model=3673

All mentioned points and procedures are described in detail in the text that follows.

4.1 Cell morphology

Before explaining the modeled morphology of the cell in this thesis, it is important to understand the principles of its development in the NEURON. As described by Hines & Carnevale (1997), NEURON enables us to develop multi-compartment branched models using two concepts: section and segment. Thereby, the section represents an unbranched cable of continuous length. More sections can then be connected to each other for realizing a branched structure. Each section consists of segments (defined for each section separately), which actually represent the number of compartments. Thus, each segment is defined by its own geometry and electrical circuit (cable model) and connected to other segments by axial resistors. Unless otherwise defined, sections and thus segments in NEURON have cylindrical shape.

The retinal ganglion cell in this thesis is implemented as a multi-compartment variant of the simplified RGC model. The morphology of the model was based on already existing simplified versions of the RGC model that could be found in previous studies from Rattay (2014), Fellner (2017) and Meng, et al. (2018).

The cell consists of three main parts (soma, axon and dendrites) modeled with eight sections. Soma is modeled as one section and assumed to have spherical shape whose approximation is modeled with the help of truncated cones of different dimensions connected to each other. Axon is divided into four parts with different geometrical and biophysical properties and thus four sections: axon hillock (AH), sodium band (SB), thin segment (TS) and distal axon (DA). Thereby, axon hillock and distal axon are modeled as a cylindrical structure, while sodium band and thin segment are modeled as conical structures using again truncated cones for shape approximation. Dendritic tree consists of three sections: vertical dendrite (VD), horizontal dendrite left (HDL) and horizontal dendrite right (HDR). All three dendritic tree sections are modeled as cylindrical structures. Number of segments for each mentioned section is given in Table 1. The exact arrangement of sections, together with their geometric properties, is presented in Figure 20. Note that all sections are expanded in only two dimensions x and z. Soma is placed in the center of the coordinate system and is connected to the

axon at the eastern pole and to the dendritic tree at the southern pole (detailed description in the caption of Figure 20).

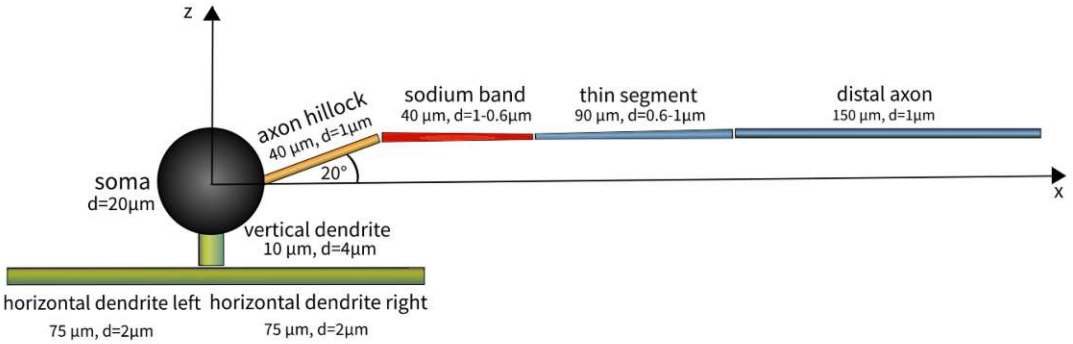

Figure 20: Morphology of the modeled RGC. Spherical soma is placed in the center of the coordinate system. Axon hillock is connected to soma at the eastern pole and with the inclination angle of 20° in the North-East direction ends at the beginning of the sodium band. From that point, sodium band, thin segment and distal axon are pointing to the east with no inclination angles. Vertical dendrite is leaving soma at the southern pole separating at the end to horizontal left and right dendrite pointing to east and west, respectively. Note that the schema is not exactly in scale and thus the exact length and diameter of each section are labeled.

The defined geometry properties of all sections are listed in Table 1. Diameters are based on values found in rat or cat retinal ganglion cells (Fohlmeister, et al., 2010), that were used for RGC models similar to this one in Meng, et al. (2018). Section lengths and number of segments are slightly modified from Rattay (2014) and Meng, et al. (2018) in terms of decreasing length or number of segments in some sections, mainly for the purpose of computational cost reduction.

Geometry	SOMA	AH	SB	TS	DA	VD	HDL	HDR
Diameter d $[\mu m]$	20	1	1-0.6	0.6-1	1	4	2	2
Length l $[\mu m]$		40	40	90	150	10	75	75
Inclination angle [°]		20						
Number of segments	21	41	41	21	51	5	21	21

Table 1: Geometric properties of the modeled RGC used in this thesis. AH: axon hillock, SB: sodium band, TS: thin segment, DA: distal axon, VD: vertical dendrite, HDL: horizontal dendrite left, HDR: horizontal dendrite right.

4.2 Cell biophysics

The model used to describe active cell behavior in this thesis is the Fohlmeister and Miller model that is defined based on experimental measurements performed on tiger

salamander retinal ganglion cells (Fohlmeister & Miller, 1997a) (for more details see section 2.3). Thereby defined maximal ion conductivities are listed in Table 2, since they are used as a reference for calculation of ion conductivity values for this model.

Biophysics (original)	$\bar{g}_{Na}$	$\bar{g}_{K}$	$\bar{g}_{L}$	$\bar{g}_{K,A}$	$\bar{g}_{Ca}$	$\bar{g}_{K,Ca}$
Value in $[mS/cm^2]$	50	12	0.05	36	2.2	0.05

Table 2: Maximal ion conductivities as defined in Fohlmeister and Miller model given in $[mS/cm^2]$.

Maximal ion conductivities in this model are defined in a following way: For each section $\bar{g}_{Na}$ value was set according to the values from Jeng, et al. (2011), while all other ion conductivities were calculated in a way that original ratios to $\bar{g}_{Na}$ values listed in Table 2 (Fohlmeister & Miller, 1997a) stay preserved. Since the $\bar{g}_{Na}$ value for sodium band from Jeng, et al. (2011) is given only in range (from 350 to 2800 mS/cm^2), the $\bar{g}_{Na}$ value for sodium band in this model is set to 400 mS/cm^2, based on value chosen in similar models from Fellner (2017) and Meng, et al. (2018). All defined maximal ion conductivities are listed in Table 3.

Biophysics	SOMA	AH	SB	TS	DA	VD	HDL	HDR
$\bar{g}_{Na}$	80	70	400	100	70	25	25	25
$\bar{g}_{K}$	19.2	16.8	96	24	16.8	6	6	6
$\bar{g}_{L}$	0.08	0.07	0.4	0.1	0.07	0.025	0.025	0.025
$\bar{g}_{K,A}$	57.6	50.4	288	72	50.4	18	18	18
$\bar{g}_{Ca}$	3.52	3.08	17.6	4.4	3.08	1.1	1.1	1.1
$\bar{g}_{K,Ca}$	0.08	0.07	0.4	0.1	0.07	0.025	0.025	0.025

Table 3: Conductivities of the modeled RGC used in this thesis given in $[mS/cm^2]$. For each section $\bar{g}_{Na}$value was set, while all other conductivities are calculated in a such way, that the proportions of the original ion conductivity values from Table 2 are preserved. AH: axon hillock, SB: sodium band, TS: thin segment, DA: distal axon, VD: vertical dendrite, HDL: horizontal dendrite left, HDR: horizontal dendrite right.

Few parameters needed for complete description of active cell behavior are independent of sections and are thus set only once for the whole model. That includes the capacitance of the membrane $C_m = 1\,\mu F$ and Nernst potentials $E_{Na} = 35\,mV$, $E_K = -75\,mV$ and $E_L = -62.5\,mV$ (all values set according to original values estimated in Fohlmeister & Miller (1997a)). Additionally, intracellular and extracellular resistivity were set according to values taken in the model from Meng, et

al. (2018) to $\rho_i = 300\ \Omega cm$ and $\rho_e = 1000\ \Omega cm$. Since Fohlmeister and Miller model from 1997 does not include temperature dependency, all simulations must be performed on initially set temperature of $T = 22°C$. Although the newer model (Fohlmeister, et al., 2010) includes temperature dependency, the model from 1997 was used in this thesis because of its stability regarding spontaneous firing that is necessary for proper estimation of stochastic behavior of nerve cells.

All above-mentioned section independent parameters are listed one more time in Table 4 for better insight.

General parameters	C_m	E_{Na}	E_K	E_L	ρ_i	ρ_e	T
Value	$1\ \mu F$	$35\ mV$	$-75\ mV$	$-62.5\ mV$	$300\ \Omega cm$	$1000\ \Omega cm$	22°C

Table 4: Parameters independent of sections used in this thesis.

4.3 Cell stimulation

In this thesis cell simulations were performed using two types of stimulations: intracellular and extracellular stimulation. Further description follows in this section.

4.3.1 Intracellular stimulation

In order to stimulate the cell from inside, one of NEURON´s built in point processes called $IClamp$[7] is used. With $IClamp$, current stimulus is applied directly to the inside of the cell. Thereby, the exact section and segment (compartment) in which current stimulus should be injected are defined. In the case of intracellular stimulation using $IClamp$, anodic (positive) current stimulus will depolarize the cell. Since determination of stochastic cell behavior requires train of pulses to be sent in order to calculate spiking probabilities, to $IClamp$ related original .mod[8] file was modified with the purpose of creating the most optimal $IClamp$ for sending a train of pulses. Modified file is then used in this thesis for all intracellular stimulations.

[7]https://www.neuron.yale.edu/neuron/static/py_doc/modelspec/programmatic/mechanisms/mech.html?highlight=point%20process

[8] Original .mod file: https://github.com/neuronsimulator/nrn/blob/master/src/nrnoc/stim.mod

4.3.2 Extracellular stimulation

As the name suggests, extracellular stimulation is a type of stimulation where an electrode is placed outside of the cell. In this thesis we assume to have a monopolar point electrode (ground electrode is assumed to be far away from point electrode) that is moved along x and z axis in order to stimulate different parts of the modeled cell. Thereby, the modeled cell is stimulated with a square pulse or train of square pulses (both monophasic and biphasic).

A description of extracellular stimulation for such assumptions is given in the book from Rattay (1990). He explains that, since we assume to have a point electrode and an influence of ground electrode that can be neglected (it is far away), the extracellular potential V_e can be calculated based on the distance from the electrode and the stimulus current shape itself:

$$V_e = \frac{\rho_e I_{st}}{4\pi r}$$

where, ρ_e describes extracellular resistance (see Table 4), I_{st} stimulus current intensity and r distance to the electrode that can be calculated using the Pythagorean theorem as $r = \sqrt{x^2 + z^2}$. This equation from Rattay is thus used in this thesis for calculating extracellular potential. Additionally, if we want to observe stimulation influence of the extracellular potential on a specific segment (compartment), following equation can be used if we assume that axon spreads along the x axis, which is a case in our model (Rattay, 1990):

$$\frac{V_{e,n-1} - 2V_{e,n} + V_{e,n+1}}{\Delta x^2}$$

Considering the morphology of the cell modeled in this thesis, some special points needed to be discussed and applied in order to calculate the influence of extracellular potential on the cell as accurately as possible. This especially applies to the modeling of the spherical soma and the calculation of the extracellular potential related to it. In following, these points are listed, briefly described and visualized in Figure 21 (see also Figure 28), while a detailed description (together with related figures) can be found in the work from Fellner (2017):

- **Contrary to the cylindrical compartments, which are modeled longitudinally by default, compartments of soma need to be modeled transversally**. Namely, a monopolar point electrode creates a spherical electric field whose strength reduces with the distance from the electrode. If we assume that the electrode is placed above the soma, we can conclude that the intensity of the electric field will be stronger on the pole of soma that is nearest to the extracellular electrode than on the opposite pole (if we apply cathodic stimulus, we expect the pole nearest to the electrode to be depolarized and the opposite pole to be hyperpolarized). Thus, in order to ensure correct distribution of electric field gradient along the spherical soma, its compartments are modeled transversally.
- **The transversal axis of soma needs to be orientated in the direction of the point electrode.** For the same reason as above (ensuring correct distribution of the electric field gradient along the soma compartments), spherical soma was modeled in a way, that direction of its transversal axis changes with the changed electrode position and thus always shows in the direction of the point electrode.
- **The vertical dendrite is always connected to the central segment of the soma, while the segment to which the axon hillock is connected changes with respect to the current orientation of the transversal axis of soma.** In order for interaxial currents between sections to be defined properly, the axon should be connected to the nearest segment of soma. Thus, based on the current position of the transverse axis of the soma, the segment closest to the axon hillock is calculated and then axon hillock is attached to it.
- **Coordinates of axon and dendritic tree need to be corrected.** When we connect two sections in NEURON, its coordinates do not preserve real geometric properties (dimensions). In Figure 21, orange arrows show where the beginning of the connected axon would be according to NEURON coordinates (without correction factor). For dendritic tree this correction factor corresponds to soma diameter (since it is connected to the central compartment of the soma), while for axon correction factor includes both soma diameter and

offset caused because of the adjustment to the different soma orientations (point above).

- **For the cylindrical sections, when calculating extracellular potential V_e, distance r is defined as an electrode-segment center distance, while distance r for calculating extracellular potential V_e at soma is defined as distance between electrode and segment surface center.** Electric field caused by the electrode affects segments of the cell at the surface and not at the segment center, but when calculating distance r for cylindrical sections due to their relatively small diameters and short segment lengths we can assume that electric field affects segment at the center and calculate distance r as an electrode-segment center distance. Contrary to that, modeled spherical soma has relatively large diameter (see Table 1) and thus electrode-segment center distance is always shorter than the distance between electrode and segment surface center where the electric field actually affects segments and we need to calculate distance r in that way.

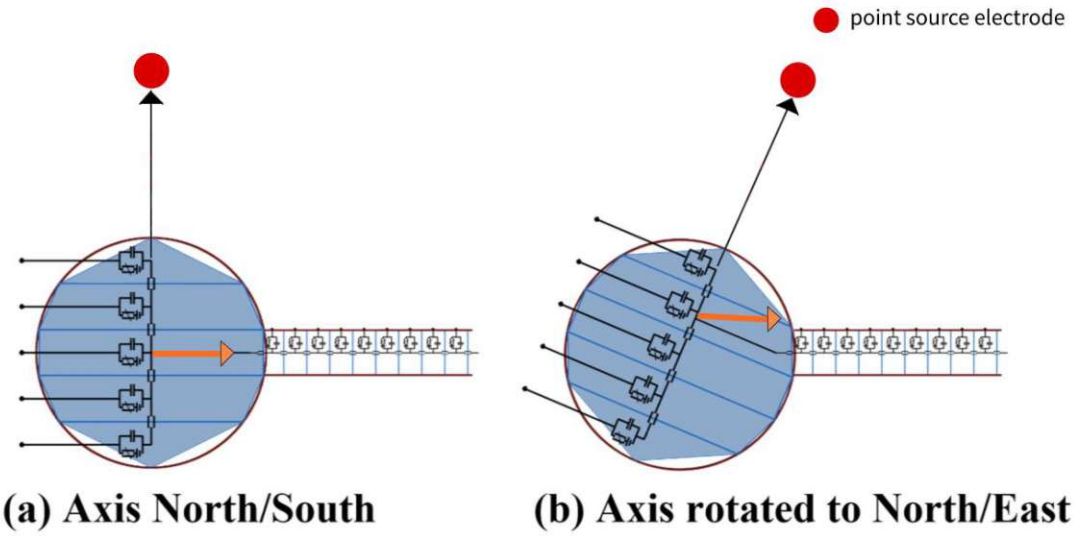

Figure 21: Special assumptions considered during modeling of spherical soma in this thesis. First important observation is related to transversal modeling of spherical soma compared to longitudinal modeling of axon which can be seen in both (a) and (b). Second observation is related to the orientation of the transversal axis of soma in the direction of the point electrode, whereby with moving electrode towards North/East, the transversal axis of soma is accordingly rotated. Third observation is related to the connection of the axon to the nearest soma segment. Thus, for the transversal axis oriented to the North/South (a) axon is connected to the central (third) soma segment, while for the transversal axis oriented to North/East (b) axon is connected to the current nearest (second) soma segment. Fourth important observation is related to the correction of the

NEURON coordinates. Thereby, orange arrows represent the beginning of the axon in NEURON coordinates and direction of its extension. Note that when the axon is connected to the central compartment and no rotation is observed (a), offset calculation includes only soma diameter, while for (b) we need to additionally include transversal axis rotation in order to calculate offset precisely. Figure adapted from Fellner (2017).

From the NEURON side, in order to perform and calculate extracellular stimulation two mechanisms are used: $extracellular$ and $xtra$ mechanism. Since $xtra$ mechanism provides a second coordinate system, it was also used for consideration of all above-mentioned offsets.

4.4 Validation of the model

In order to validate the model developed for this thesis and ensure that it can be reliably used for planned simulations, already existing models and to them related research were used. Since the model in this thesis shows the most similarities with the model from Meng, et al. (2018), the validation was mainly based on it. In the mentioned paper Meng, et al. investigated upper threshold phenomenon on retinal ganglion cell model by varying different parameters like type of pulse (monophasic and biphasic), pulse duration or electrode position.

For the purpose of model validation, few sets of mentioned parameters defined in Meng, et al. (2018) were applied to this model and threshold values and cell responses were compared. Thereby, it turned out that both threshold values and transmembrane voltage responses of this model show large similarity with Meng et al. model. The responses of both models to lower and upper threshold for the same electrode position (electrode position 1) and monophasic pulse are presented in Figure 22 (Meng et al. model) and Figure 23 (model developed in this thesis). Upper threshold is thereby defined as first stimulus intensity value where the action potential is not observed anymore. We can observe that transmembrane voltages of selected compartments as well as transmembrane voltage along the cell show very high degree of similarity for both lower (left) and upper (right) threshold response. Any small differences are probably due to existing differences in the models. Additionally, this model was also validated based on a model from Fellner (2017) and the same degree of similarity in responses was observed. Based on the comparison results, we can conclude that this model should be reliable and can be used for further simulations.

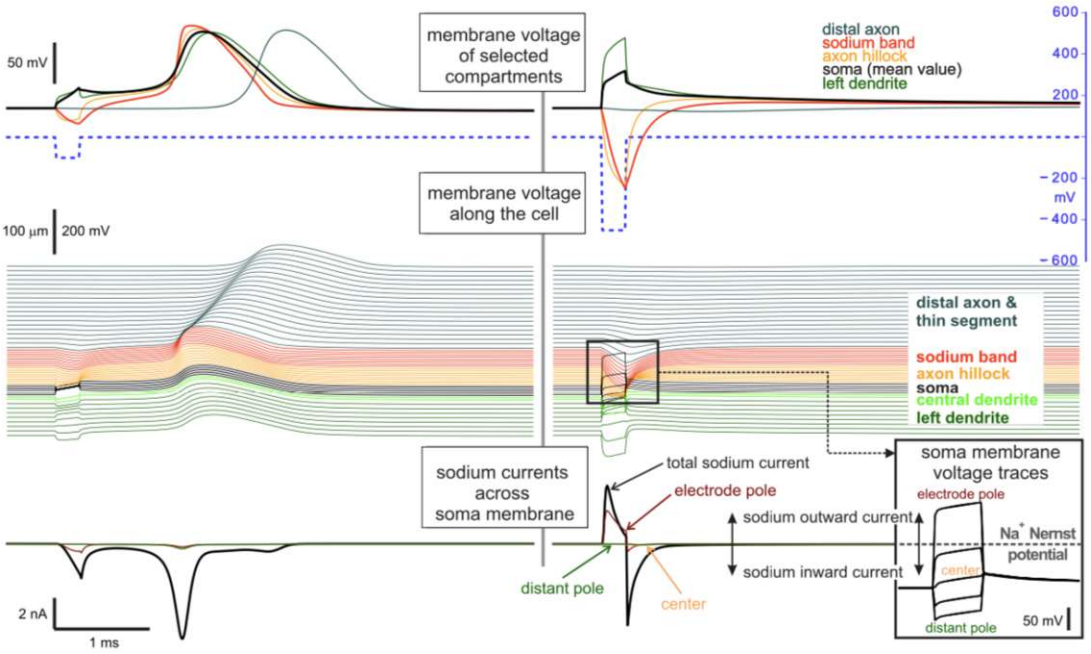

Figure 22: Meng et al. response of transmembrane voltages to lower and upper threshold for the electrode position 1 and monophasic pulse. This figure shows a Meng et al. model response to the estimated lower (top and middle left) and upper (top and middle right) threshold for electrode position 1 ($x = -35\ \mu m,\ z = 15\ \mu m$). Additionally sodium currents across soma membrane are presented (bottom right and left). Figure and parts of caption from Meng, et al. (2018).

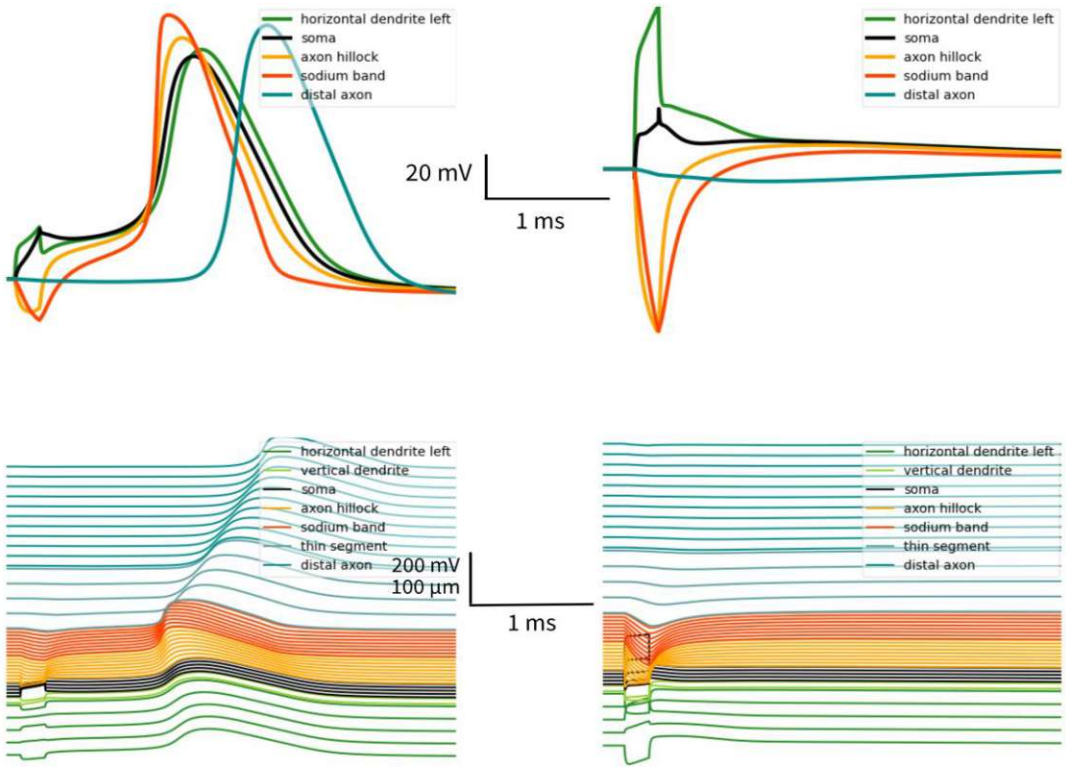

Figure 23: Response of the model developed in this thesis to the lower and upper threshold for electrode position 1 ($x = -35\ \mu m,\ z = 15\ \mu m$) and monophasic pulse. The responses of transmembrane voltage of selected compartments (top) as well as transmembrane voltage along

the cell (bottom) should be compared with the mentioned responses from Figure 22 for both lower (left) and upper (right) thresholds. If we compare them, a very high degree of similarity is observed in all selected compartments and along the cell. For lower threshold action potential is initiated at sodium band ant from there spreads to the other parts of the cell. For upper threshold horizontal dendrite left together with soma show depolarization in their central compartments, axon hillock and sodium band are thereby highly hyperpolarized, while distal axon shows almost no response besides slight hyperpolarization.

REMARK: For the purpose of easier comparison, similar colors as in Meng, et al. (2018) were chosen to mark different sections. In order to maintain consistency in the work, the same section colors will be used for visualization until the end of the thesis.

4.5 Noise modeling

As already described (see section 3), in order to simulate and investigate dynamic range and other stochastic measures, we need to add a stochastic component (channel noise insertion) to the model. The noise insertion method used in this thesis is so-called Rattay´ s current noise approach (see section 3.3.1), characterized with the following equation (Rattay, 2000):

$$I_{noise,n} = GAUSS\, k_{noise} \sqrt{A_n g_{Na}}$$

whereby, the mean and the standard deviation of $GAUSS$ (Gaussian noise current) were set to $\mu = 0$ and $\sigma = 1$, according to the original paper. Time step is set to its standard value of $dt_{noise} = 0.0025\ ms$. Value of constant factor common to all compartments is set to $k_{noise} = 0.0038\ \mu A/\sqrt{mS}$. This value comes from Rattay & Tanzer (2022b), where they estimated $k_{noise} = 0.0038\ \mu A/\sqrt{mS}$ value for non-myelinated axons using Hodgkin and Huxley model from 1952. In the absence of specific values for the retinal ganglion cell model used in this thesis, this value was chosen considering that this model is a non-myelinated model and as described in section 2.3 is based on the Hodgkin and Huxley model. Unless otherwise noted, sodium conductivity values are standard values listed in Table 3 and Appendix. The noise specific parameters are listed one more time in Table 5.

Noise parameters	μ	σ	dt_{noise}	k_{noise}
Value	0	1	$0.0025\ ms$	$0.0038\ \mu A/\sqrt{mS}$

Table 5: Noise specific parameters used in this thesis.

Above specified noise current $I_{noise,n}$ was inserted into each segment (compartment) of the modeled cell with the help of already mentioned NEURON specified IClamp point process. Just like in case of the intracellular stimulation, to IClamp related .mod file was modified in order to create the most optimal IClamp for sending a train of pulses that are used for the simulations performed in this thesis (see section 4.3.1).

The differences in generation of action potentials before and after inserting above-described noise current can be seen in Figure 24. After adding a stochastic component, the modeled cell can better imitate generation of AP from experimental results like the one from rat retinal ganglion cells presented in Figure 15 from Boinagrov, et al. (2012). We observe change in spiking probability related to stimulus intensity and thus investigate stochastic behavior of the cell.

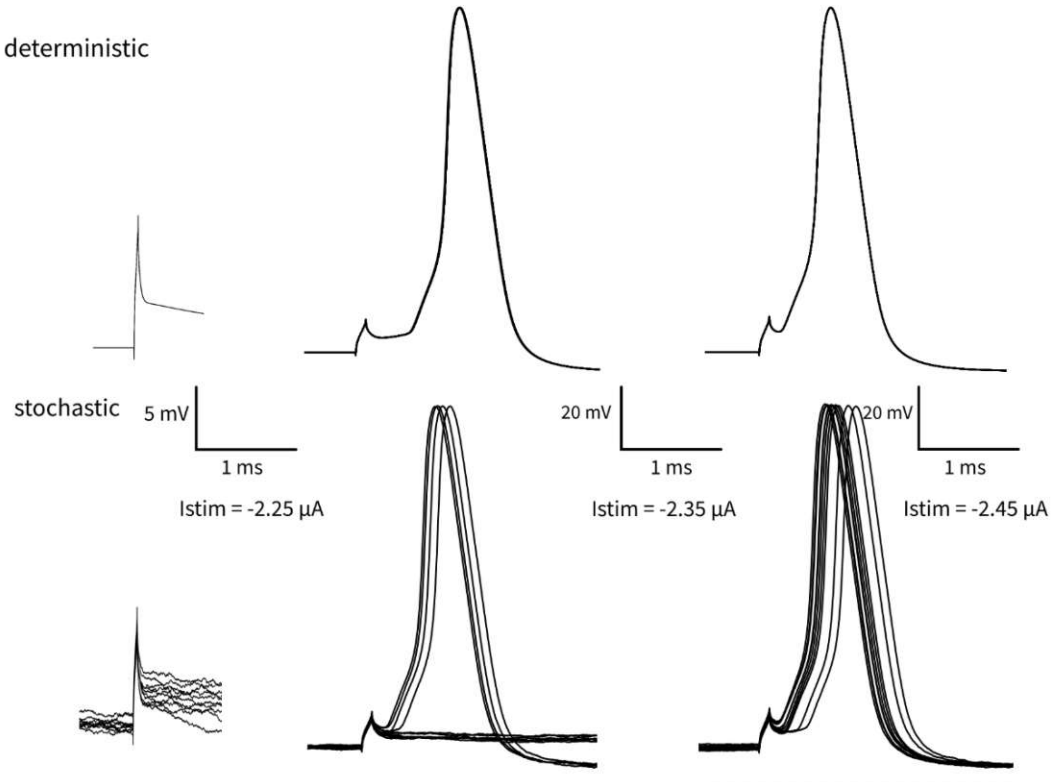

Figure 24: Generation of AP before and after inserting noise into the model. Figure shows action potential generation of the modeled cell with and without adding a stochastic component after sending a train of 10 pulses. The electrode was placed above the axon hillock, while APs were measured at soma. Applying subthreshold stimulus to a deterministic model results in no AP generation (top left), while applying threshold (top middle) or suprathreshold (top right) stimulus results in generation of all 10 APs. Additionally, all APs show the same shape and overlap. Applying subthreshold stimulus to stochastic model (bottom left) results in no AP generation, with applied threshold stimulus about 50% APs were generated (bottom middle), while applying suprathreshold stimulus results in generation of all 10 APs (bottom right). Contrary to

deterministic response on stimulus, APs generated using stochastic model show variations in shape and do not overlap.

4.6 Dynamic range determination

As already mentioned in section 3.2, dynamic range is an important measure of stochasticity of nerve cells (besides relative spread) and is defined as the stimulus intensity range in which spiking probability increases from 0.1 to 0.9 (Shepherd & Javel, 1997). Typical relationship between spiking probability and stimulus intensity (see section 3.1 and 3.2) in Figure 25 is characterized through both dynamic range and relative spread. This figure will be used for description of the dynamic range determination method used in this thesis.

Important thing related to determination of stochastic measures and thus dynamic range is that we need to work with a train of stimulus current pulses since we need to calculate spiking probability (the percentage of the evoked action potentials in relation to the number of sent pulses). Usual way of dynamic range determination would be the following: we are sending a train of pulses defined number of times and for each of those times we are using different stimulus intensity (around threshold value) and thereby calculating spiking probability. The number of various stimulus intensities for which we are sending a train of pulses and calculating spiking probabilities must be large enough so that spiking probabilities at the end can be fitted with the integrated Gaussian curve. From the integrated Gaussian curve, we can then derive stochastic measures like dynamic range or relative spread. This method can be observed with the help of Figure 25 from Rattay & Tanzer (2022b), where the stimulus intensity was increased by 50 μA for each step and resulting spiking probabilities (represented by black crosses) were then fitted with an integrated Gaussian curve (black line).

In this thesis we decided to try a slightly different approach for dynamic range determination and to calculate dynamic range from only “two points”. In order to explain the approach, we need to look at Figure 25 again, but this time we pay attention to the slope of the resulting spiking probability curve (see green line). Green line actually represents the inflection tangent at the threshold. We can see that in a range where spiking probability goes from 0.3 to 0.7, the inflection tangent is very close to

the fitted spiking probability function (black line). According to it, DR could be estimated from the data of only two points. To be more precise, we could only send a train of pulses two times and for that take two different values of stimulus intensity that are giving us a spiking probability in a range of 0.3 to 0.7. When spiking probabilities for these two stimulus intensity values are calculated, DR can be estimated using simple straight line equations. For RS estimation, the equation from Rattay and Tanzer that describes relationship between DR and RS (see section 3.2) was then used:

$$RS = \frac{\sigma}{\mu} \approx \frac{DR}{2.56\mu}$$

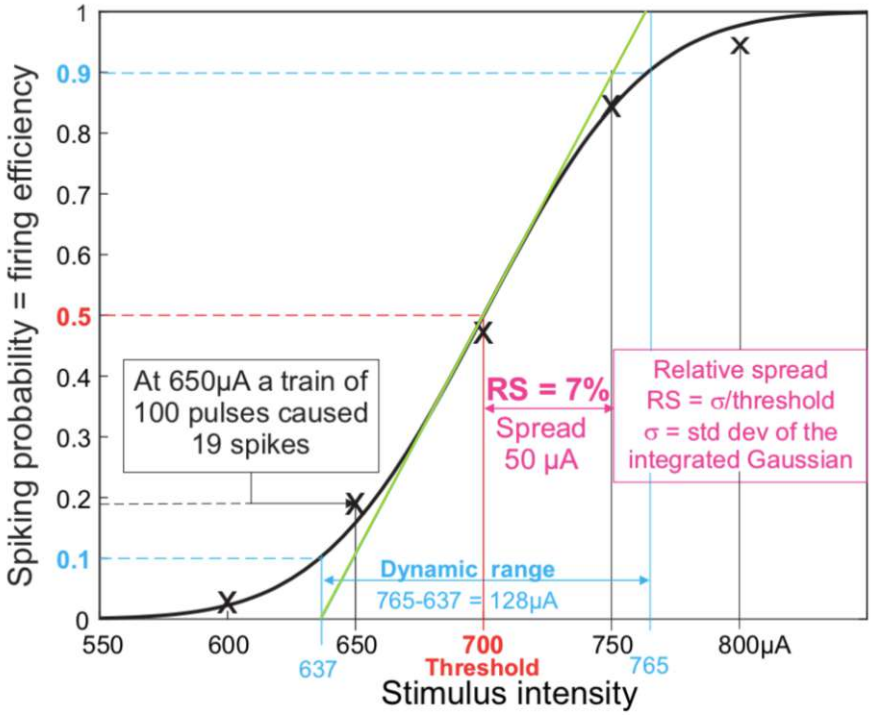

Figure 25: Determination of dynamic range. DR (cyan) and RS (magenta) in this figure were estimated from five spiking probability values fitted with an integrated Gaussian curve (black line). Threshold value, representing intensity related to 50% of spiking probability, is marked with the red color. Green line represents inflection tangent at the threshold and since it is actually leaning on the fitted spiking probability function (black line) in the range of spiking probability from 0.3 to 0.7, it can be used for estimating DR with only two data points. Figure adapted from Rattay & Tanzer (2022b).

To summarize, for each estimated dynamic range value in this thesis, two simulations were performed: once with a train of stimulus current pulses having the amplitude set slightly above a threshold value and once with a train of stimulus current pulses having

the amplitude set slightly below a threshold value. In order to estimate two needed stimulus intensity amplitudes, so that to them related spiking probabilities lie in desired range from 0.3 to 0.7 two steps were performed for each simulation:

- **Determination of the threshold stimulus intensity.** Threshold stimulus intensity for given simulation was determined manually with the noise turned off. Since the noise is not injected into compartments, there is no need for a train of pulses to be used, one stimulus current pulse is sufficient.
- **Quick assessment of the spiking probability sensitivity to the change of stimulus intensity.** Threshold stimulus intensity alone is not sufficient for determination of the two needed stimulus intensity amplitudes, because it only gives us information for which amplitude spiking probability is 50%, but not how sensitive is spiking probability function to the change of stimulus intensity amplitude. Therefore, in the second step a few pulses with the noise turned on were sent, so that sensitivity and thus two needed stimulus intensity amplitudes can be determined.

It is also important to note that, unless otherwise stated, DRs shown in the results are normalized to threshold and thus given as a percentage. Thereby, each threshold was first estimated manually (as already mentioned), but after calculating spiking probabilities it was also estimated from the "two points" method. Since there seems to be almost no difference between manually estimated and from the "two points" method calculated threshold, the last one was used for normalizing DR and is given in the results.

Regardless of the current electrode position, action potentials were always measured at soma (at the middle soma segment, to be more precise).

4.7 General procedure of simulations

In this section some general steps that were applied to each stimulation will be described.

In order to achieve needed accuracy in spiking probability and thus dynamic range determination, for each simulation train of 10 000 stimulus current pulses was used.

Sending a train of 10 000 pulses in one simulation alone requires relatively high computational costs. In our case we have an additional current noise component that needs to be injected in every single segment of the model, which makes these costs even higher. Thus, we tried to lower the simulation requirements by using different temporal discretization for different stimulation phases. According to the set time step dt, each simulation was divided into three phases (Table 6):

- **Initial phase.** Every simulation started with the so-called initial phase. During that phase, the simulation runs without any stimulus (noise is also turned off) to ensure that the model has reached a stable state and thus avoid possible oscillations and uncertainties. Initial phase duration is set to $dur_{init} = 500\ ms$ with the time step $dt_{init} = 10\ ms$. Such a large time step is allowed since practically nothing happens in this phase (we are just waiting).
- **Fine phase.** The phase in which we need by far the greatest temporal discretization, as well as the current noise components to be inserted into the segments, is the moment when a pulse is sent and an action potential potentially initiated. Time step in this phase is set to $dt_{fine} = 0.0025\ ms$[9]. Since we are sending 10 000 pulses (with certain distance between them), fine phase begins short before sending each pulse ($dur_{fine,before} = 5\ ms$), so that the inserted noise component can achieve a stable transient response. Fine phase ends short after action potential is potentially initiated and thus last totally $dur_{fine,total} = 10\ ms$. Ensuring that this phase together with noise lasts enough is important since noise enables us to analyze spiking probability through influencing AP generation.
- **Wait phase.** As already mentioned, the 10 000 pulses were sent in intervals with defined distance between them, so after each sent pulse we had a "wait phase" until the next pulse is sent. After performed tests, no difference in estimated DR could be found whether the noise during wait phase was turned

[9] Note that noise time step needs to have the same value as the fine time step: $dt_{noise} = dt_{fine} = 0.0025\ ms$.

on or not. Thus, we decided to exclude noise insertion between the pulses and to set time step to $dt_{wait} = 1\ ms$. In order for the cell to get back into initial state after being depolarized, distance between pulses was set to $dur_{wait} = 150\ ms$.

Simulation phases	Initial phase	Fine phase	Wait phase
duration dur $[ms]$	500	10	150
time step dt $[ms]$	10	0.0025	1

Table 6: Duration and time step parameter for all three phases of simulation. Note that fine phase starts 5 ms before each pulse.

Above-described phases are presented in Figure 26 for better understanding.

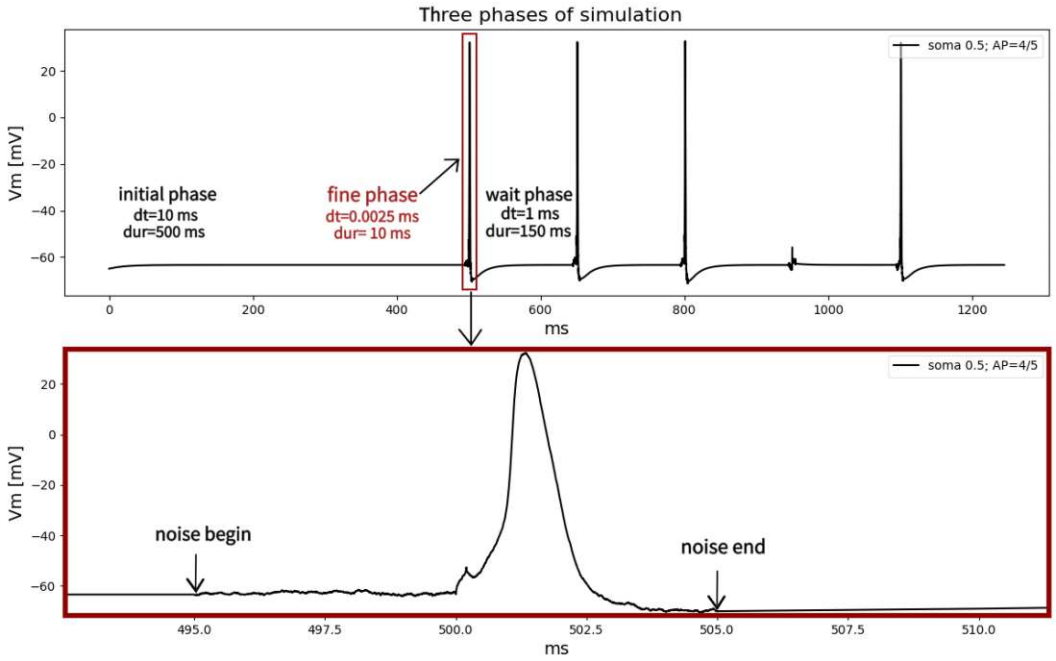

Figure 26: Three phases of each simulation divided according to their temporal discretization. In order to present these three phases, a train of 5 pulses was sent (cathodic extracellular stimulation) and transmembrane voltage V_m and thus reaction to the stimulus was measured at soma (soma 0.5 indicates that measurements were performed at the central soma segment). Simulation begins with an initial phase characterized with the large time step dt. Fine phase begins 5 ms before each pulse and last for totally 10 ms, so we can ensure that noise is present until the action potential is potentially initiated. Thereby, the finest time step dt is required. Between two pulses so-called wait phase characterized with relatively large time step dt is defined, so that the cell has time to come back to its initial state after excitation. Note that noise is inserted into segments only during the fine phase. In this particular simulation from 5 sent pulses, we observe 4 initiated APs, which gives us a spiking probability of 80%.

Dividing each simulation into three parts with different degrees of temporal discretization and optimizing insertion of noise component (see section 4.3.1 and 4.5)

notably reduced computational costs of the performed simulations. It was unfortunately not reduced enough for us to be able to perform simulations on private computers. Thus, all simulations were performed on a 60-core server at the Technical University of Vienna.

5 Results

In this section the results obtained from performed simulations are presented. For complete understanding of procedures behind those simulations, please refer to the previous section (Methodology).

Unless otherwise noted, simulations were performed with defined standard parameters (summed up in Table 7) and lower threshold (referred as just threshold). Number of initiated APs was thereby always measured at the central segment of soma.

5.1 Types of stimulation and electrode positions

In order to get a good insight into the change of the dynamic range depending on the part of the cell we are stimulating, simulations were performed at six different positions using three types of stimuli.

5.1.1 Types of stimulation

As already mentioned (see section 4.3), a modeled cell in this thesis was stimulated with the two main types of stimulation: intracellular and extracellular. For intracellular stimulation anodic train of current pulses was used (since by the intracellular stimulation positive current depolarizes the cell). For extracellular stimulation two different trains of current pulses were defined: monophasic (cathodic) and biphasic (anodic-cathodic). The anodic-cathodic biphasic stimulus (and not cathodic-anodic) was chosen since it seems that fewer artifacts occur with that type of stimulation and thus action potential detection is less complicated (see also (Meng, et al., 2018)). For better understanding and visualization, all stimulation types are presented one more time in Figure 27.

It is important to note that duration of pulses was constant during all performed simulations and set to $dur_{pulse} = 0.2\,ms$ for intracellular and extracellular

monophasic stimulation and to $dur_{pulse,bi} = 0.4\,ms$ for extracellular biphasic stimulation (since it consists of two parts). The only parameter that was varied is stimulus current intensity (amplitude).

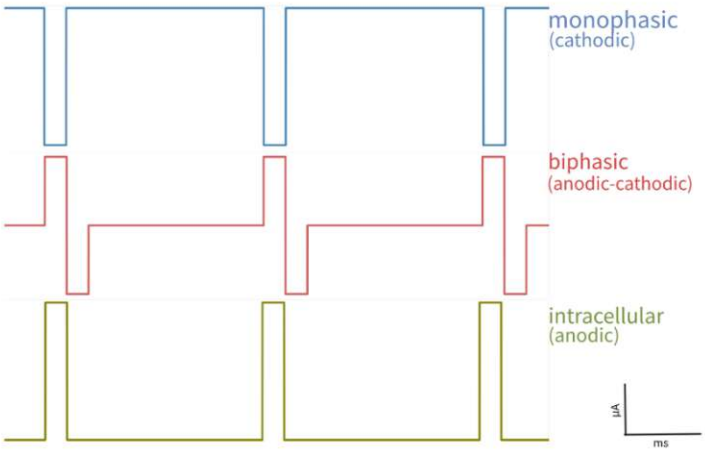

Figure 27: Three different trains of current pulses used for simulations in this thesis are presented. Using extracellular stimulation, monophasic cathodic (negative) and biphasic anodic-cathodic (positive-negative) trains of pulses were sent in order to excite the cell. Contrary to that, when using intracellular stimulation a train of anodic (positive) pulses were sent. Pulse duration was constant during all performed simulations, while stimulus current intensity (amplitude) was varied.

5.1.2 Electrode positions during simulations

Simulations in this thesis were performed using six different electrode positions, so we can cover stimulation of different cell parts which due to their geometric and biophysical properties could give us interesting results during DR estimation. For each electrode position chosen for extracellular stimulation (red circles in Figure 28), there was an equivalent position for intracellular stimulation (gray circles in Figure 28). Thereby, for one position an electrode was set directly above soma (SOMA), so we can observe electrode influence on it. Given that there are different geometric and biophysical properties along the axon, the electrode was set above its three different sections: axon hillock (AH), sodium band (SB) and distal axon (DA). The remaining two electrode positions were used for dendritic tree stimulation. Thereby, the electrode was set at two different positions along left horizontal dendrite: in the center (HD1) and at the boundary with the vertical dendrite (HD2).

Those positions and their abbreviations, together with the distribution of the extracellular potential Ve for each position are presented in Figure 28. Color gradient along the cell shows us the influence of the extracellular potential Ve, that arises from sent extracellular current stimulus, on each segment of the modeled cell. We observe how the distribution of Ve changes when electrode position is changed. As expected, with increased electrode-segment distance, influence of Ve on segments decreases. Additionally, the electric field gradient along the transversal axis of soma is well visible, especially for electrode positions that are closer to soma (see section 4.3.2).

Due to the morphology of the modeled cell, where sections are mostly changing along the x axis, electrode positions for extracellular stimulations are characterized through their position on the x axis and thus electrode positions in respect to x remained constant for each section during all simulations: $x = -37.5\ \mu m$ for HD1, $x = 0\ \mu m$ for HD2 and SOMA, $x = 20\ \mu m$ for AH, $x = 67.58\ \mu m$ for SB and $x = 252.58\ \mu m$ for DA. Contrary to that, electrode positions can be moved along the z axis, without changing a predicted site of excitation. That was used to investigate DR in dependence of electrode-cell distance. Thereby, simulations were performed at two electrode-cell distances:

- **dist1**: Since we tried to keep the electrode-cell distance same for all stimulated sections, dist1 is defined as distance where electrode is $26\ \mu m$ away from each stimulated section. Thus, the z value for each electrode position was set in a way, that the electrode-cell distance remains $26\ \mu m$.
- **dist2:** With second distance dist2, we wanted to increase electrode distance for each section for $10\ \mu m$ which results in electrode-cell distance of $36\ \mu m$.

Note that specified x values for electrode positions were chosen in a way to be closest to the center of section and thus stimulate corresponding central segments the most (only exception is position HD2). Parallel to that, intracellular anodic stimulus current was always injected into the central segment of corresponding section, with the exception of the position HD2 where it is injected into the first segment of left horizontal dendrite.

It is important to note one more time that regardless of electrode position or type of stimulation, APs were always measured at soma.

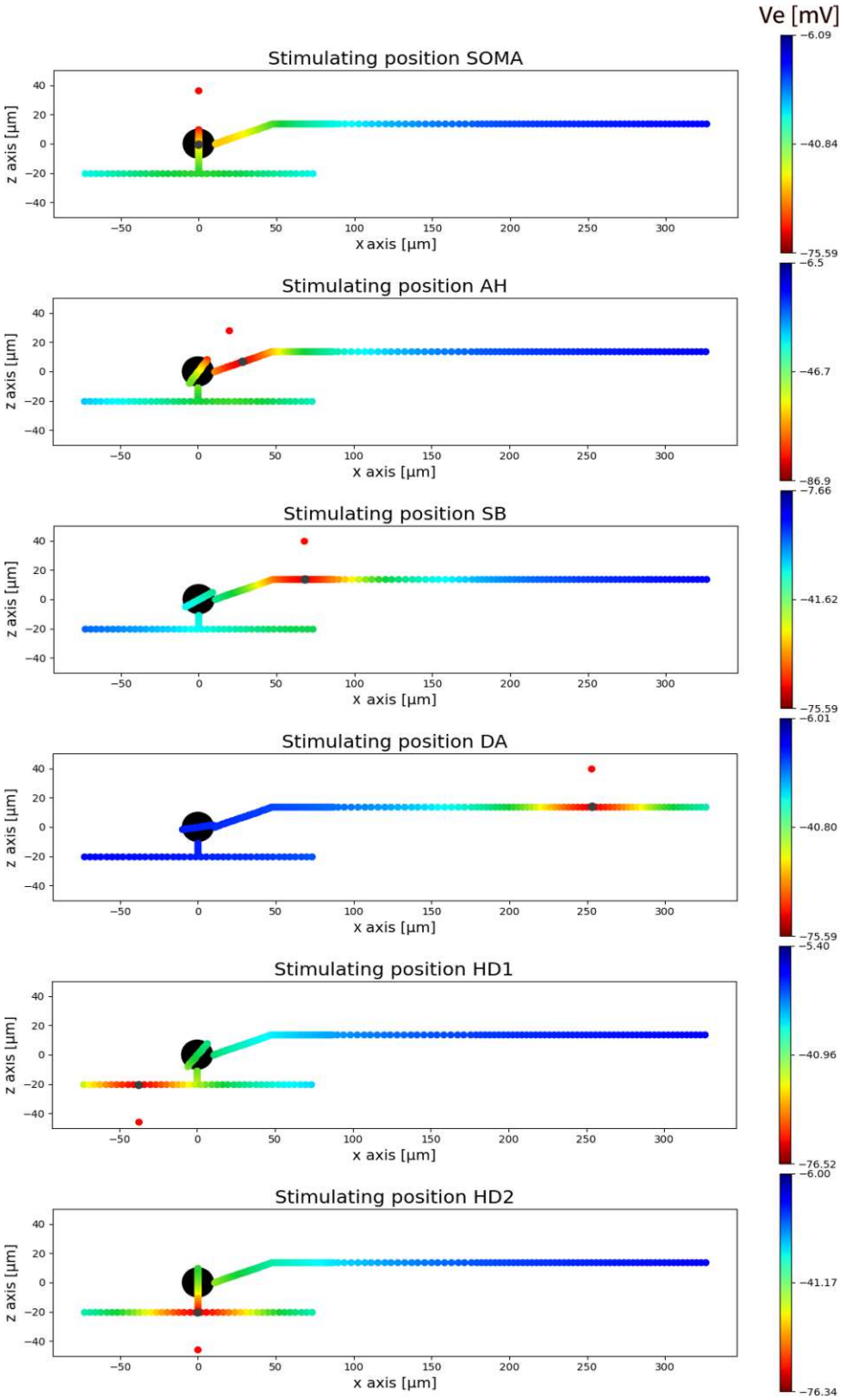

Figure 28: Six different electrode positions used for simulations in this thesis. Red circles represent extracellular electrode position, while gray circles represent corresponding segments

where stimulus current was inserted when using intracellular stimulation. For DR investigation near the soma, electrode was placed directly above it (SOMA). Along axon three different electrode positions were changed and investigated: axon hillock (AH), sodium band (SB) and distal axon (DA). The remaining two electrode positions were used to investigate DR around the dendritic tree, whereby the electrode is first placed below the center of the left horizontal dendrite (HD1) and then moved and placed at the boundary with the vertical dendrite (HD2). During simulations electrode position was moved along z axis (see explanation of dist1 and dist2), but remained constant in respect to the x axis for each section. The color gradient represents influence of the extracellular potential V_e during extracellular stimulation (cathodic stimulus of amplitude $I_{st} = 2.5\ \mu A$) on the segments in dependency of the current electrode position. Thereby, we observe highest influence of V_e on the segments that are nearest to the electrode, which is expected since the V_e is defined as a function of stimulus and electrode-segment distance (see section 4.3.2). Note that each circle in color gradient represents one segment (these circles are only recognizable in the sections with the smallest number of segments in relation to their length like thin axon or horizontal dendrites).

5.2 Single parameters variation

In order to validate our model and better understand the results from following simulations, a relationship between stochastic measures (relative spread and dynamic range) and two single parameters were inspected. The first one is diameter d (for validation) and second one is maximal sodium conductance $\bar{g}_{Na}$ (for better understanding the results).

5.2.1 RS vs. diameter

As described in section 3.4, there is a linear relationship between $\log RS$ and $\log d$. In order to prove that our model shows the same behavior, a relationship between RS and diameter was estimated with all three types of stimulation: extracellular monophasic, extracellular biphasic and intracellular. For extracellular stimulations electrode was set above distal axon (position DA) and diameter of distal axon was varied from its initial value $\mathrm{d} = 1\ \mu m$ to $\mathrm{d} = 3\ \mu m$ in steps of $0.5\ \mu m$. Accordingly, for intracellular stimulation stimulus current was inserted into central segment of DA, whereby the two last simulations ($\mathrm{d} = 2.5\ \mu m$ and $\mathrm{d} = 3\ \mu m$) are left out.

The results are presented in Figure 29. Regardless of type of stimulation, linear relationship between $\log RS$ and $\log d$ is observed, whereby with increased diameter, RS decreases. Apart from the fact that the relative spread seems to be greater for this electrode position (DA) when using intracellular simulation, slope for all three stimulation types appears to be similar.

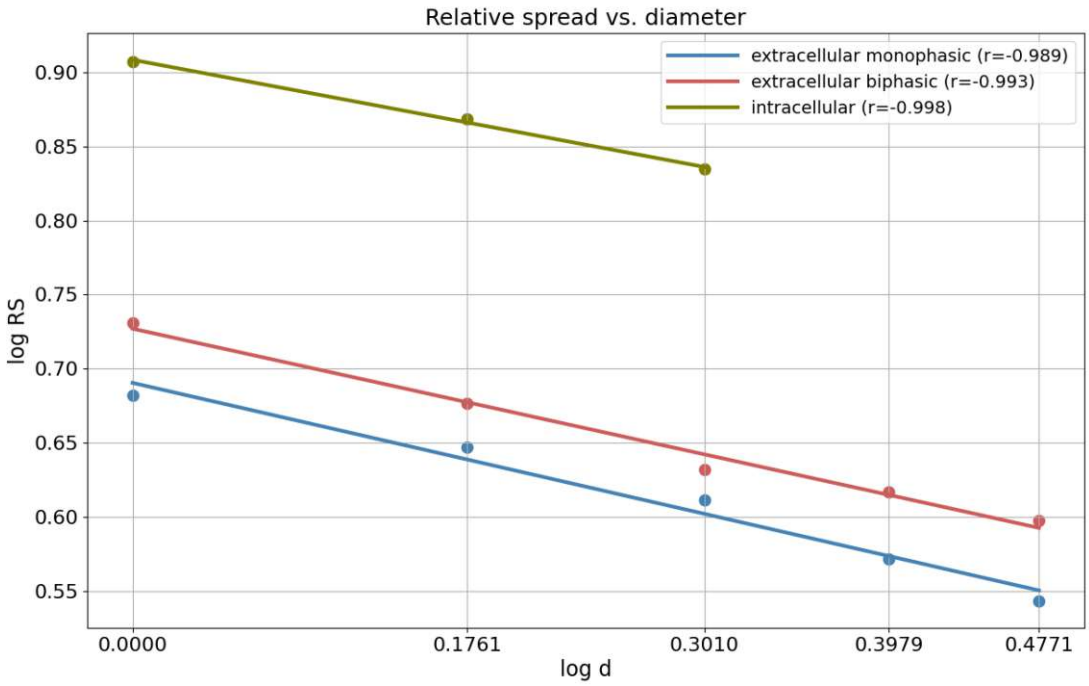

Figure 29: RS vs. diameter. Linear relationship between log RS and log d is observed for all three types of stimulation: extracellular monophasic (red), extracellular biphasic (blue) and intracellular (olive). Electrode was set directly above distal axon (position DA) for extracellular stimulations and inserted into the central segment of distal axon for intracellular stimulation. Diameter of distal axon was increased from its initial value of d $= 1\ \mu m$ in steps of $0.5\ \mu m$. Correlation coefficients r are given in the brackets and show a very high degree of correlation for each stimulation type.

5.2.2 DR vs. maximal sodium conductance

Since when it comes to ion conductances, inserted noise current $I_{noise,n}$ depends only on maximal sodium conductance $\bar{g}_{Na}$ in given section (see sections 3.3 and 4.5), we wanted to see what the relationship between DR and maximal sodium conductance $\bar{g}_{Na}$ is and thus better understand further results. For that, the electrode was set directly above the sodium band (position SB) for extracellular stimulations and stimulus current was accordingly inserted into the central segment of the sodium band for intracellular stimulation. Sodium band was chosen because it is a section with by far the highest maximal sodium conductance $\bar{g}_{Na}$. Thereby, maximal sodium conductance for sodium band was varied from its initial value $\bar{g}_{Na} = 400\ mS/cm^2$ to $\bar{g}_{Na} = 1200\ mS/cm^2$ in steps of $200\ mS/cm^2$.

The results for all three stimulation types are presented in Figure 30. They all show linear relationship between DR and maximal sodium conductance $\bar{g}_{Na}$ whereby for

increased $\bar{g}_{Na}$ DR also increases. The highest slope is observed when using extracellular monophasic stimulation (red), while slopes of fitted lines for intracellular (olive) and extracellular biphasic stimulation (blue) seem to be very similar.

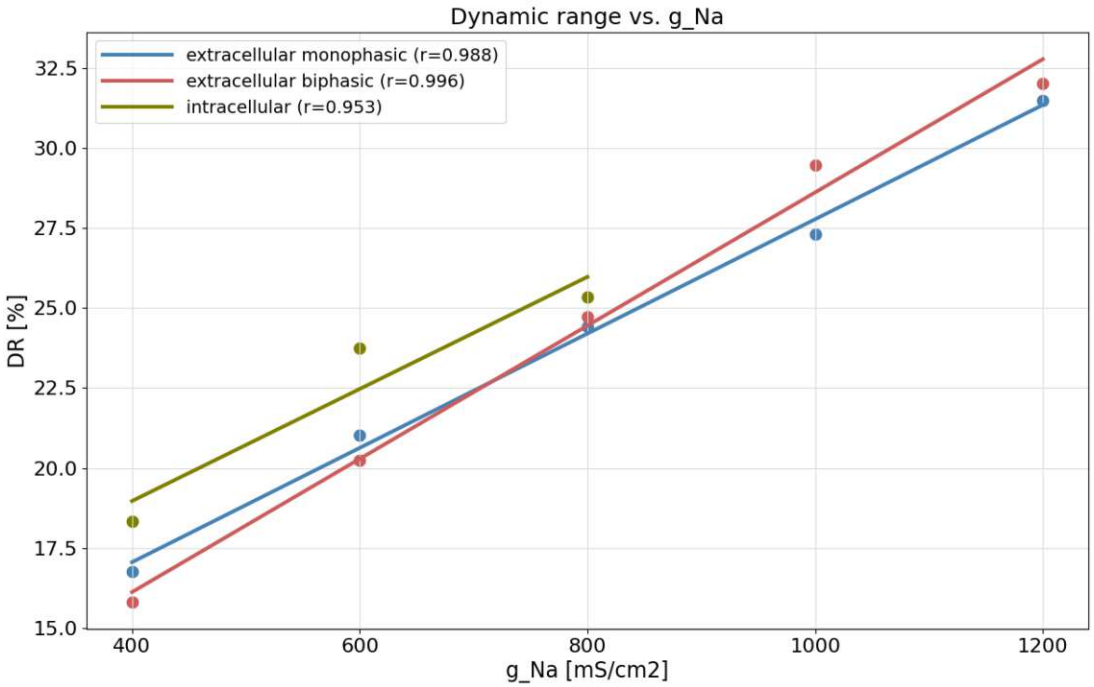

Figure 30: DR vs. maximal sodium conductance. Linear relationship between DR and $\bar{g}_{Na}$ is observed for all three types of stimulation: extracellular monophasic (red), extracellular biphasic (blue) and intracellular (olive). Electrode was set directly above the sodium band (position SB) for extracellular stimulations and inserted into the central segment of the sodium band for intracellular stimulation. Maximal sodium conductance of sodium band was increased from its initial value of $\bar{g}_{Na} = 400\ mS/cm^2$ in steps of $200\ mS/cm^2$. Correlation coefficients r are given in the brackets and show a very high degree of correlation for each stimulation type.

5.3 Site of AP initiation

Like described and defined in section 5.1.2, six electrode positions were used during performed simulations. Although the electrodes were set in a way to stimulate different cell sections, the place of excitation often does not coincide with the site of the action potential initiation. For a proper analysis of estimated DRs, information about the site of AP initiation in relation to the section being stimulated could be very important. This phenomenon was thus investigated for the modeled cell. Thereby, all used stimulus intensity values were set according to those used for DR estimation (slightly above lower threshold values).

Apart from electrode position DA, where site of AP initiation is distal axon and thus coincide with the site of excitation, for all other electrode positions (HD1, HD2, SOMA, AH and SB) site of AP initiation was sodium band. Thereby, there was no distinction between extracellular (monophasic and biphasic) and intracellular stimulations. After being initiated at sodium band, AP propagates in both directions in order to reach other sections, while when being initiated at distal axon, AP propagates in one direction in order to reach other sections. For better visualization, in following diagrams site of AP initiation is shown for three electrode positions that are placed the furthest from sodium band (SOMA, HD2 and DA) for extracellular monophasic (Figures 31-33) and intracellular stimulations (Figure 34). The reason for not presenting results observed for extracellular biphasic stimulation is because no differences in site of AP initiation could be observed when compared to extracellular monophasic stimulation.

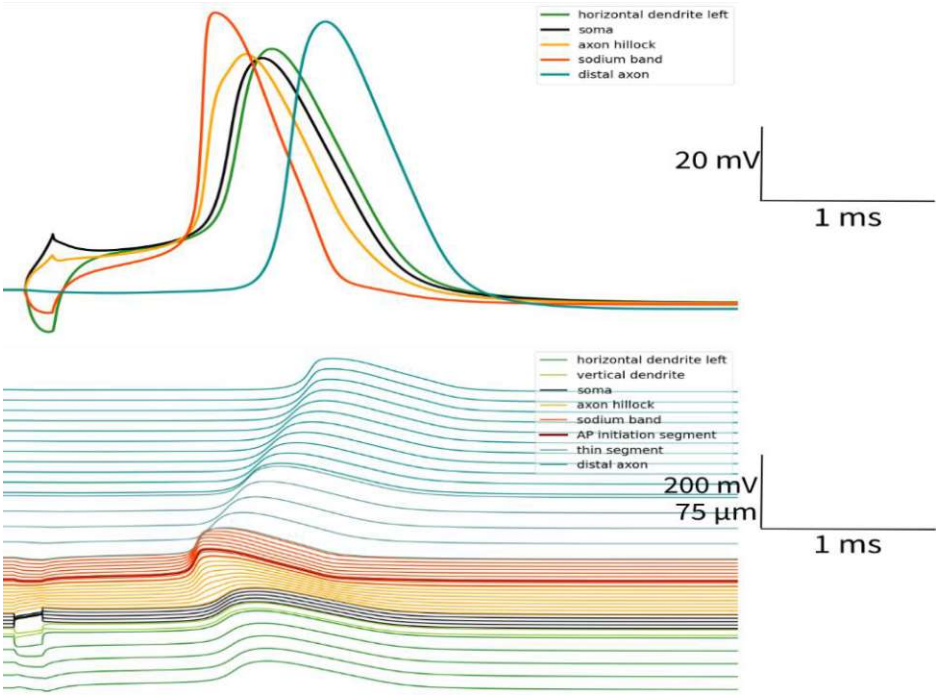

Figure 31: AP initiation for electrode position SOMA in response to extracellular monophasic cathodic stimulation. The responses of transmembrane voltage of central segments of selected sections (top) as well as transmembrane voltage along the cell (bottom) are shown. Site of AP initiation (in this case sodium band, although the electrode was placed above soma) is marked with the thick red line (bottom). As presented in both subfigures, after being initiated at sodium band, AP propagates in both directions through other sections, whereby the last segments where the action potential arrives are those in the distal axon.

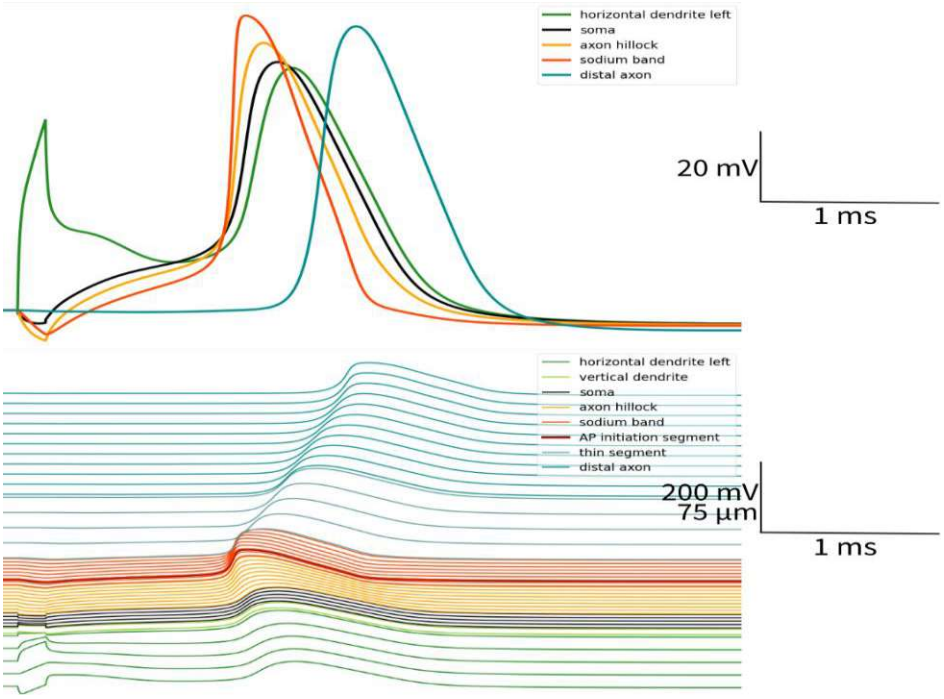

Figure 32: AP initiation for electrode position HD2 in response to extracellular monophasic cathodic stimulation. Site of AP initiation is sodium band, although electrode was placed below left horizontal dendrite. Very similar response as already seen for electrode position SOMA in Figure 31. Same layout as in Figure 31.

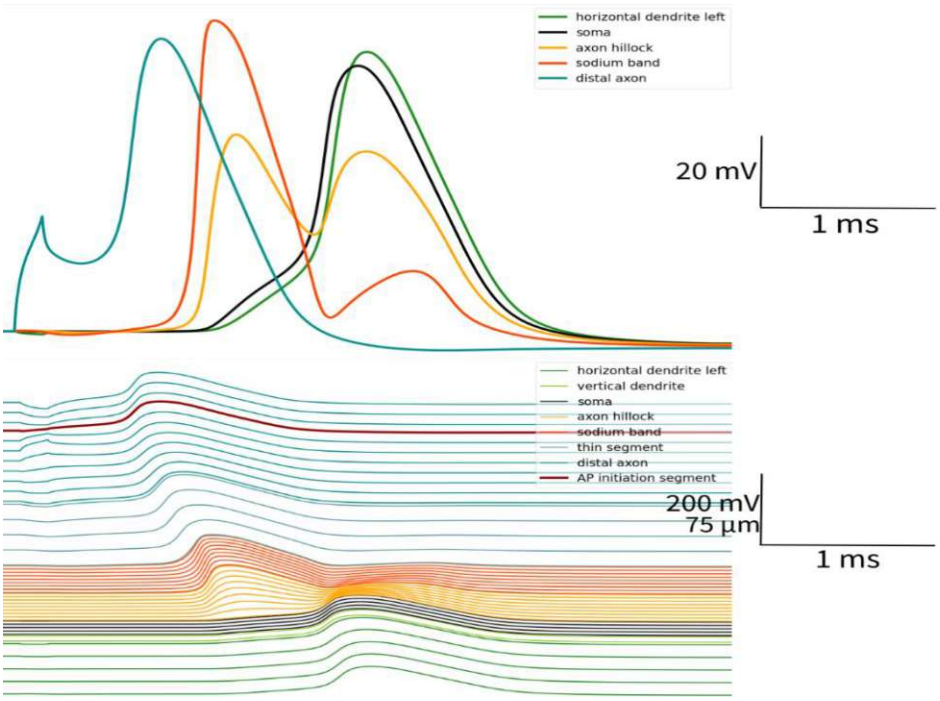

Figure 33: AP initiation for electrode position DA in response to extracellular monophasic cathodic stimulation. Site of AP initiation is the distal axon and thus overlaps with the stimulated section. From the distal axon, AP propagates further into all other sections in one direction until it reaches the end of horizontal dendrites. Same layout as in Figure 31.

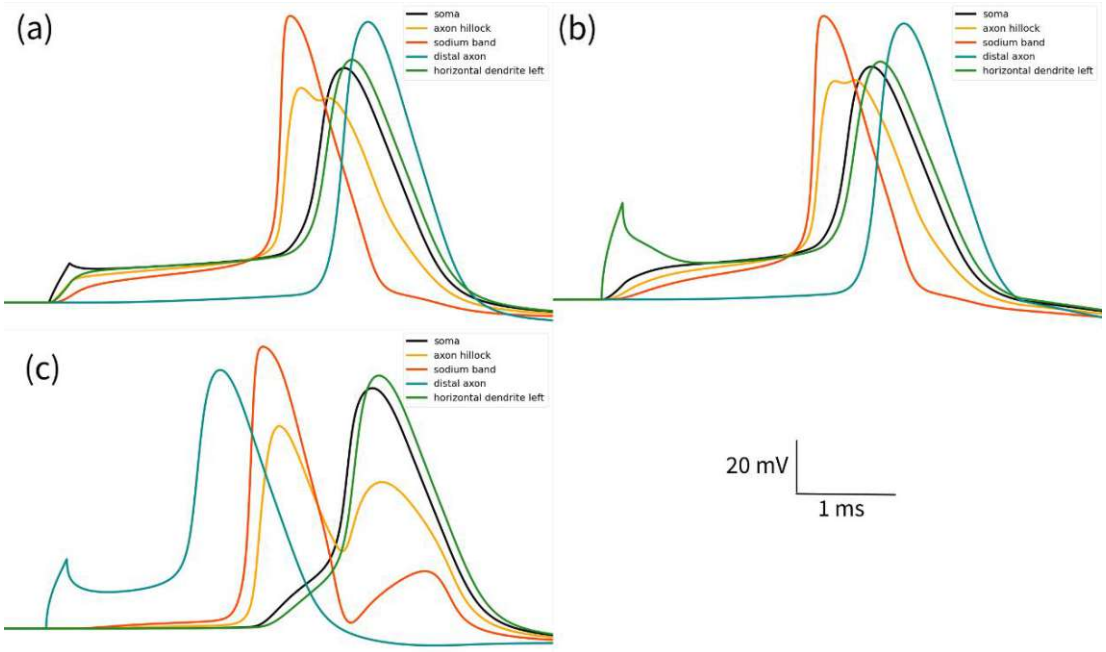

Figure 34: AP initiation for three electrode positions in response to intracellular anodic stimulation: position SOMA (a), position HD2 (b) and position DA (c). The responses of transmembrane voltage of central segments of selected sections are shown and are very similar to the extracellular monophasic cathodic responses presented in previous three Figures.

It is important to note that the site of AP initiation could change with increased stimulus intensity. Since at the end we decided to pay a bit attention to DR estimation for the upper threshold, sites of AP initiation with higher stimulus intensities (around upper threshold value) were checked, but in our case they remained the same even for high stimulus intensities.

5.4 DR vs. electrode position (stimulated section)

The results presented so far can be seen as an introduction that serves for a better understanding of the following results. In this section the main results related to the change of dynamic range in dependency of electrode position are presented for all three types of simulation: extracellular monophasic (cathodic), extracellular biphasic (anodic-cathodic) and intracellular (anodic).

For better visualization of the distances between defined electrode positions, the x axis in following figures is actually stretched out thick black line from Figure 35, which represents the path that starts from the left horizontal dendrite and through the vertical

dendrite and the soma reaches the distal axon. The distances between the stimulation points are proportional to the distances on the thick black line.

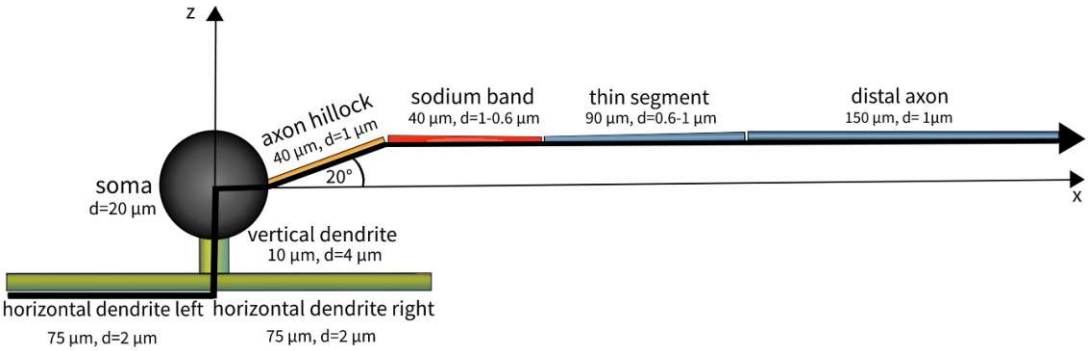

Figure 35: Path used for better visualization of electrode positions and distances between sections in related figures. This path is marked with thick black line and starts from the left horizontal dendrite and reaches the distal axon through vertical dendrite and soma. Thus, the *x* axis in the following figures is actually stretched out thick black line with preserved proportions.

5.4.1 DR determination with standard parameters

In this section results of DR dependency of electrode position are presented in the way that for each type of stimulation DR and threshold values for all six defined electrode positions are shown. Thereby, for both types of extracellular stimulations DR was estimated using two electrode-cell distances: dist1 and dist2 (see section 5.1.2), while for intracellular stimulation only one set of simulations were performed, since the stimulus is injected directly into a defined segment.

Figure 36 shows results obtained from extracellular monophasic cathodic train of pulses. We can see that by increasing the electrode-cell distance from dist1 to dist2, the threshold values increase, while the ratio of estimated thresholds between sections remains the same, which actually was to expect. Highest threshold values were needed to initiate AP for electrode position HD2, while for electrode position SB lowest threshold values were observed. Contrary to that, estimated DR values seem to be relatively independent of distances (the biggest difference so far is observed for electrode position HD2). By far the highest DR was observed for electrode position SB, while lowest DR values were estimated for electrode position HD1 and SOMA. What seems to be interesting is the sudden increase in threshold and DR values for electrode position HD2, compared to values of adjacent positions. Note also how,

although axon hillock and distal axon have same geometrical and biophysical properties (besides length), DR values between electrode positions AH and DA differ notably.

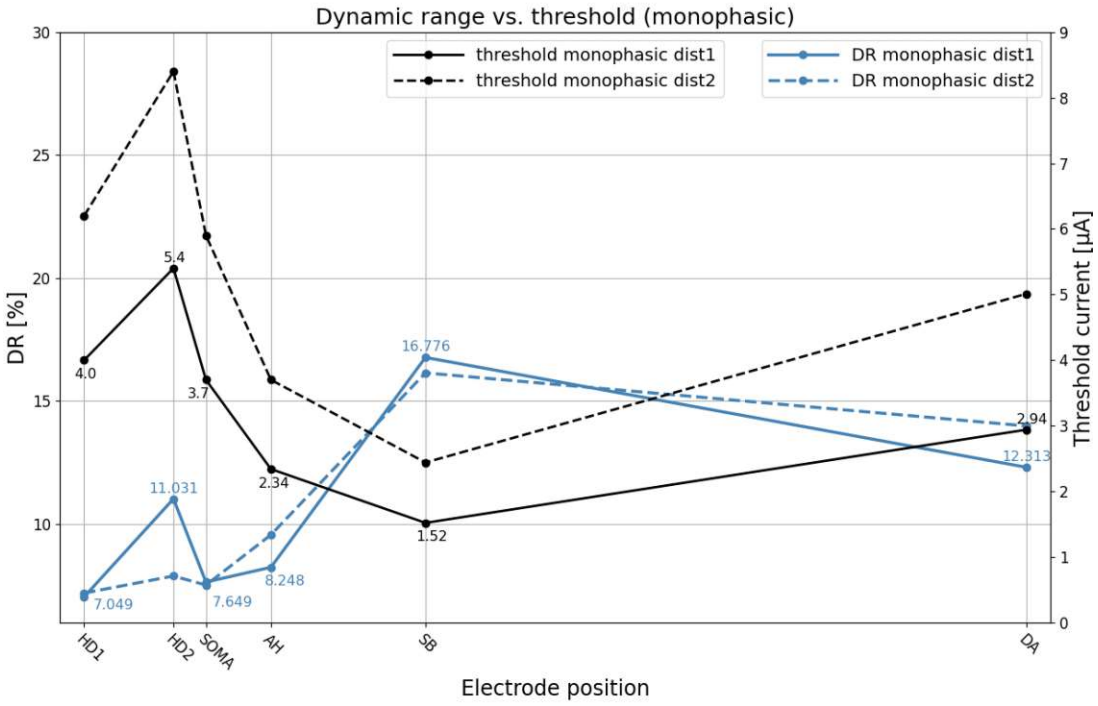

Figure 36: DR vs. electrode position (simulated section) obtained from extracellular monophasic cathodic train of pulses. Threshold (black) and DR (blue) values are shown for two different distances: dist1 (solid lines) and dist2 (dashed lines). Dist1 is defined as distance where electrode is placed 26 μm away from each stimulated section, while for dist2 electrode is set 10 μm further away from the cell, which results in electrode-cell distance of 36 μm.

The results obtained from extracellular biphasic anodic-cathodic train of pulses are shown in Figure 37. Just like by monophasic stimulation described above, threshold values increase with increased distance, but their course remains the same. Here as well, it appears that DR values show no distance dependence. Additionally, the highest and lowest values of both threshold and DR are the same as by monophasic stimulation. Besides electrode position HD2, which shows more similar threshold and DR values when compared to adjacent electrode positions (which is not the case by monophasic simulation) and the fact that threshold values here tend to be a bit higher than by monophasic stimulation, no other visible differences could be observed.

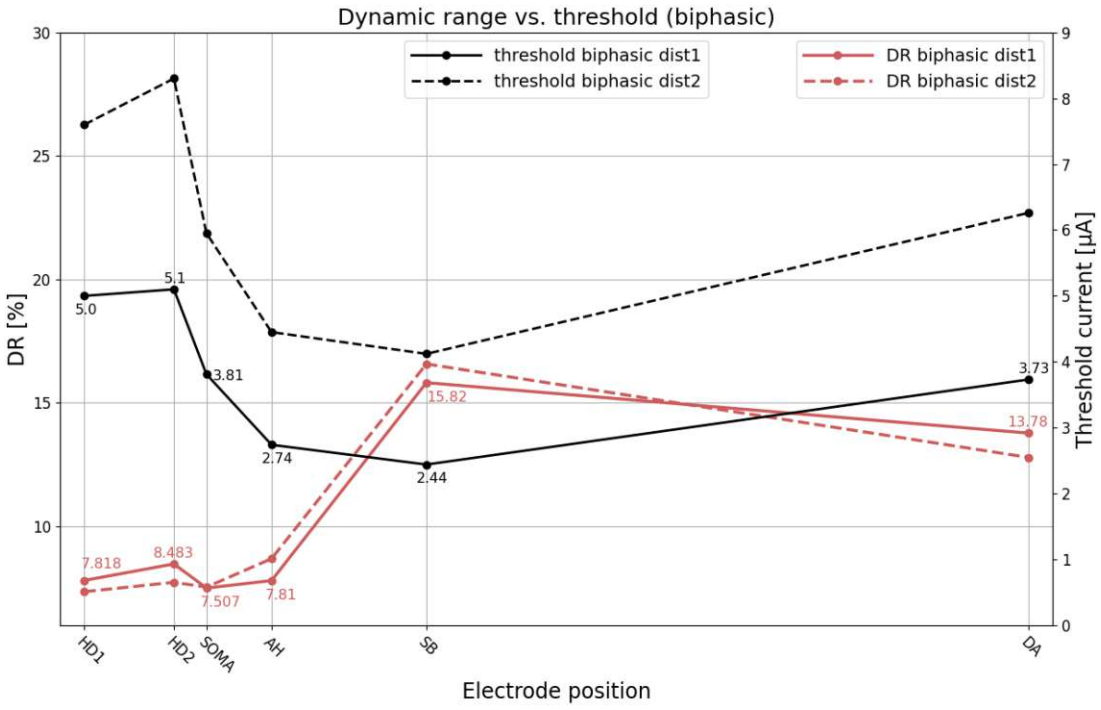

Figure 37: DR vs. electrode position (simulated section) obtained from extracellular biphasic anodic-cathodic train of pulses. Same layout as in Figure 36.

Figure 38 shows results obtained from an intracellular anodic train of pulses. When it comes to threshold, it shows significantly lower values for all electrode positions, when compared to extracellular stimulations. Thereby, highest (HD2) and lowest (SB) threshold value remained same as by extracellular stimulation, while difference is observed at electrode position SOMA (threshold almost as high as at position HD2) and at position DA (threshold almost as low as at position SB). Estimated DR values are not actually comparable to the one obtained from extracellular stimulations. Here, DR increases with each next electrode position and thus has the lowest value at electrode position HD1 and the highest for electrode position DA.

In order to get a better overview of DR values estimated from three different types of stimulation, we put them together and presented them in Figure 39. We observe that DRs estimated from extracellular monophasic and biphasic stimulation show no significant difference. Thereby, it seems that DR values for monophasic stimulation tend to be a bit higher (except at position DA and HD1), but the course remains very similar. Compared to extracellular stimulations, DR values obtained from intracellular stimulation tend to be higher and as mentioned above do not follow a similar pattern.

Note how DR values differ for electrode positions AH and DA, although both sections have the same diameter and biophysical properties.

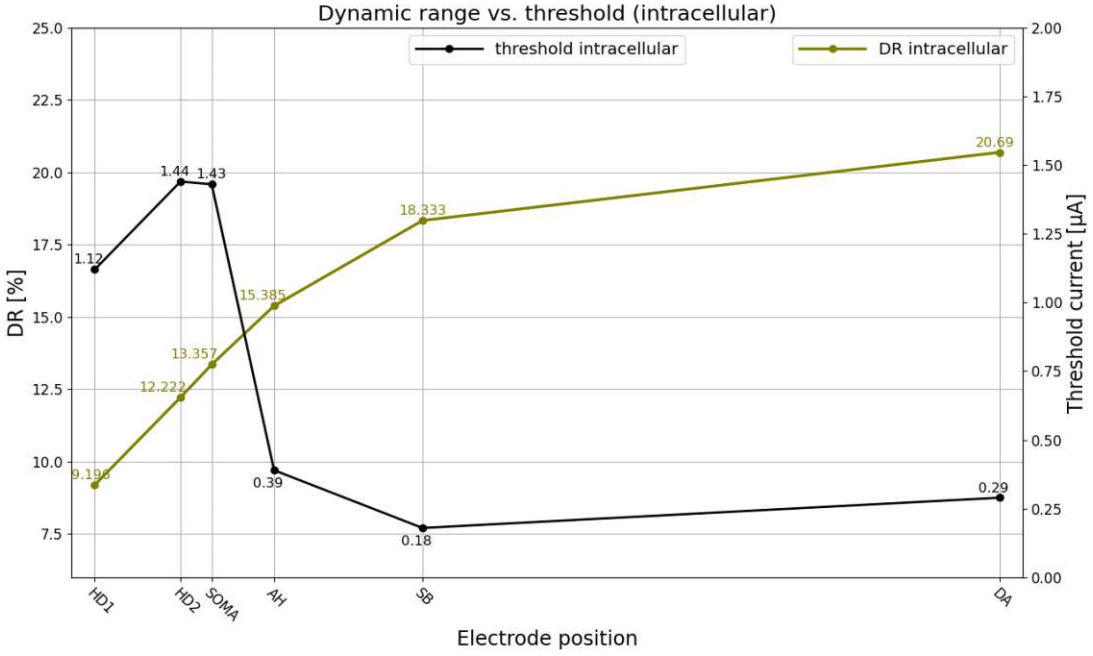

Figure 38: DR vs. electrode position (simulated section) obtained from intracellular monophasic anodic train of pulses. Threshold (black) and DR (olive) values are shown. For each electrode position, intracellular current stimulus was inserted into the central segment of the corresponding section with the exception of position HD2, where the stimulus was inserted into the first segment of the left horizontal dendrite.

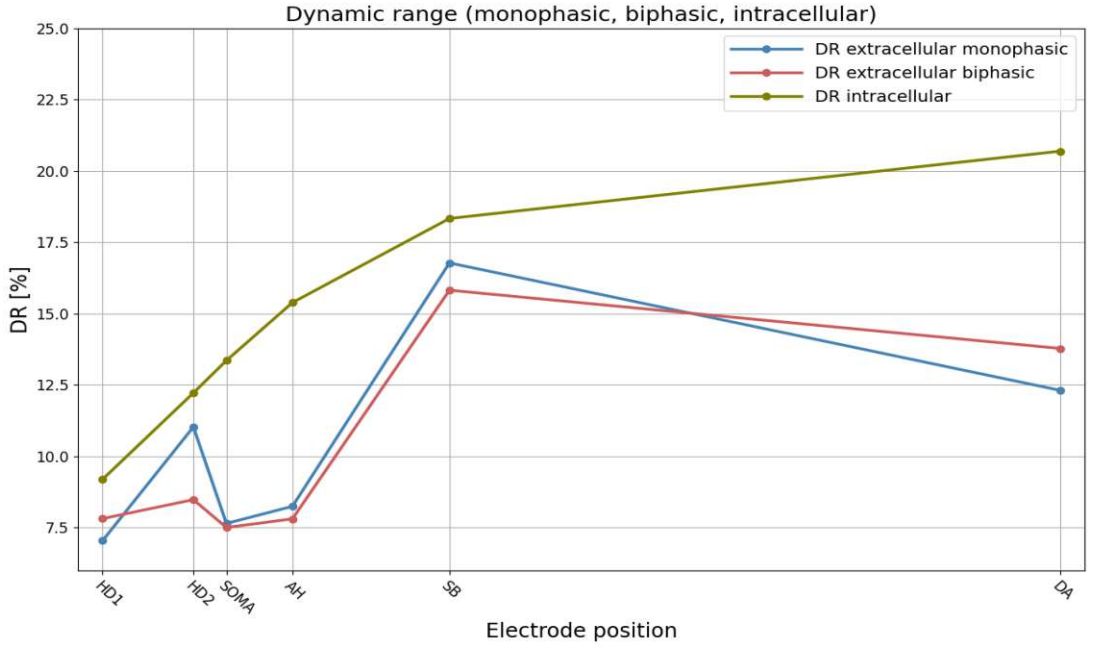

Figure 39: Compared estimated DR values for extracellular monophasic (blue), extracellular biphasic (red) and intracellular (olive) stimulation. Values presented for extracellular

stimulations are the one obtained for dist1. While no significant difference is observed between monophasic and biphasic stimulation, DR values estimated for intracellular stimulation show different behavior compared to them.

5.4.2 DR determination with increased channel noise at soma

In order to see how the DR changes if we assume that the channel noise generated in the soma is greater than the one in the other sections, noise standard deviation σ was increased from $\sigma = 1$ to $\sigma = 4$ at all soma segments. For all other sections, noise standard deviation remained unchanged. For extracellular stimulation, DR is again estimated for two defined distances: dist1 and dist2, while for intracellular stimulation as always only one set of simulations were performed. In the following figures, threshold values are not presented since they remained the same as for simulations with standard parameters.

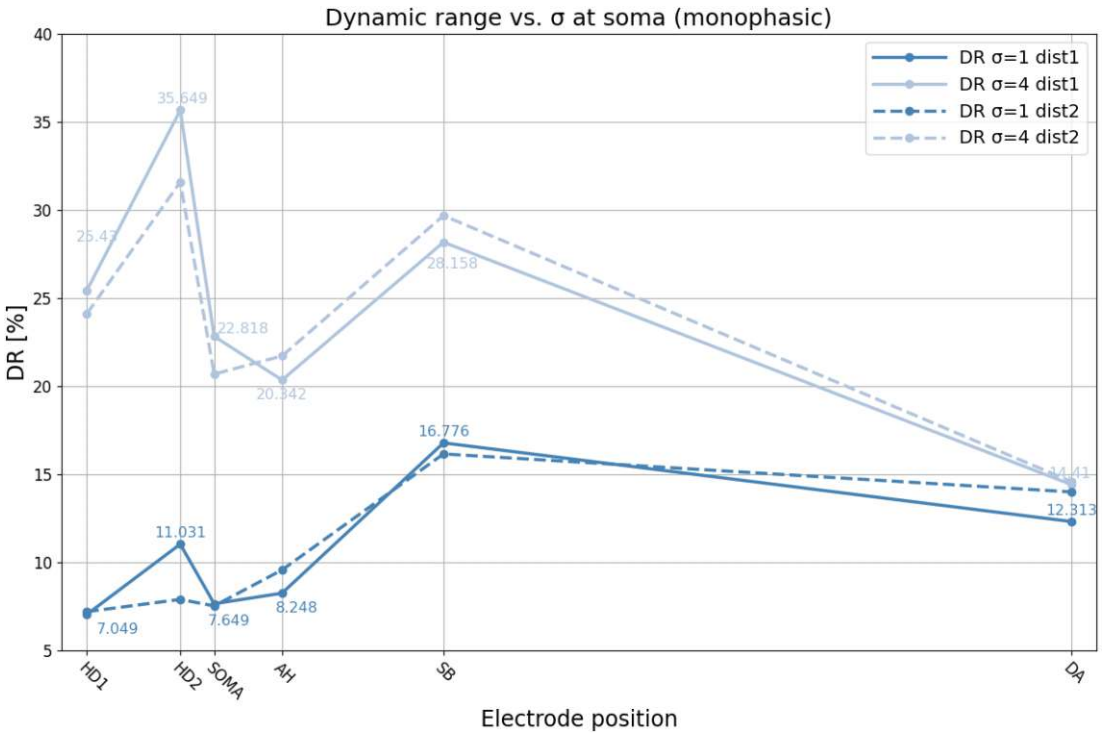

Figure 40: DR with 4x increased noise standard deviation $\sigma = 4$ at all soma segments in response to extracellular monophasic cathodic train of pulses. New DR values (light blue) were estimated for two distances: dist1 (solid line) and dist2 (dashed line) and compared to the previous results (blue), where noise standard deviation $\sigma = 1$ was the same for all segments.

Figure 40 shows results obtained from extracellular monophasic cathodic train of pulses. After inserting noise with four times greater σ at all soma segments, DR significantly increased for all electrode positions that are close enough to the soma.

Although the noise σ was increased only at soma, the highest increase is observed for electrode positions HD1 (260%) and HD2 (223%), followed with SOMA (198%), AH (147%), SB (68%) and DA (17%)[10]. Actually, DR increase decreases with each next electrode position and thus is the largest for electrode position HD1 and the lowest for electrode position DA. These increases resulted in the change of electrode positions with the highest and lowest estimated DR values. Now, highest DR is estimated for electrode position HD2 and lowest for electrode position DA (it is enough away from soma and change of noise standard deviation at soma has by far the least impact on this electrode position).

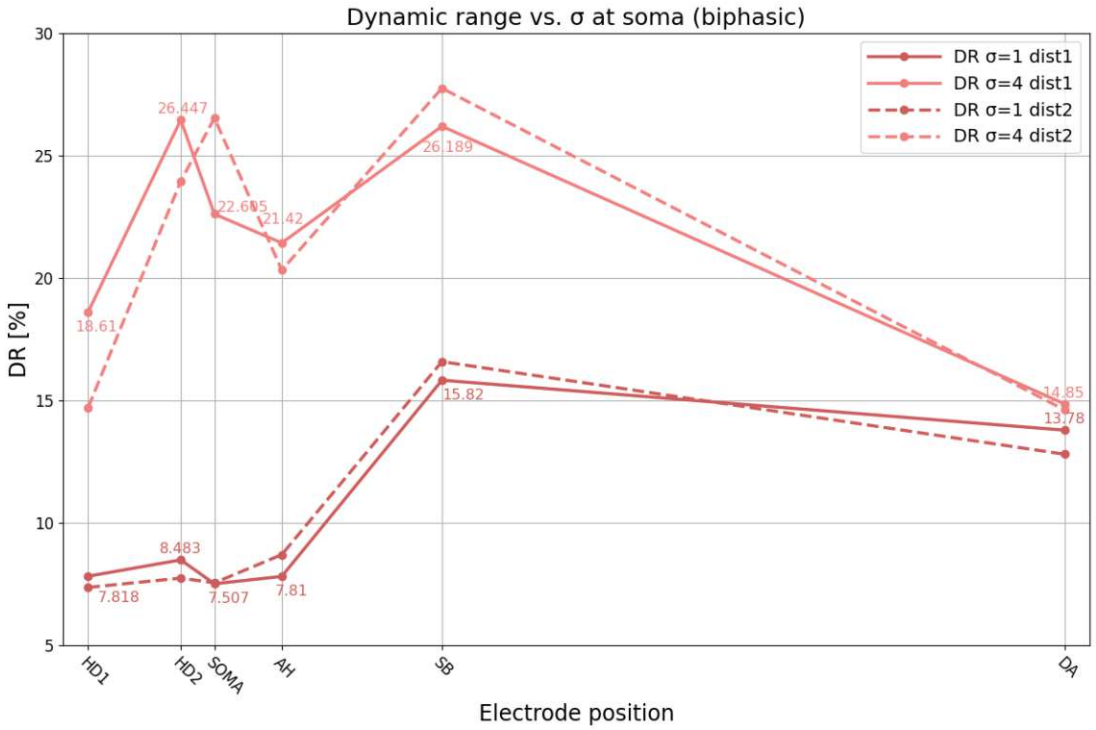

Figure 41: DR with 4x increased noise standard deviation $\sigma = 4$ at all soma segments in response to extracellular biphasic anodic-cathodic train of pulses. Same layout as in Figure 40.

The results obtained from extracellular biphasic anodic-cathodic train of pulses are presented in Figure 41. The highest DR increase is now observed for electrode positions HD2 (211%) and SOMA (202%), followed by AH (174%), HD1 (138%), SB (65%) and DA (7%)[10]. Compared to the results obtained from extracellular monophasic stimulus, percentages of DR increase here tend to be a bit lower, but the course remains similar (apart from DR increase at electrode position HD1, which is

[10] DR increase given as a percentage for each section is calculated using DR values estimated for dist1.

significantly lower than the one observed by monophasic stimulus). The highest DR values were estimated for positions HD2 and SB, while the lowest one was estimated for electrode position DA.

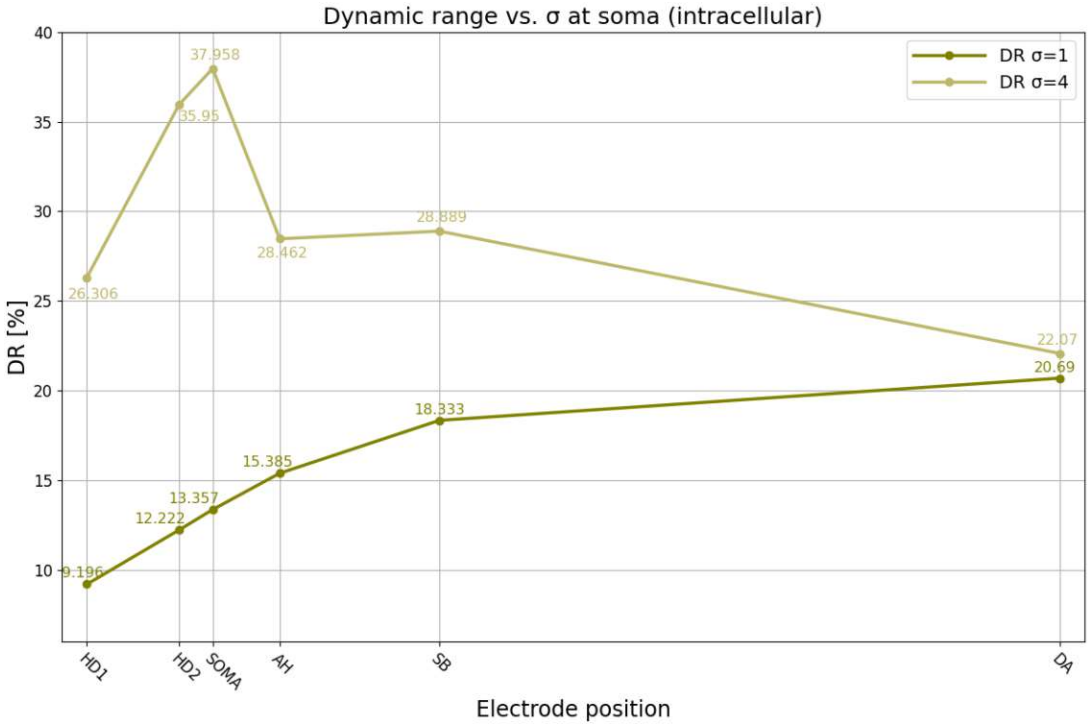

Figure 42: DR with 4x increased noise standard deviation σ = 4 at all soma segments in response to the intracellular anodic train of pulses. The results obtained with increased noise standard deviation at soma (light olive) are compared to the one with standard parameters (olive), where noise standard deviation σ = 1 was identical for all sections.

Figure 42 shows results obtained from an intracellular anodic train of pulses. Contrary to the extracellular stimulations, the course of the DR values has here significantly changed when compared to the results with standard parameters, where channel noise was identical for all sections. By far the largest DR increase was observed at position SOMA (284%) and from that position decreases in both directions with following percentages: HD2 (194%) and HD1 (186%) in one direction and SB (84%), AH (58%) and DA (7%) in other direction. Thus, the highest DR value was observed at position SOMA and as we move away from the soma DR values decrease. The lowest DR value is again observed for electrode position DA.

In order to better visualize how slope steepness of spiking probability as function of stimulus intensity change with electrode positions, DR values given in μA (not normalized to threshold) are presented for dist1 for all three types of stimulation in

Figure 43. The lower DR value in μA, the steeper spiking probability function observed.

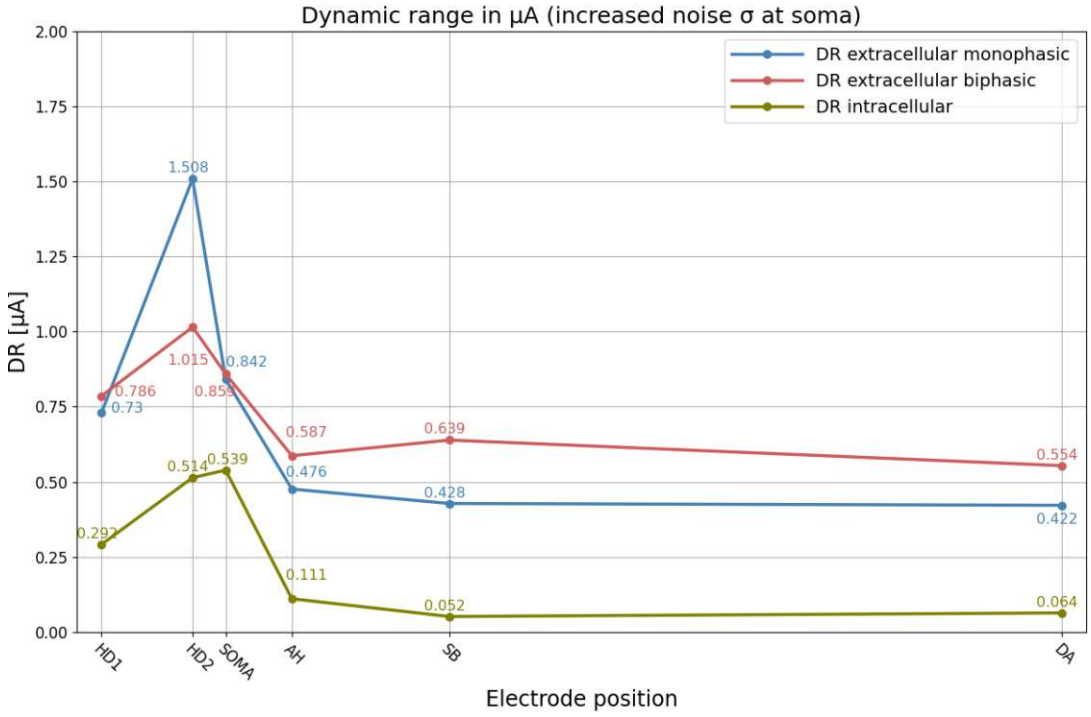

Figure 43: Compared estimated DR values with 4x increased noise standard deviation σ = 4 at all soma segments for extracellular monophasic (blue), extracellular biphasic (red) and intracellular (olive) stimulation. Values presented for extracellular stimulations are the one obtained for dist1. Note that presented DR values are given in μA (not normalized to threshold).

To sum it up, for extracellular stimulations, increase of noise standard deviation at soma, resulted in significantly increased DR values above all in soma and dendrite sections. Noticeable increase in DR values was also observed for electrode positioned above axon hillock and sodium band, while for electrode positioned above distal axon (far away from soma) almost no changes appear compared to other electrode positions. Contrary to that, for intracellular stimulation by far the largest increase in DR values was observed at soma and from there decreases in both directions, again with almost no influence on electrode positioned above distal axon. If we observe DR values given in μA, steeper spiking probability slopes are observed at axonal than at somatic parts of the cell for all three types of stimulation.

5.4.3 DR determination with an upper threshold

In previous sections, all DR values were estimated with a lower threshold, since it was the main aim of this thesis. At the end, we decided to concentrate a bit on determining DR values with an upper threshold. For that purpose, extracellular monophasic cathodic stimulus was chosen, while electrode positions correspond to dist1.

When estimating the upper threshold, different thresholds could be observed in dependency of the AP measurement site. In our case, as for all other simulations, APs were measured at soma. Thereby, for most electrode positions (HD1, HD2, SOMA, DA) with upper threshold estimated at soma, no AP was observed in any other cell section, while for electrode positions AH and SB upper threshold at soma did not prevent AP conductance in the axon.

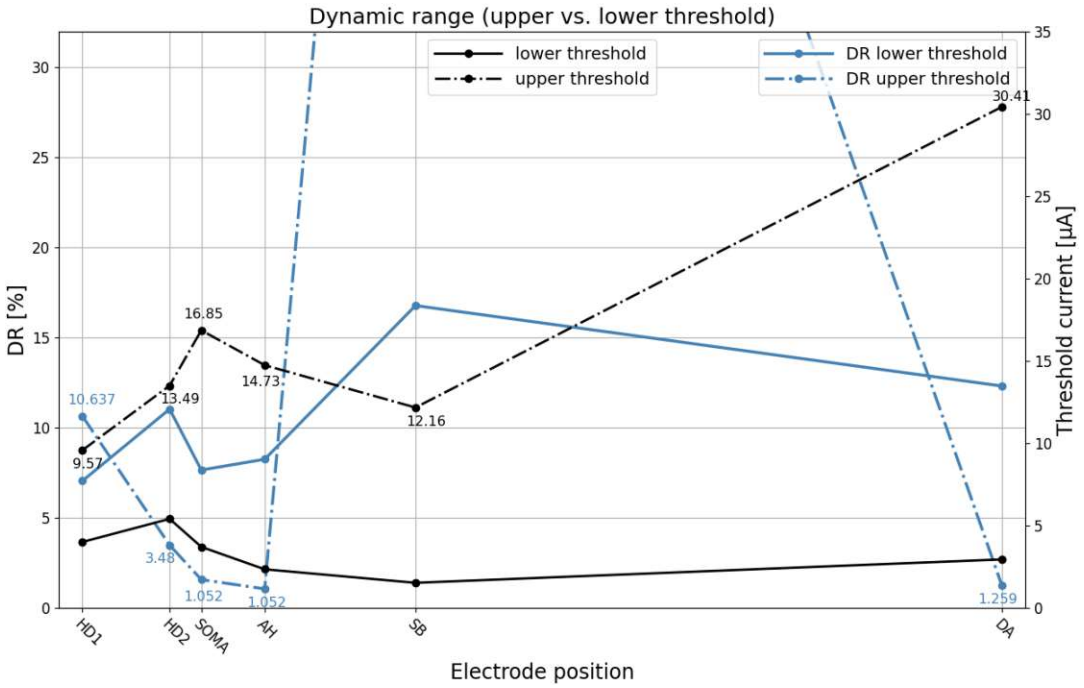

Figure 44: DR estimated with upper and lower threshold obtained from extracellular monophasic cathodic train of pulses for dist1. Threshold and DR values referring to the upper threshold are plotted with dash-dotted lines and compared with lower threshold results (solid lines).

Figure 44 shows results obtained from extracellular monophasic cathodic train of pulses for both lower and upper threshold. If we exclude electrode positions HD1 and SB, we recognize that for upper threshold, DR values for each electrode position are significantly lower than DR values observed for lower threshold. The reason for that probably lies in the fact that DR values are presented as normalized to threshold. Since

upper threshold values are notably higher, we expect smaller DR values given as percentage for same DR values given in μA.

In order to get better insight into all this, DR values given in μA (not normalized to threshold) are presented for both lower and upper thresholds in Figure 45. Thereby, electrode position SB was excluded since no explanation could be found for such high DR value. Now, apart from electrode position HD1, DR values not normalized to threshold for all other electrode positions show high degree of similarity.

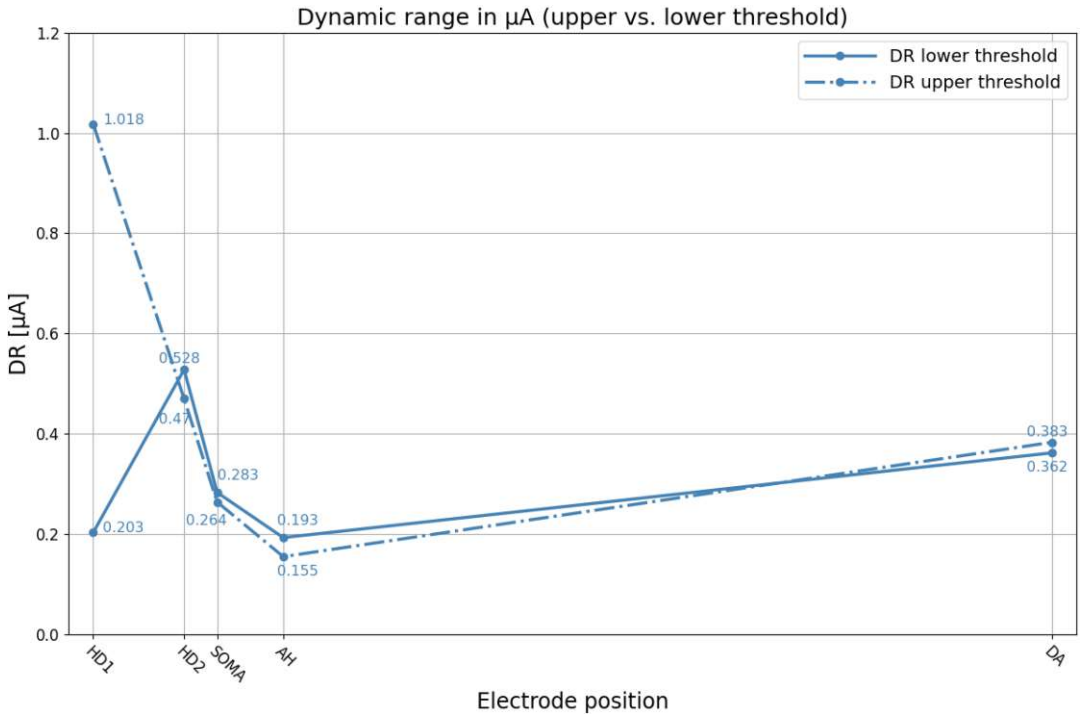

Figure 45: DR estimated with upper and lower threshold obtained from extracellular monophasic cathodic train of pulses for dist1. Note that presented DR values are given in μA (not normalized to threshold). DR values referring to upper threshold are plotted with dash-dotted lines and compared with lower threshold results (solid lines).

.

6 Discussion

In this section we tried to sum up and analyze presented results and if possible to compare them with already existing research. Additionally, limitations of the used modeling methods as well as suggestions for further work are discussed. Note that unless otherwise stated, DR values are discussed as a percentage (normalized to threshold).

6.1 Discussion of presented results

Our model follows a negative linear relationship between $\log RS$ and $\log diameter$ (Figure 29) reported by experimental studies (Verveen, 1962), but contrary to the recent modeling studies (Rattay & Tanzer, 2022b) does not actually follow Verveen´s equation $\log(RS) = -1.5 - 0.8\log(d)$. Several factors could explain such behavior. Firstly, in mentioned studies from Rattay and Tanzer, a common factor k_{noise} was actually adapted for different axon models in order to approximate Verveen´ s equation. Secondly, if we implement a more complex model, the strength of the linearity depends also on electrode position or pulse polarity which could lead to deviations from the given equation, as reported by Tanzer (2021).

Speaking about threshold values, regardless of used stimulus type, the lowest threshold was always observed at sodium band, which is consistent with the previous studies (Fried, et al., 2009; Jeng, et al., 2011; Werginz, et al., 2014; Werginz, et al., 2020), while thresholds for other sections increased with distance from sodium band as reported by Madugula, et al. (2022). Since the sodium band is the section most responsive to electrical stimulation, we could expect rather lower DR values for electrode positioned above the sodium band. However, for both monophasic and biphasic extracellular stimulations the sodium band was the section with the highest observed DR values. Since sodium band has by far the highest maximal sodium conductance $\bar{g}_{Na}$, these results could be related to the fact that inserted noise current is proportional to the square root of the $\bar{g}_{Na}$ within a section and thus as shown in

Figure 30, with increased $\bar{g}_{Na}$ DR values also increase. Lowest DR values were observed at electrode positions near the soma and dendrites. A possible explanation for this might lie in their geometry and relatively low $\bar{g}_{Na}$ defined for dendrites. The notable difference between DR values for electrode positioned above axon hillock and distal axon, despite their same diameter and biophysical properties, could be explained with their different positions in the cell (distal axon, as the name suggest, is placed relatively far away from other sections which decreases their influence on it) and the fact that for axon hillock APs are initiated at sodium band, while for distal axon site of excitation and AP initiation remains same. It can be therefore assumed that besides maximal sodium conductance $\bar{g}_{Na}$ and diameter, DR value of a certain section may be influenced by the section length, surrounding sections or place of AP initiation.

Additionally, we need to keep in mind that those DR values are the one normalized to threshold and thus corresponding threshold values also influence presented DR values. It is one more reason why the highest DR value for extracellular stimulation is observed for electrode positioned above the sodium band. It can thus be suggested that DR values show a somewhat inverse relationship to threshold (Figures 36-37). This provides some explanation as to why DR values determined for intracellular stimulation differ from the one determined for extracellular stimulations, especially for electrode positioned above distal axon (Figure 38). While both threshold and DR curves for monophasic and biphasic extracellular stimulation show very similar tendencies, threshold and thus DR values for intracellular stimulation differ notably. Similar degree of inverse relationship between DR values given as percentage and thresholds is observed in modeling study for pyramidal cell (Cvetkovic, 2022).

With increased noise standard deviation in all soma segments, similar results are observed as the one from experiments reported by Madugula, et al. (2022). Spiking probability functions as a function of stimulus intensity for axonal sections are steeper than the one observed for somatic and dendrite sections (Figure 43), regardless of the type of stimulus. Effects of the additionally inserted noise are noticeable in all sections, with being the lowest at the distal axon (Figures 40-41). It is important to note that before increasing a noise standard deviation in all soma segments, steeper spiking probability functions for axonal than for somatic and dendrite sections were observed

only for intracellular stimulation, while for extracellular stimulations (both monophasic and biphasic) steeper spiking probability functions were often observed for electrode positioned near the soma than electrode positioned above distal axon.

In contrast to earlier findings from Rattay & Tanzer (2022b), where the increase of RS with increased electrode-axon distance was reported, we have been unable to demonstrate that behavior in this thesis. Although we could expect an increase in RS and thus in DR with increased electrode-cell distance (the further the electrode is, the larger the surface is stimulated and thus more ion channels are involved in the AP generation), results presented here show no consistent dependency on the electrode-cell distance. Furthermore, those differences mostly appear to be rather small or for some cases even totally negligible (e.g. electrode positions HD1 and SOMA in Figure 37).

The ratios of estimated upper and lower threshold values for extracellular monophasic stimulus are in accordance with the one reported by previous studies (Boinagrov, et al., 2012; Meng, et al., 2018; Sajedi, et al., 2021) with an average of 5.68. The phenomenon where upper threshold in soma does not prevent AP conductance in axon discussed in recent studies (Meng, et al., 2018; Fellner, et al., 2019) was observed when stimulating axon hillock and sodium band, while for all other stimulated sections with upper threshold in soma no AP was observed in any other section. Speaking about estimated DR values with an upper threshold, if we exclude electrode positions above left horizontal dendrite (HD1) and sodium band (SB), DR values in μA (not normalized to threshold) are similar to estimated DR values in μA with a lower threshold (Figure 45). Similar DR values in μA with an upper and lower threshold could indicate the existence of a characteristic U-shape of spiking probability as a function of stimulus intensity as reported in experimental and modeling studies (Boinagrov, et al., 2012; Meng, et al., 2018). Although DR values in μA are similar with both lower and upper thresholds, DR values normalized to threshold are as expected significantly lower with an upper threshold.

6.2 Limitations of the model and further work

The major limitation of this study is related to the implemented RGC model. The cell geometry was simplified to a 2D model and biophysical properties and dynamics were based on Fohlmeister and Miller model from 1997 and thus all simulations needed to be performed at the temperature of 22℃, which is not applicable for humans. In order to get better insight and more accurate results, for further work from the modeling side we suggest implementation of a real 3D model based on a newer RGC model derived from experimental measurements on rats and cats (Fohlmeister, et al., 2010) that also includes temperature as a variable. Thereby, more time needs to be invested into mechanisms that work against spontaneous firing of the RGC, since the newer model is more prone to it.

Since it seems that there is a lack of both experimental and modeling studies related to DR in general, but especially related to its dependency on stimulated cell section, results of this thesis only provide first insights into the DR behavior and thus leave a lot of room for improvement and further work. Therefore, presented results need to be interpreted cautiously and every aspect should be further investigated. Since experimental results reported by Madugula, et al. (2022) suggest that sigmoidal curve of spiking probability as a function of stimulus intensity is steeper for axonal than for soma compartments, which is not observed with our model when using extracellular stimulations (monophasic or biphasic) unless more noise is injected into soma segments, special attention should be paid on it. Thereby, factors that affect spiking probability and thus DR should be thoroughly investigated (especially at soma region) and according to that, modifications of noise modeling approach should be discussed, so that it can reliably imitate experimental results. Another interesting point for further work could be determination of DR with an upper threshold, which was only slightly examined in this thesis.

Appendix Parameters and Equations

Geometry	SOMA	AH	SB	TS	DA	VD	HDL	HDR
Diameter d $[\mu m]$	20	1	1-0.6	0.6-1	1	4	2	2
Length l $[\mu m]$		40	40	90	150	10	75	75
Inclination angle [°C]		20						
Number of segments	21	41	41	21	51	5	21	21
Biophysics	**SOMA**	**AH**	**SB**	**TS**	**DA**	**VD**	**HDL**	**HDR**
$\bar{g}_{Na}$ $[mS/cm^2]$	80	70	400	100	70	25	25	25
$\bar{g}_{K}$ $[mS/cm^2]$	19.2	16.8	96	24	16.8	6	6	6
$\bar{g}_{L}$ $[mS/cm^2]$	0.08	0.07	0.4	0.1	0.07	0.025	0.025	0.025
$\bar{g}_{K,A}$ $[mS/cm^2]$	57.6	50.4	288	72	50.4	18	18	18
$\bar{g}_{Ca}$ $[mS/cm^2]$	3.52	3.08	17.6	4.4	3.08	1.1	1.1	1.1
$\bar{g}_{K,Ca}$ $[mS/cm^2]$	0.08	0.07	0.4	0.1	0.07	0.025	0.025	0.025

Parameters independent of section

Nernst potential	
E_{Na} $[mV]$	35
E_{K} $[mV]$	-75
E_{L} $[mV]$	-62.5
E_{Ca} $[mV]$	132.46

Simulation parameters	
$dur_{init\ phase}$ $[ms]$	500
$dt_{init\ phase}$ $[ms]$	10
$dur_{fine\ phase}$ $[ms]$	10
$dt_{fine\ phase}$ $[ms]$	0.0025
$dur_{wait\ phase}$ $[ms]$	150
$dt_{wait\ phase}$ $[ms]$	1
dur_{pulse} $[ms]$	0.2
$dur_{pulse,biphasic}$ $[ms]$	0.4
pulses pro simulation	10 000

General cell parameters	
C_m $[\mu F]$	1
ρ_i $[\Omega cm]$	300
ρ_e $[\Omega cm]$	1000
T [°C]	22

Noise parameters	
μ	0
σ	1
dt_{noise} $[ms]$	0.0025
k_{noise} $[\mu A/\sqrt{mS}]$	0.0038

Electrode-cell distance	
dist1 $[\mu m]$	26
dist2 $[\mu m]$	36

Table 7: Standard parameters defined for simulations in this thesis.

Equation used for calculating membrane voltage:

$$\dot{V} = \left[-\bar{g}_{Na} m^3 h (V - E_{Na}) - \bar{g}_{Ca} c^3 (V - E_{Ca}) - (\bar{g}_K n^4 + \bar{g}_A a^3 h_A + \bar{g}_{K,Ca})(V - E_K) - \bar{g}_L (V - E_L) + i_{st}\right]/c$$

Equation used for calculating gating variables of voltage-gated ion channels (m, h, c, n, a, h_A):

$$\dot{x} = -(\alpha_x + \beta_x)x + \alpha_x$$

with following equations for opening α_x and closing rates β_x:

$$\alpha_m = \frac{-0.6(V+30)}{e^{-0.1(V+30)} - 1}; \qquad \beta_m = 20e^{-(V+55)/18}$$

$$\alpha_h = 0.4e^{-(V+50)/20}; \qquad \beta_h = \frac{6}{e^{-0.1(V+20)} + 1}$$

$$\alpha_c = \frac{-0.3(V+13)}{e^{-0.1(V+13)} - 1}; \qquad \beta_c = 10e^{-(V+38)/18}$$

$$\alpha_n = \frac{-0.02(V+40)}{e^{-0.1(V+40)} - 1}; \qquad \beta_n = 0.4e^{-(V+50)/80}$$

$$\alpha_a = \frac{-0.06(V+90)}{e^{-0.1(V+90)} - 1}; \qquad \beta_a = 0.1e^{-(V+30)/10}$$

$$\alpha_{h,A} = 0.04e^{-(V+70)/20}; \qquad \beta_{h,A} = \frac{0.6}{e^{-0.1(V+40)} + 1}$$

Equation used for calculating ligand-gated ion channel:

$$g_{K,Ca} = \bar{g}_{K,Ca} \frac{([Ca^{2+}]_i/(Ca^{2+})_{diss})^2}{1 + ([Ca^{2+}]_i/(Ca^{2+})_{diss})^2}$$

Sources of equations: (Fohlmeister, et al., 1990; Fohlmeister & Miller, 1997a).

Abbreviations

AH	axon hillock
AMD	age-related macular degeneration
AP	action potential
DA	distal axon
DR	dynamic range
FCM	Fohlmeister-Coleman-Miller
HDL	horizontal dendrite left
HDR	horizontal dendrite right
RGC	retinal ganglion cell
RS	relative spread
SB	sodium band
TS	thin segment
VD	vertical dendrite

References

Abramian, M. et al., 2014. Quasi-monopolar electrical stimulation of the retina: a computational modelling study. *Journal of Neural Engineering*, 11(2), p. 025002.

Abramian, M. et al., 2011. Activation of retinal ganglion cells following epiretinal electrical stimulation with hexagonally arranged bipolar electrodes. *Journal of Neural Engineering*, 8(3), p. 035004.

Al Abed, A. et al., 2012. Convolution based method for calculating inputs from dendritic fields in a continuum model of the retina. *Annual International Conference of the IEEE Engineering in Medicine and Biology Society. IEEE Engineering in Medicine and Biology Society. Annual International Conference*, p. 215–218.

Alberts, B. et al., 2002. Ion channels and the electrical properties of membranes. In: *Molecular biology of the cell.* 4. ed. New York: Garland Science.

Boinagrov, D., Loudin, J. & Palanker, D., 2010. Strength-duration relationship for extracellular neural stimulation: numerical and analytical models. *Journal of Neurophysiology*, 104(4), pp. 2236-2248.

Boinagrov, D. et al., 2012. Upper threshold of extracellular neural stimulation. *Journal of Neurophysiology*, 108(12), pp. 3233-3238.

Byrne, J. H. & Dafny, N. eds., n.d. *Neuroscience online: an electronic textbook for the neuroscience.* [Online] Available at: http://nba.uth.tmc.edu/neuroscience/ [Accessed 13 11 2022].

Cleveland Clinic, n.d. *Cleveland Clinic.* [Online] Available at: https://my.clevelandclinic.org/health/body/22694-retina-eye [Accessed 1 11 2022].

Cohen, E. D., 2018. Retinal Prostheses. In: H. Kolb, E. Fernandez & R. Nelson, eds. *Webvision: The organization of the retina and visual system [Internet].* Salt Lake City (UT): University of Utah Health Sciences Center.

Cooper, G., 2000. Cell membranes. In: *The cell: a molecular approach.* 2. ed. Sunderland (MA): Sinauer Associates.

Cvetkovic, D., 2022. *Spiking efficiency of electrically stimulated pyramidal cells: a modeling study.* Unpublished master´s thesis. Vienna University of Technology.

Dayan, P. & Abbott, L. F., 2005. Model neurons II: conductances and morphology. In: *Theoretical neuroscience: computational and mathematical modeling of neural systems.* s.l.:The MIT Press, pp. 195-228.

Dokos, S., Suaning, G. J. & Lovell, N. H., 2005. A bidomain model of epiretinal stimulation. *IEEE Transactions on Neural Systems and Rehabilitation Engineering : A Publication of the IEEE Engineering in Medicine and Biology Society*, 13(2), pp. 137-146.

Ezeokafor, I., Upadhya, A. & Shetty, S., 2021. Neurosensory prosthetics: an integral neuromodulation part of bioelectronic device. *Frontiers in Neuroscience,* Volume 15, p. 671767.

Fellner, A., 2017. *Modeling block of excitation of retinal ganglion cell stimulated with microelectrodes using python and neuron.* Master´s thesis. Vienna University of Technology.

Fellner, A., Stiennon, I. & Rattay, F., 2019. Analysis of upper threshold mechanisms of spherical neurons during extracellular stimulation. *Journal of Neurophysiology*, 121(4), pp. 1315-1328.

Fitzpatrick, D., 2015. Chapter 1 - Retinal implants. In: *Implantable electronic medical devices.* s.l.:Academic Press, pp. 1-18.

Fohlmeister, J. F., Cohen, E. D. & Newman, E. A., 2010. Mechanisms and distribution of ion channels in retinal ganglion cells: using temperature as an independent variable. *Journal of Neurophysiology*, 103(3), pp. 1357-1374.

Fohlmeister, J. F., Coleman, P. A. & Miller, R. F., 1990. Modeling the repetitive firing of retinal ganglion cells. *Brain Research*, 510(2), pp. 343-345.

Fohlmeister, J. F. & Miller, R. F., 1997a. Impulse encoding mechanisms of ganglion cells in the tiger salamander retina. *Journal of Neurophysiology*, 78(4), pp. 1935-1947.

Fohlmeister, J. F. & Miller, R. F., 1997b. Mechanisms by which cell geometry controls repetitive impulse firing in retinal ganglion cells. *Journal of Neurophysiology*, 78(4), pp. 1948-1964.

Fried, S. I. et al., 2009. Axonal sodium-channel bands shape the response to electric stimulation in retinal ganglion cells. *Journal of Neurophysiology*, 101(4), pp. 1972-1987.

Gerstner, W., Kistler, W. M., Richard, N. & Paninski, L., 2014. *Neuronal dynamics: from single neurons to networks and models of cognition.* Cambridge: Cambridge University Press.

Goldwyn, J. H., Imennov, N. S., Famulare, M. & Shea-Brown, E., 2011. Stochastic differential equation models for ion channel noise in Hodgkin-Huxley neurons. *Physical review. E, Statistical, Nonlinear, and Soft Matter Physics*, 83(4).

Goldwyn, J. H. & Shea-Brown, E., 2011. The what and where of adding channel noise to the Hodgkin-Huxley equations. *PLoS Computational Biology*, 7(11), p. e1002247.

Greenberg, R. J. et al., 1999. A computational model of electrical stimulation of the retinal ganglion cell. *IEEE Transactions on Bio-medical Engineering*, 46(5), pp. 505-514.

Grosberg, L. E. et al., 2017. Activation of ganglion cells and axon bundles using epiretinal electrical stimulation. *Journal of Neurophysiology*, 118(3), pp. 1457-1471.

Guo, T. et al., 2014. Understanding the retina: a review of computational models of the retina from the single cell to the network level. *Critical Reviews in Biomedical Engineering*, 42(5), pp. 419-436.

Guo, T. et al., 2013. Cell-specific modeling of retinal ganglion cell electrical activity. *35th Annual International Conference of the IEEE Engineering in Medicine and Biology Society (EMBC)*, pp. 6539-6542.

Hines, M., 1993. NEURON — a program for simulation of nerve equations. In: F. H. Eeckman, ed. *Neural systems: analysis and modeling.* Boston, MA: Springer, pp. 127-136.

Hines, M. L. & Carnevale, N. T., 1997. The NEURON simulation environment. *Neural Computation*, 9(6), pp. 1179-1209.

Hodgkin, A. L. & Huxley, A. F., 1952. A quantitative description of membrane current and its application to conduction and excitation in nerve. *The Journal of Physiology,* 117(4), pp. 500-544.

Jeng, J. et al., 2011. The sodium channel band shapes the response to electric stimulation in retinal ganglion cells. *Journal of Neural Engineering*, 8(3), p. 036022.

Joarder, S. A. et al., 2011. A continuum model of retinal electrical stimulation. *Journal of Neural Engineering*, 8(6), p. 066006.

Kameneva, T., Meffin, H. & Burkitt, A. N., 2011. Modelling intrinsic electrophysiological properties of ON and OFF retinal ganglion cells. *Journal of Computational Neuroscience*, 31(3), pp. 547-561.

Lamb, T. D., 2016. Why rods and cones?. *Eye (London, England)*, 30(2), pp. 179-185.

Madugula, S. S. et al., 2022. Inference of electrical stimulation sensitivity from recorded activity of primate retinal ganglion cells. *BioRxiv*.

Mahabadi, N. & Al Khalili, Y., 2022. Neuroanatomy, retina. In: *StatPearls [Internet]*. Treasure Island (FL): StatPearls Publishing.

Maturana, M. I. et al., 2014. The effect of morphology upon electrophysiological responses of retinal ganglion cells: simulation results. *Journal of Computational Neuroscience*, 36(2), pp. 157-175.

Meng, K. et al., 2018. Upper stimulation threshold for retinal ganglion cell activation. *Journal of Neural Engineering*, 15(4), p. 046012.

Miller, R. F., Staff, N. P. & Velte, T. J., 2006. Form and function of ON-OFF amacrine cells in the amphibian retina. *Journal of Neurophysiology*, 95(5), pp. 3171-3190.

Mino, H., Rubinstein, J. T. & White, J. A., 2002. Comparison of algorithms for the simulation of action potentials with stochastic sodium channels. *Annals of Biomedical Engineering*, 30(4), pp. 578-587.

Pfützner, H., 2012. *Angewandte Biophysik.* 2. ed. s.l.:Springer Vienna.

Publio, R., Ceballos, C. C. & Roque, A. C., 2012. Dynamic range of vertebrate retina ganglion cells: importance of active dendrites and coupling by electrical synapses. *PLoS ONE*, 7(10), p. e48517.

Publio, R., Oliveira, R. F. & Roque, A. C., 2009. A computational study on the role of gap junctions and rod Ih conductance in the enhancement of the dynamic range of the retina. *PLoS ONE*, 4(9), p. e6970.

Purves, D. et al. eds., 2004. *Neuroscience.* 3. ed. Sunderland (MA): Sinauer Associates.

Rattay, F., 1990. *Electrical nerve stimulation: theory, experiments, and applications.* s.l.:Springer Vienna.

Rattay, F., 1999. The basic mechanism for the electrical stimulation of the nervous system. *Neuroscience*, 89(2), pp. 335-346.

Rattay, F., 2000. Basics of hearing theory and noise in cochlear implants. *Chaos, Solitons & Fractals*, 11(12), pp. 1875-1884.

Rattay, F., 2014. On the upper threshold phenomenon of extracellular neural stimulation. *Journal of Neurophysiology*, 112(10), pp. 2664-2665.

Rattay, F. & Aberham, M., 1993. Modeling axon membranes for functional electrical stimulation. *IEEE Transactions on Bio-medical Engineering*, 40(12), pp. 1201-1209.

Rattay, F., Lutter, P. & Felix, H., 2001. A model of the electrically excited human cochlear neuron. I. Contribution of neural substructures to the generation and propagation of spikes. *Hearing Research*, 153(1-2), pp. 43-63.

Rattay, F. & Resatz, S., 2004. Effective electrode configuration for selective stimulation with inner eye prostheses. *IEEE Transactions on Bio-medical Engineering*, 51(9), pp. 1659-1664.

Rattay, F. et al., 2003. Mechanisms of electrical stimulation with neural prostheses. *Neuromodulation*, 6(1), pp. 42-56.

Rattay, F. & Tanzer, T., 2022a. Impact of electrode position on the dynamic range of a human auditory nerve fiber. *Journal of Neural Enginneering*, Volume 19, p. 016025.

Rattay, F. & Tanzer, T., 2022b. A simple model considering spiking probability during extracellular axon stimulation. *PLoS ONE*, 17(4), p. e0264735.

Resatz, S. & Rattay, F., 2004. A model for the electrically stimulated retina. *Mathematical and Computer Modelling of Dynamical Systems - MATH COMPUT MODEL DYNAM SYST*, 10(2), pp. 93-106.

Rubinstein, J. T., 1995. Threshold fluctuations in an N sodium channel model of the node of Ranvier. *Biophysical Journal*, 68(3), pp. 779-785.

Sajedi, S., Fellner, A., Werginz, P. & Rattay, F., 2021. Block phenomena during electric micro-stimulation of pyramidal cells and retinal ganglion cells. *Frontiers in Cellular Neuroscience*, Volume 15, p. 771600.

Schachter, M. J., Oesch, N., Smith, R. G. & Taylor, W. R., 2010. Dendritic spikes amplify the synaptic signal to enhance detection of motion in a simulation of the direction-selective ganglion cell. *PLoS Computational Biology*, 6(8), p. e1000899.

Schiefer, M. A. & Grill, W. M., 2006. Sites of neuronal excitation by epiretinal electrical stimulation. *IEEE Transactions on Neural Systems and Rehabilitation Engineering : A Publication of the IEEE Engineering in Medicine and Biology Society*, 14(1), pp. 5-13.

Sheasby, B. W. & Fohlmeister, J. F., 1999. Impulse encoding across the dendritic morphologies of retinal ganglion cells. *Journal of Neurophysiology*, 81(4), pp. 1685-1698.

Shepherd, R. K. & Javel, E., 1997. Electrical stimulation of the auditory nerve. I. Correlation of physiological responses with cochlear status. *Hearing Research*, 108(1-2), pp. 112-144.

Tandon, P. et al., 2021. Automatic identification of axon bundle activation for epiretinal prosthesis. *IEEE Transactions on Neural Systems and Rehabilitation Engineering : A Publication of the IEEE Engineering in Medicine and Biology Society, 29*, pp. 2496-2502.

Tanzer, T., 2021. *Analysis of ion current fluctuations in multi-compartment models of electrically stimulated neurons.* PhD thesis. Vienna University of Technology.

Tong, W. et al., 2020. Minimizing axon bundle activation of retinal ganglion cells with oriented rectangular electrodes. *Journal of Neural Engineering*, 17(3), p. 036016.

Tsai, D. et al., 2012. Responses of retinal ganglion cells to extracellular electrical stimulation, from single cell to population: model-based analysis. *PLoS ONE*, 7(12), p. e53357.

Velte, T. J. & Miller, R. F., 1995. Dendritic integration in ganglion cells of the mudpuppy retina. *Visual Neuroscience*, 12(1), pp. 165-175.

Velte, T. J. & Miller, R. F., 1997. Spiking and nonspiking models of starburst amacrine cells in the rabbit retina. *Visual Neuroscience*, 14(6), pp. 1073-1088.

Verveen, A. A., 1960. On the fluctuation of threshold of the nerve fibre. *Structure and Function of the Cerebral Cortex*, pp. 282-288.

Verveen, A. A., 1962. Axon diameter and fluctuation in excitability. *Acta Morphologica Neerlando-Scandinavica*, pp. 79-85.

Vilkhu, R. S. et al., 2021. Spatially patterned bi-electrode epiretinal stimulation for axon avoidance at cellular resolution. *Journal of Neural Engineering*, 18(6).

Werginz, P., Fried, S. I. & Rattay, F., 2014. Influence of the sodium channel band on retinal ganglion cell excitation during electric stimulation--a modeling study. *Neuroscience*, Volume 266, pp. 162-177.

Werginz, P., Raghuram, V. & Fried, S. I., 2020. The relationship between morphological properties and thresholds to extracellular electric stimulation in α RGCs. *Journal of Neural Engineering*, Volume 17, p. 045015.

Werginz, P. & Rattay, F., 2014. Past, present, future: a review on visual prostheses. *Minerva Medica*, 106(1), pp. 65-77.

White, J. A., Rubinstein, J. T. & Kay, A. R., 2000. Channel noise in neurons. *Trends in Neurosciences*, 23(3), pp. 131-137.

Yin, S., Lovell, N. H., Suaning, G. J. & Dokos, S., 2010. A continuum model of the retinal network and its response to electrical stimulation. *Annual International Conference of the IEEE Engineering in Medicine and Biology Society. Annual International Conference*, pp. 2077-2080.

Yin, S., Lovell, N. H., Suaning, G. J. & Dokos, S., 2011. Continuum model of light response in the retina. *Annual International Conference of the IEEE Engineering in Medicine and Biology Society. IEEE Engineering in Medicine and Biology Society. Annual International Conference*, pp. 908-911.